Foot Impact and Dynamic Analyses of Piezoelectrically-Actuated Walking Micro-Robots

by

Jeong Hoon Ryou

A dissertation submitted in partial fulfillment
Of the requirements for the degree of
Doctor of Philosophy
(Mechanical Engineering)
in The University of Michigan
2013

Doctoral Committee:

Assistant Professor Kenn Richard Oldham, Chair
Professor Brent Gillespie
Professor Jessy W. Grizzle
Professor Karl Grosh

TABLE OF CONTENTS

LIST OF FIGURES

LIST OF TABLES

LIST OF APPENDICES

ABSTRACT

The objective of this dissertation is to establish a dynamic modeling procedure capturing both structural motions and contact/impact behavior including quantification of small-scale contact forces. It is difficult to model the dynamics of batch-fabricated walking micro-robots since foot-terrain contact interaction is very complicated due to continuous mechanical structure and comparably large influence of various small-scale contact forces. However, a dynamic model with a good level of accuracy is strongly desirable for design of control inputs and mechanical structures to increase energy efficiency and operation reliability; such robots have harsh limitations on power source capacity and electronic components due to their intended mobility and small structural dimensions. For a selection of piezoelectrically-operated walking micro-robots studied in this work, the foot contact/impact behavior is so complicated that no contact/impact models previously introduced in various fields of study provide adequate estimation in time/frequency-domain responses. Thus, this work proposes a dynamic modeling procedure for such walking micro-robotic systems under repetitive single foot-terrain interaction and, three individual tasks were conducted to accomplish this objective.

The first task is to analyze a simple micro-cantilever test structure that mimics the foot-terrain interaction of the walking micro-robots. This task proposes a modeling and identification procedure for contact dynamics without knowledge of geometric profile or material of the ground surface. Since this modeling method does not assume to know the contact surface geometries, it can be applied to dynamic modeling of the mobile walking robots for which ground condition can be changeable and unknown. Experimental comparison with various test cases validated the proposed dynamic model showing a fairly accurate estimation in time-domain responses.

The second task is to characterize impact behavior with two robotic structures operated by “bulk” PZT ceramics. This was done because it is experimentally observed that even single impact between a foot and the ground largely affects the whole system response of micro-scale robot prototypes. Since the impact models in other fields did not provide a sufficient approximation for the micro-robotic impact response, this task proposes a theoretical impact model using a modal coordinate system. Experimental

verification is again presented to support the hypotheses regarding the proposed theoretical impact model.

The final task is to apply an empirical modeling procedure to one of the thin-film walking micro-robot prototypes, a millipede robot, and to conduct example simulation studies with the obtained dynamic model. Additionally, simulation studies using the obtained dynamic model are conducted to analyze the influence of various ground conditions on the walking dynamics by perturbing short-range forces and characteristics that were previously defined to represent such ground condition.

CHAPTER 1

INTRODUCTION

1.1 Background

For the last couple of decades, micro-technology has flourished and provided remarkable improvement in human society throughout various areas such as medicine, communication, portable electronic devices, and entertainment by providing small, accurate sensing, actuation and control capabilities to mechanical and electronic systems. Growth of such technology has inspired development of mobile micro-robotic systems that would have the capability to conduct tasks that human or other ordinary-size robots cannot carry out. Such tasks, for example, could be operations such as exploration and surveillance in small areas such as inside narrow pipes, the inner parts of the body, or debris in disaster areas.

As one of the representative fields of micro-technology, microelectromechanical systems (MEMS) applied to micro-robotics have shown many benefits. These include small dimensions of systems with high fabrication precision, easy communication with electrical elements in semiconductor chips, low power consumption, and batch fabrication processing potentially granting mass production with lower cost. For this reason, numerous MEMS-based micro-robots have been developed in various fields. During the 1990s, a few first-generation MEMS robotic systems were developed that were highly innovative at that time. For instance, the first batch-fabricated walking micro-robot, shown in figure 1.1a and which uses electrothermal actuation, was introduced in 1999 by Stemme et al [1]. The proposed robot had large weight bearing capability of 2500 mg which is 30 times larger than the weight of the robot. However, like other initiative micro-robotic systems at that time, there existed significant limitations in that the leg motion was small and unidirectional, and the actuators used were single degree of freedom, which limited the robot’s maneuverability and robustness of movement against the geometric profile of the ground.

In the 2000s, improved technologies in various fields enabled further miniature of device size and diversification of designs and actuation methods. For example, a bio-mimetic approach adapting motions of fish [2], a novel design using electrostatic fields for smaller device size and controllability [3], and a biomedical robot for surgical operations using electromagnetic actuation [4], shown in figure 1.1b-d, were introduced. However, for all mobile MEMS micro-robots that have been introduced to date, movement is accomplished either by single leg strokes and unidirectional or the workspace was limited to specific areas where specific body forces, such as strong electrostatic fields between electrodes [3] or magnetic fields [4], could be applied.

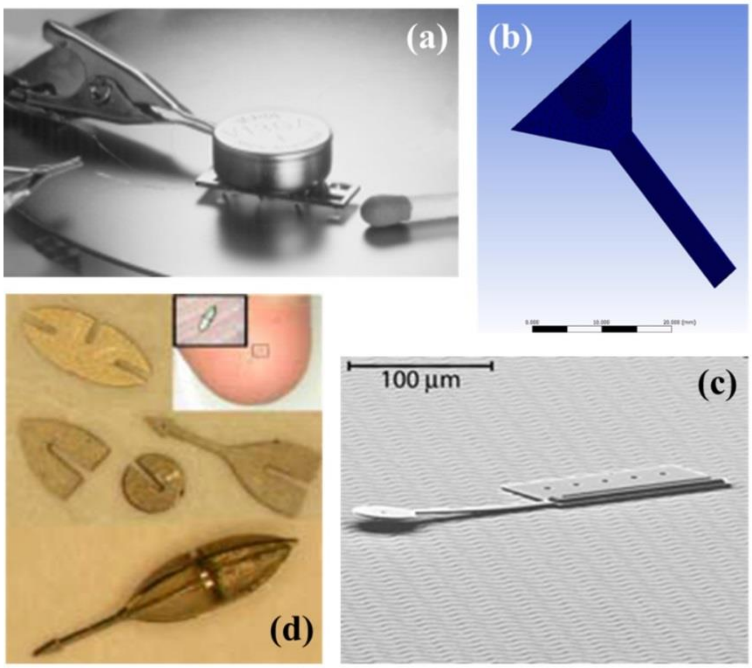

Figure 1.1 Various micro-robots in other studies
(a) Electrothermally actuated walking micro-robot (1999) [1],
(b) fish-like underwater micro-robot using Ionic Conducting Polymer Films (ICPF) (2011) [2],
(c) micro-robot using Untethered Scratch Driver Actuator (USDA) (2006) [3],
(d) untethered biomicro-robot using electromagnetic fields (2006) [4]

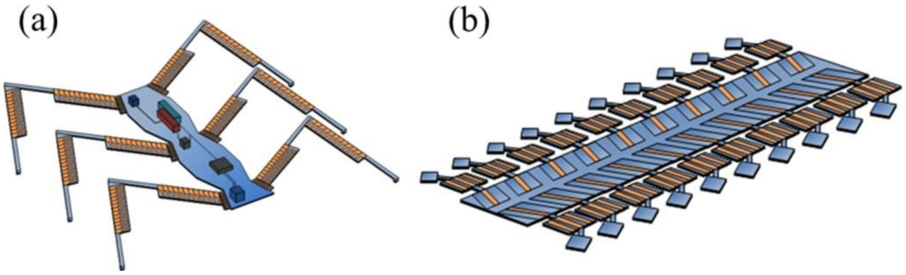

Figure 1.2 Conceptual diagrams of thin-film piezoelectrically walking micro-robots: (a) hexapod design (b) millipede design

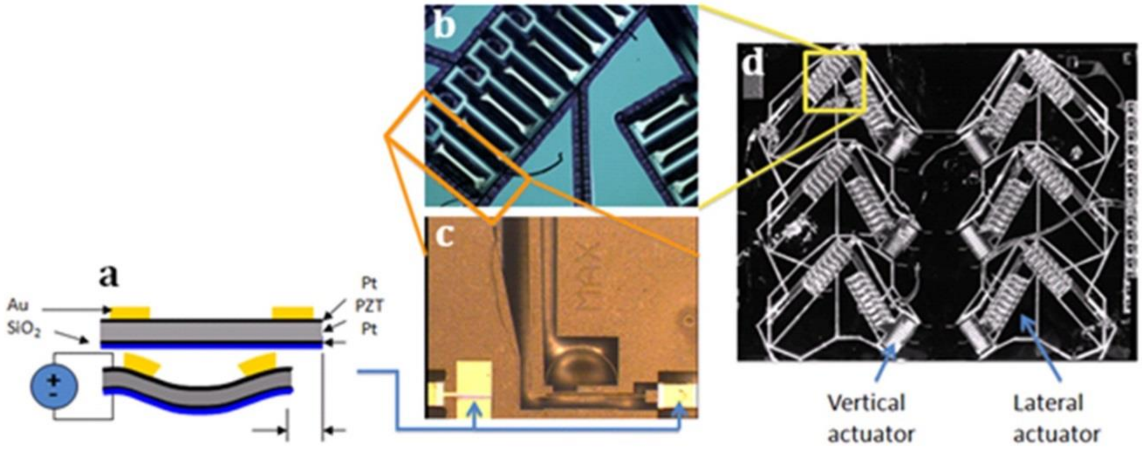

Figure 1.3 Hexapod micro-robot
(a) Actuation of single PZT strip, (b) A lateral actuator at the knee joint consisting of multiple segments, (c) Zoomed-up figure of single segment, (d) Top view of the entire system

In order to break through these barriers to micro-robotic range-of-motion, the Microsystems group in the University of Michigan, Vibration and Acoustics Laboratory, has designed and developed thin-film micro-robots, shown in figure 1.2, which have comparatively large displacement with multiple-degrees-of-freedom (m-DoF) motion for each leg, as shown in figure 1.3. As illustrated in the figure, arrays of piezoelectric actuators generate large rotation at each joint working as single revolving actuator and this mechanism creates large displacement at the end of a leg. Also shown in figure 1.4 is a leg that has both joints of vertical actuators and lateral actuators so that a single leg operates with m-DoF motion. Detailed explanations of single leg motion have been previously described [5].

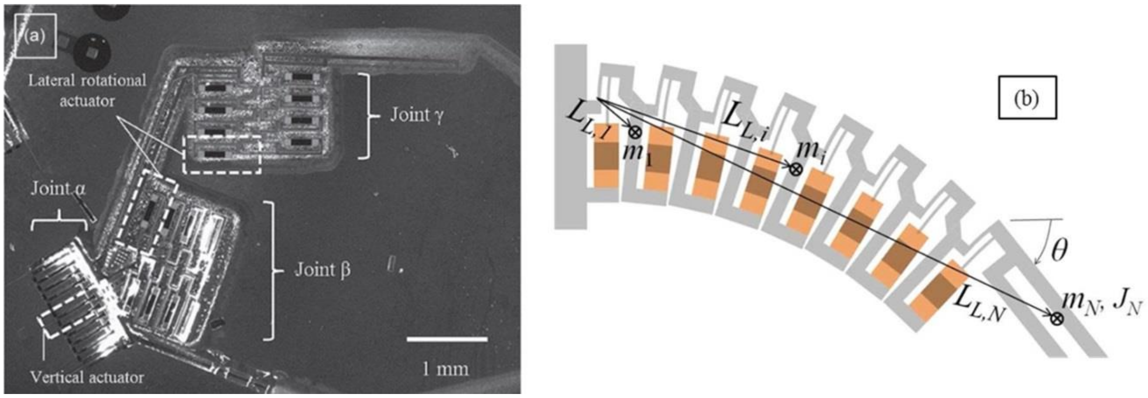

Figure 1.4 (a) Optical image of a fully released m-DoF leg [5] (b) conceptual diagram of arrays of piezoelectric actuators [6]

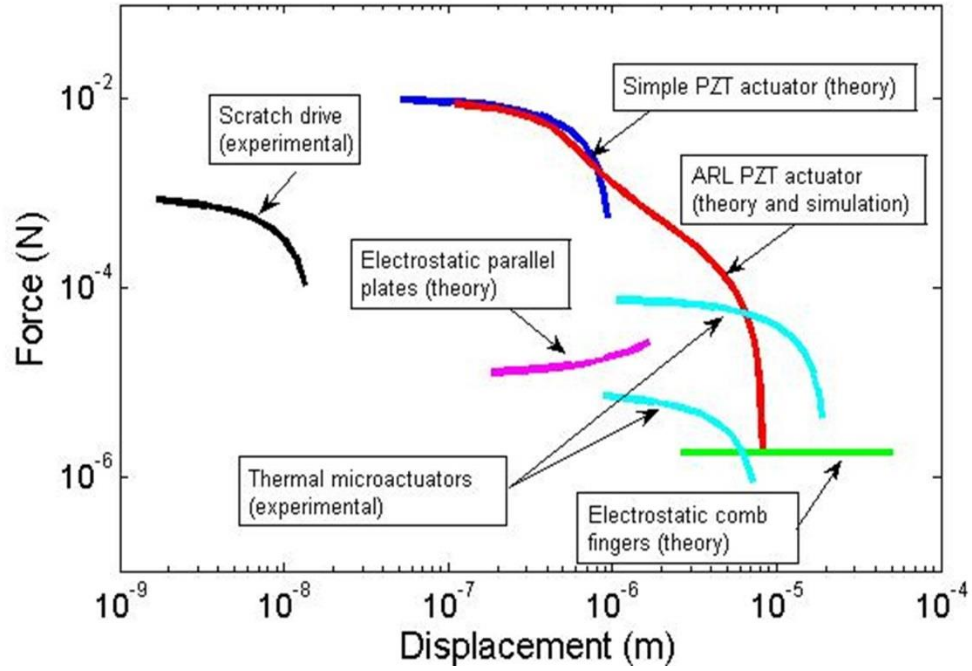

Figure 1.5 Force-displacement curves for common MEMS actuators, 20 V

For the actuation method in these robots, piezoelectricity is selected due to various benefits such as rapid response, large force generation, and low power consumption, which are very desirable features for mobile systems. Figure 1.5 shows that piezoelectric actuation has overall good force-displacement ratios over other actuation methods, given equal actuator area and applied voltage.

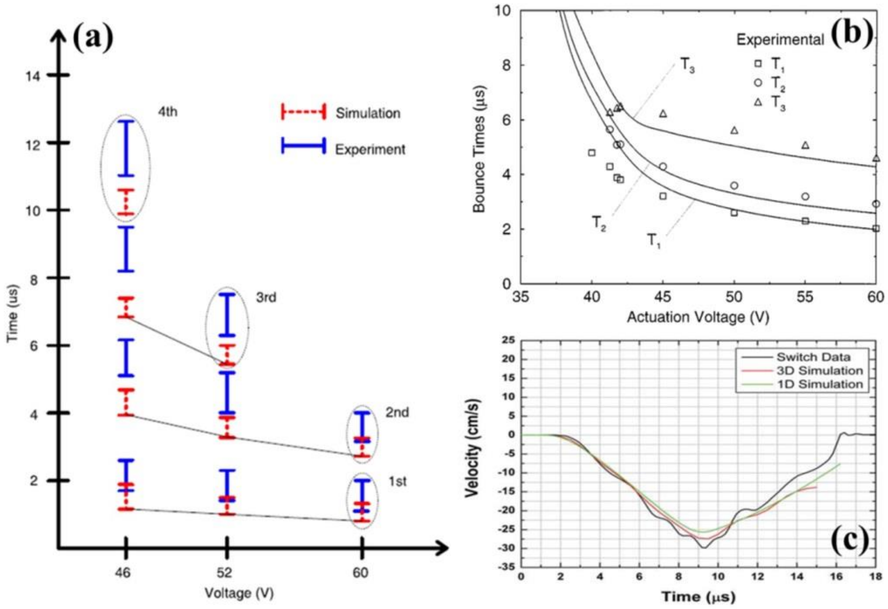

Figure 1.6 former studies on dynamic contact interaction in MEMS
(a) Contact periods comparison [7], (b) Bounce time comparison [8], (c) Predicted displacements from the 1-D and 3-D models compared to measured data [9]

Should highly mobile walking robots be achieved, with low power consumption and fast leg response, it is anticipated that their interaction with ground during dynamic walking will be complex. Analysis of contact dynamics between surfaces in MEMS devices has also been an active area of MEMS research, but results are likewise limited. Typically, either only certain features of a response can be predicted. Figure 1.6 shows a few key examples of the prior works in contact dynamic modeling of micro-devices, implying that the former studies exhibit limited model validations such as single parameter comparison [7][8], or comparison of time-domain responses to single input signal during a very limited time duration [9][10]. In addition, nearly all prior MEMS contact models are intended for devices with fixed, known geometries, which is very different from the situation for foot-terrain interaction of a mobile micro-robot.

1.2 Problem Statement and Tasks

Due to numerous factors in micro-systems, it is very hard to model dynamics of mobile micro-robotic systems. Benefits of dynamic modeling for walking micro-robots, not to mention other micro-devices experiencing impact between surfaces, include:

- The ability to conduct numerical analysis using mathematical/engineering methods to aid in robot design or gait optimization.
- The availability of a simulation model on which to apply various conventional and/or novel control techniques.
- The opportunity to identify/quantify effects of external environment on system dynamics and validate theoretical approaches to increasing device feasibility

Hence, the research objective of this work is to establish dynamic modeling and identification procedures for piezoelectrically actuated walking micro-robots making contact with their surroundings. These models should provide some fair level of accuracy in predicting micro-robot motion, as evaluated by experimental comparisons.

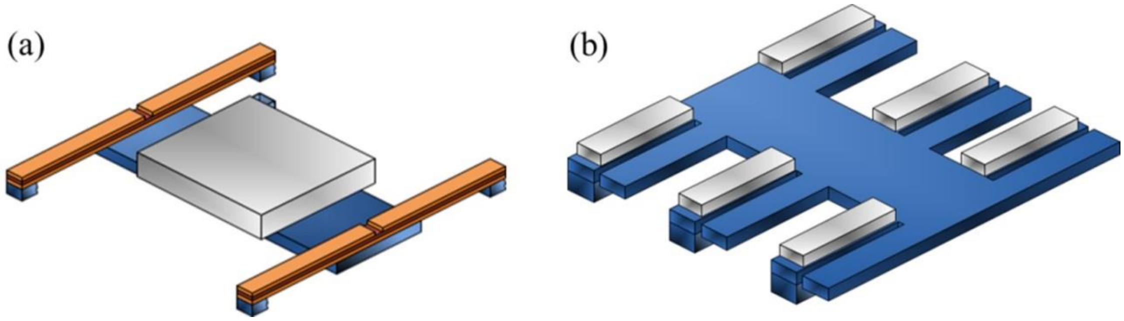

Figure 1.7 Micromachined structures operated with “bulk” piezoelectric ceramics (a) Quadruped “Bulk” PZT Robot (QBPZTR), (b) Hexapod “Bulk” PZT Robot (HBPZTR)

As will be introduced in more detail in the corresponding chapters, former studies on dynamic contact interaction in MEMS have presented very limited explicit validation with measured system responses to ranges of inputs or external conditions, and almost no such studies for piezoelectric actuation. Therefore, this work starts with testing on a simple micro-cantilever test structure mimicking contact between a robotic foot and the ground [11]. This task establishes a procedure for dynamic modeling of contact interaction of a micro-device without knowledge of contact surface conditions such as geometric profile, material properties and influence of ambient condition. The modeling procedure also includes contact/impact modeling as well as identification/quantification of the involving short-range contact forces based on the derived dynamic model using analysis on various experimental data sets.

Moving to mobile micro-robots, empirical observation reveals that single impacts of robot legs substantially affect the whole system dynamics, which can lead to seemingly chaotic and complicated responses. These responses are not well modeled with a single Coefficient of Restitution (CoR) at the contact point since there is no point in the system assumed to be fixed in inertial frame of reference and because contact forces are very rapidly transmitted throughout the entire structure. Therefore, even though the previous task shows that the proposed dynamic modeling procedure for a micro-device even without knowledge of contact surface conditions could present a fair approximation to the measured data, impact behavior for mobile walking micro-robot should be further characterized for plausible dynamic modeling.

Hence, in the second task, we developed more realistic robotic structures, shown in figure 1.7, which are operated with thick piezoelectric ceramics under single contact point interacting with the ground. Using these devices, a procedure is established for dynamic modeling of impact behavior on the more complex robotic systems using both an analytical approach with a modal coordinate system and an empirical approach using experimental data processing [12]. We applied the same modeling procedure proposed in the first task for characterization of structural dynamics and short-range contact forces.

Finally, the combined modeling procedure is applied to one thin-film piezoelectrically actuated micro-robot prototype, referred to as a millipede design, to begin to verify whether the proposed modeling also works for more delicate and sensitive micro-robotic devices. Additionally, experimental observation is conducted to evaluate design optimization of joint angles and leg link lengths for a specific leg configuration.

Finally, based on the validated model, a series of simulation studies is conducted to evaluate anticipated robot walking sensitivity to variation in ground conditions.

CHAPTER 2

MODEL IDENTIFICATION FOR IMPACT DYNAMICS OF A PIEZOELECTRIC MICROACTUATOR

2.1 Introduction

Contact dynamics of microsystems are often complex and difficult to model, due to the existence of various small-scale, nonlinear forces affecting the behavior of micro-scale objects before, during, and after contact. While various models have been proposed for different physical situations, when a microstructure must interact with its external environment, it may be especially useful to obtain a dynamic model without full knowledge of the geometry or properties of the interacting surfaces. In this paper, a model is developed for contact dynamics of a silicon proof mass driven by a piezoelectric actuator into contact with an underlying, irregular silicon “ground” surface. The geometry of the proof mass and the piezoelectric forcing are intended to approximate contact between the foot of a terrestrial micro-robot and the terrain on which it operates. Methods for modeling and/or identifying the forces acting on such a robot foot are potentially very useful for predicting walking gait performance of prototype micro-robots based on piezoelectric thin-films.

Previous studies of contact behavior of MEMS devices have most often relied on accurate knowledge of interacting surface geometries. This is especially true of studies of scanning probe technologies, as in atomic force microscopy [13] or probe storage research [14], which has allowed extremely detailed studies of contact dynamics for such instruments. For applications with larger interacting surfaces, on the order of 10 to 1000 μm, the most prevalent area of contact modeling is for micro-electromechanical switches [7-8][10][18-22], with additional work being done on certain vibration scavenging [16] or miniature gear devices [17]. Table 2.1 shows a summary of many contact models from the literature for interacting surfaces at this scale. In all cases, the geometries of the interacting surfaces are taken to be well-known, and nearly all cases involve electrostatic forcing. A variety of models for impact, adhesion, and damping behavior have been utilized, and these have enabled accurate predictions of certain specific phenomena during one or more impact events. More specifically, among closely related models in table 2.1, Decuzzi [15] and Do [7] investigated trends in adhesion/contact force for different environments and Do [7], LaRose [20], and McCarthy [8] suggested novel impact/bounce models over various substrate conditions, which are used to inform the lumped-parameter modeling in this chapter. Additionally, for models based on an assumption that the geometry of the contact surfaces is well-known, close estimation of the short-ranged forces was conducted in several studies, including use of the Reynolds Equation for squeeze-film damping [8][10][15][18][20] and various adhesion/contact force models such as Johnson-Kendall-Roberts (JKR) [15] or Lennard-Jones force [21]. However, a common drawback in these models, aside from the *a priori* knowledge of geometry, is the absence of explicit experimental validation of the model over prolonged periods in the time domain, which is crucial for analysis of the influence of various small-scale nonlinear forces during locomotion of a terrestrial micro-robot.

The approach taken in the following study is to attempt to model contact behavior using simplified and parameterized models for relevant interaction forces, and to apply system identification techniques to quantify these parameters without detailed knowledge of the interacting surface geometries or properties. This approach allows a wider variety of impact phenomena to be predicted than has been achieved by most other models for devices with similar dimensions; these phenomena include presence of bouncing events, contact duration, and oscillation amplitudes during periodic operation. Naturally, the limitation of this approach relative to prior works is that the model parameters cannot at this time be predicted from basic material properties, although prior works provide information on which small-scale factors to include. A second limitation of the current model is that fundamental underlying forces, such as Van der Waal's force, may be obscured in lumped parameter representations. Meanwhile, another advantage and difference between the model to be presented and other prior models is that electrostatic forcing, one of the dominant factors in most micro-electromechanical switch models, is nearly negligible for the piezoelectric test structure being analyzed, which in some situations makes other small-scale phenomena more impactful on device response.

Table 2.1 Comparison of features included in contact models for impact of fixed surface and actuated device 0.01-1 mm in size
Abbreviations: ES – electrostatic; EX – external; SF – squeeze-film; PE – piezoelectric; L – lumped dynamics; D – distributed dynamics; M – modal dynamics; CoR – Coefficient of Restitution; VdW – Van der Wals; TD – time dependent (empirical).

Authors	Forcing	Dynamics	Damping	Impact	Adhesion	Experimentally validated:
Wang et al., [10]	ES	L	SF	Asperity	-	Threshold for bouncing
Decuzzi et al. [15]	ES	D	SF	VdW	VdW	-
Do et al. [7]	ES	D	SF	Elastic/ plastic	-	Periods of contact
Park et al. [19]	ES	M	SF	Lagrange	-	Feedforward control gains
LaRose et al. [20]	ES	D	SF	CoR	-	Transient response match
McCarthy et al. [8]	ES	D	SF	Spring	-	Bounce times vs. voltage
Granaldi et al. [21]	ES	L	L	VdW	VdW	-
Zhang et al. [22]	ES	L	L	Spring	-	Freq. response amplitude
Guo et al. [15]	ES	D	SF	VdW	VdW	Open/closed switch times
Czapleski et al. [9]	ES	L	L	-	-	Transient before impact
Field & Epp [16]	EX	M	L	Stochastic	-	Statistical properties
Current work	PE	L	SF	CoR	TD	Time response trajectory for a range of periodic inputs.

2.2 Test Structure and Instrumentation

The test structure used for contact model development consists of a simple lead-zirconate-titanate (PZT) unimorph attached to a rigid silicon proof mass, as shown in figure 2.1. The unimorph is a composite thin-film stack of a silicon dioxide base layer, platinum bottom electrode, chemical-solution deposited PZT active layer, top platinum electrode, and structural gold layer. The active portion of the cantilever is 750 μm long and 100 μm wide, while the proof mass is 150 μm long by 100 μm wide, and is formed from the device layer of a silicon on insulator wafer with 10 μm thickness. The thickness of PZT layer is 0.7 to 1 μm with about 15 V for its breakdown voltage. Foot dimensions and first resonant frequency of the test structure are selected to approximately match the foot dimension and first resonant frequency of prototype micro-robotic leg joints [23], produced by the same fabrication process as robot protoypes and shown in figure 2.1b; the fabrication process is the same as that previously presented in [24][25], and was performed at the U.S. Army Research Laboratory.

The cantilever test structure is released from the silicon substrate in an isotropic XeF_2 silicon etch, which gives rise to an irregular and unknown silicon geometry beneath the proof mass. Identical test structures with the cantilever physically removed after fabrication indicate that the primary contact region is a ridge at the center of the proof mass, as would be expected from isotropic etching, but exact length and height vary from device to device. During operation, the bottom platinum electrode is used as ground, to minimize electrostatic forces between cantilever and ground, helping to isolate contact behaviors, while the active voltage input is applied to the top platinum electrode. During experimentation, static displacement of the cantilever was measured using an optical profilometer, (LEXT OLS4000), while dynamic displacements were measured at the center of the cantilever and center of the proof mass using a laser Doppler vibrometer (Polytek PSV-400). Figure 2.2 shows a diagram of the experimental setup.

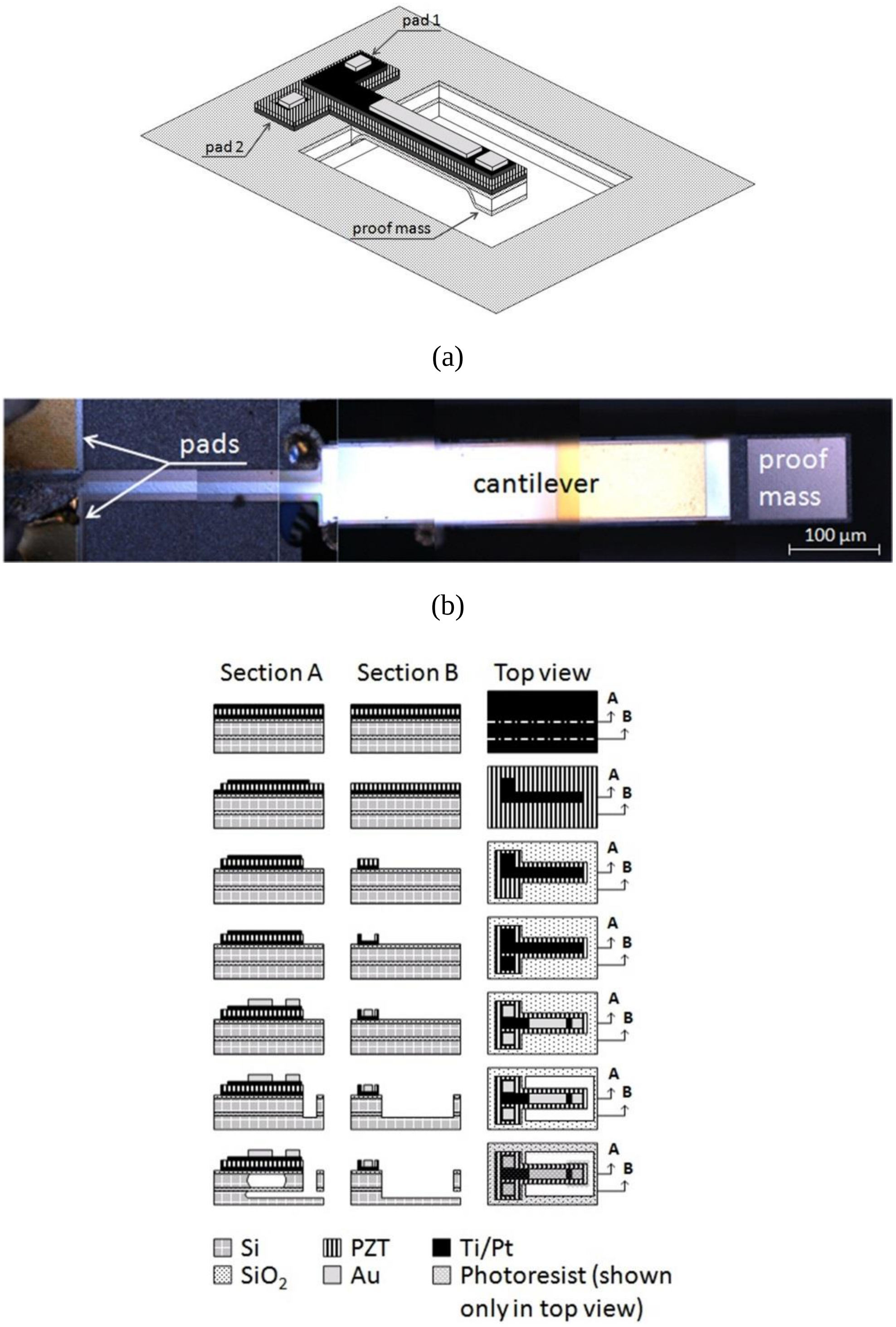

(a)

(b)

(c)

Figure 2.1 (a) Micro-cantilever test structure, (b) image of cantilever from optical microscope, (c) fabrication process

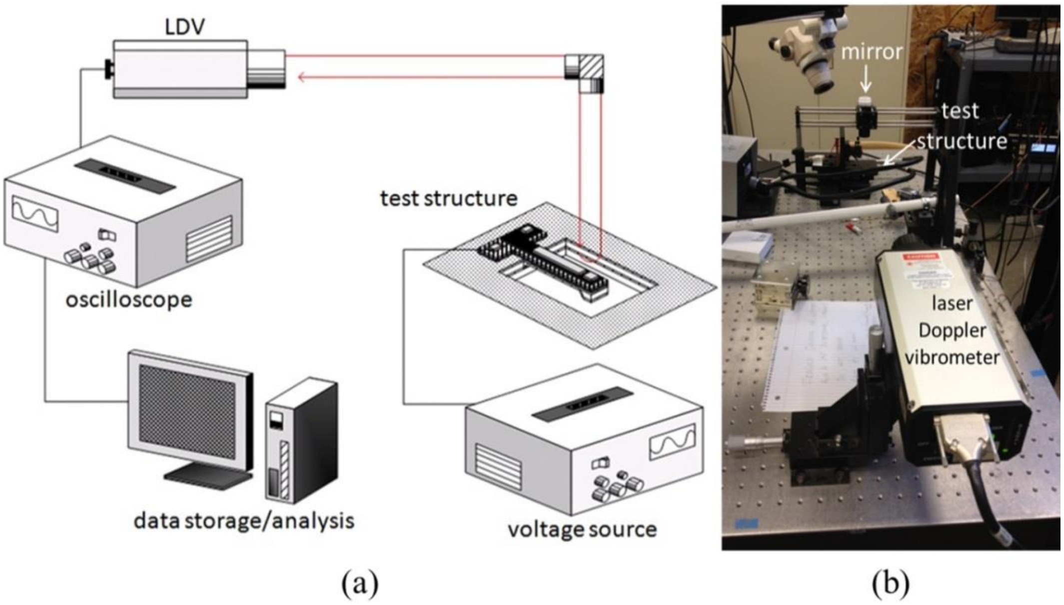

Figure 2.2 Measurement instruments and experimental setup: (a) schematic view (b) photograph of the laser Doppler vibrometer setup

2.3 System Model

The system model consists of a lumped parameter model approximating the modal dynamics of the test structure, an empirically-derived model for internal forcing applied by the piezoelectric thin-film on the cantilever beam, and parameterized squeeze film damping, adhesion, and impact models for ground interaction.

2.3.1 Structural Dynamics

The structural dynamics of the cantilever beam and proof mass are modeled in the form

$$\mathbf{M}\ddot{\mathbf{x}} + \mathbf{B}\dot{\mathbf{x}} + \mathbf{K}\mathbf{x} = \mathbf{U} \tag{2.1}$$

where **M**, **B**, and **K** are linear mass, damping, and stiffness matrices, respectively, and **U** is a vector of forcing inputs. For convenience, the state vector of the system, **x**, is chosen to be second order, with states x_c, displacement at the center of the cantilever, and x_p, displacement at the center of the proof mass (i.e., $\mathbf{x} = [x_p \;\; x_c]^T$). While this allows only the two most prominent vibration modes of the system to be captured in the dynamic model, these states are both simple to measure using available instrumentation, and the forcings to the system are approximately decoupled, into forces acting on the cantilever and proof mass respectively. This allows **U** to be modeled in the form

$$U = \begin{bmatrix} u_{c0} + u_{c,pzt}\left(V\left(t^- \mid t^- < t\right)\right) \\ u_{p0} + u_{p,g}\left(x_c, \dot{x}_c, t\right) \end{bmatrix} \tag{2.2}$$

where u_{c0} and u_{p0} are fixed, constant sources of structural deformation due to residual stresses from the fabrication process, $u_{c,pzt}$ is the sum of internal driving forces in the cantilever beam, which is a function of the applied voltage to the system, V, and influenced by the history of that voltage input up to the current time, t, and $u_{p,g}$ is the sum of external forces generated through interaction with the ground, which depends on position and velocity of the proof mass.

Because the neutral position of the system when no voltage is applied is dependent on the voltage history of the piezoelectric film, the zero positions for x_p and x_c are defined by applying a specified voltage function prior to each identification experiment, namely a polarization signal, $V_{pole}(t)$ represented by

$$V_{pole}(t) = \begin{cases} 10, & t < 0 \\ 0, & t \geq 0 \end{cases} \tag{2.3}$$

Then, the neutral position of the system is defined as the solution to

$$\mathbf{K}\mathbf{x}_0 = \begin{bmatrix} u_{c0} + u_{c,pzt}\left(V_{pole}(0)\right) \\ u_{p0} \end{bmatrix} \tag{2.4}$$

or in other words, zero positions are the position of the cantilever and proof mass in air after poling the PZT film at 10 V (in practice, 10 V is applied for 10 minutes, with at least one minute before measurement of cantilever and proof mass position by optical profilometry or LDV). Then, the dynamic system to be analyzed in terms of contact dynamics is described by differential states, $\delta\mathbf{x} = \mathbf{x} - \mathbf{x_0}$ and $\delta\mathbf{u} = \mathbf{u} - \mathbf{u_0}$, and differential forces, $\delta u_c(t)$ and $\delta u_p(t)$,

$$\begin{aligned}&\mathbf{M}\delta\ddot{\mathbf{x}} + \mathbf{B}\delta\dot{\mathbf{x}} + \mathbf{K}\delta\mathbf{x} \\ &= \begin{bmatrix} u_{pzt}\left(V\left(t^- \mid t^- < t\right)\right) - u_{pzt}\left(V_{pole}\left(0\right)\right) \\ u_g\left(\delta x_p, \delta\dot{x}_p, t\right) \end{bmatrix} \\ &= \begin{bmatrix} \delta u_c\left(t\right) \\ \delta u_p\left(t\right) \end{bmatrix}\end{aligned} \tag{2.5}$$

This formulation thus eliminates the effects of constant sources of strain from the model (such as residual strain in non-active thin-films) and leaves for further identification models for piezoelectric forcing and ground interaction. Numeric values for **M**, **B**, and **K** are obtained from conventional modal analysis with a low voltage (1 V) swept sine input, using the circle fit method [26]. The most prominent resonant peaks for the experimentally tested system occur at 623 and 6424 Hz.

2.3.2 PZT Model

The forcing applied to the cantilever by the piezoelectric thin-film as a function of voltage, equivalent to a net force applied to the cantilever beam relative to the reference force producing the neutral deflection after poling, i.e.

$$\delta u_c\left(t\right) = u_{pzt}\left(V\left(t^- \mid t^- < t\right)\right) - u_{pzt}\left(V_{pole}\left(0\right)\right) \tag{2.6}$$

from (2.5), is a very complex function of the voltage signal experienced by the PZT film up to the current time. This is especially true when both positive and negative electric fields are in use, as the polarization state of the film itself may vary from that achieved after poling. However, for strictly periodic input signals with a limited range of amplitudes used in the current work it was found that the piezoelectric forcing could be approximated by comparatively simple and experimentally identifiable polynomial functions, such that

$$\delta u_c(t) \approx g_c\left(V(t), \dot{V}(t)\right) \tag{2.7}$$

Here, g_c is a empirically-fit hysteresis model for PZT actuation gain from static bending tests.

The function describing g_c is identified as a function of voltage by solving the equation

$$K_{1,1}\delta x_c = g_c\left(V, \dot{V}\right) \tag{2.8}$$

for a number of voltage cycles and fitting polynomial curves to the hysteresis loops. Here $K_{1,1}$ is the estimated stiffness of the cantilever from the structural model and $\delta x_{c,}$ the displacement of the center of the cantilever from its zero position, is being measured during static bending tests.

Figure 2.3a shows static displacements versus voltage for a cantilever beam stepped in increments from 0 V (after poling) back to -8 V, up to -8 V, and back to 8 V. As it illustrates, position of the proof mass is bound when voltage reaches close to 8 V and it stays at the same position until voltage falls back to 2 V. This is attributed to adhesion and this hypothesis is strengthened by the fact that the proof mass seems to be "released" from the "ground" surface when voltage becomes negative. Figure 2.3b shows the second experimental data where the range of voltage is from -6 to 6 V, which just avoids contact with ground for quasi-static motion and thus features no adhesion effect, as visible in the continuously changing in position of the proof mass during voltage drop from 6 V to 0 V. While there is substantial variation from cycle to cycle, as visible in figure 2.3c, for the main purpose of contact modeling, an average empirical fit for g_c was found as

$$g_c(V) = \begin{cases} 0.0076V^2 - 0.6062V - 0.6350 & \text{if } \dot{V} < 0 \\ 0.0016V^3 - 0.0255V^2 - 0.7057V + 1.4796 & \text{if } \dot{V} > 0 \end{cases} \tag{2.9}$$

It should be noted that the full trajectory of the proof mass positions over a larger range of voltage would look like the plot on the bottom left corner of figure 2.3c, which is a typical "butterfly" feature of bipolar hysteresis of thin-film PZT actuators. For this study, only one side of the butterfly curve is in use, and the curve here is not symmetric along the 0 V line due to some inherent polarization of the PZT thin-film during the fabrication process.

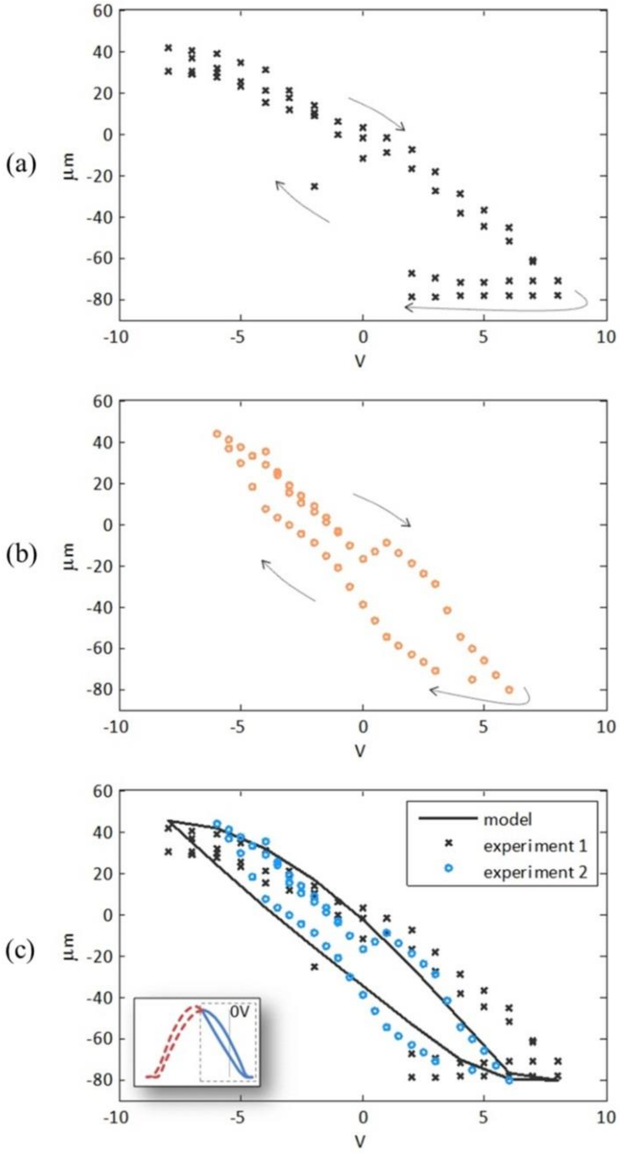

Figure 2.3 Hysteresis curves from cantilever testing here: (a) experiment 1, voltage range -8 V to 8 V, (b) experiment 2, voltage range -6 V to 6 V, (c) gain model and a fully interpolated hysteresis curve on the bottom left corner

Because error in the piezoelectric model can produce error in the parametric models for contact dynamics, at the conclusion of parameter identification a sensitivity analysis to altering the piezoelectric model is performed by varying the presumed zero position of the proof mass above the ground surface and repeating parameter identification as if that had been the true zero position of the structure (in effect shifting the piezoelectric gain to the extent of its experimental range). As will be discussed later, the contact model parameters prove relatively insensitive to changes in the piezoelectric model, although improved hysteresis modeling is a potential area of future work for modeling of the system as a whole, especially when a wider range of voltage amplitudes may be applied.

2.3.3 Impact Modeling

The goal of impact modeling is to identify a comparatively simple, parameterized model describing behavior when the proof mass at the tip of the cantilever impacts with the underlying ‘ground’. Although this test structure used for model development can only interact with one surface, conceptually it should be possible to adjust the parameters describing the impact model to describe a variety of other surface interactions. The impact model developed here consists of lumped-parameter squeeze-film damping and adhesion models, together with a coefficient-of-restitution test for bouncing.

When the proof mass is not in contact with the ground, $\delta u_p(t)$ is estimated using a parameterized squeeze film damping equation,

$$\delta u_p = C_s \frac{\dot{x}_p}{\left(x_p + g_p\right)^3}, \quad x_p > -g_p \tag{2.10}$$

where g_p is the effective distance between the proof mass and ground at the zero position for the proof mass, and C_s is a lumped coefficient incorporating viscosity and other squeeze-film damping factors. C_s and g_p are tuned experimentally during the system identification procedure in the following section. The value for g_p is not identical to the value for d_p which is the distance between the proof mass zero position and ground because the uneven shape of the underlying silicon results an effective non-zero gap when the proof mass is in contact, as shown schematically in figure 2.4.

If the proof mass comes into contact, the external ground interaction force becomes a function of adhesion to ground, which is given a general form.

$$\delta u_p = f_a\left(t - t_c\right),\ x_p = -d_p \tag{2.11}$$

where t_c is a the time at which the current period of contact began, and f_a is an experimentally identified function for adhesion force, to be identified.

To determine whether the proof mass sticks or bounces at impact, a coefficient of restitution model is used. First, at the moment of impact, the estimated bounce velocity is calculated from

$$\dot{x}_p^+ = -\alpha \dot{x}_p^- \tag{2.12}$$

where $\dot{x}_p^-$ is proof mass velocity just before impact, $\dot{x}_p^+$ is hypothesized velocity after impact, and α is an experimentally determined coefficient of restitution. Then, the pulling-off force associated with such a change in velocity is calculated from the dynamics of the remainder of the system as

$$f_{pull} = -K_{2,1}\delta x_c - C_{2,1}\delta \dot{x}_c + K_{2,2}\delta x_p + C_{2,2}\delta \dot{x}_p \tag{2.13}$$

If f_{pull} is positive after the hypothesized bounce and is larger than $f_a(t\text{-}t_c)$, proof mass velocity is calculated from (2.12), otherwise the proof mass is taken to be in sustained contact with ground, and the adhesion force from (2.11) is applied, until $f_{pull}(t)$ at a future time exceeds $f_a(t\text{-}t_c)$.

2.4 Impact Parameter Identification

Given that structural and piezoelectric models for the system from Section 2.2 have been developed based on non-contact and static bending tests, three parameters and one function must be identified to finalize an impact model of the form proposed in (2.10) to (2.13). These are the squeeze-film coefficient and effective gap between proof mass and ground, coefficient of restitution (CoR), and adhesion force function.

CoR is most easily identified, by gradually increasing voltage to the system at a fixed oscillation frequency, in the present example 300Hz, until the proof mass just begins to impact the ground, without any sustained adhesion. A number of impact events are measured under the LDV, and proof mass velocity is calculated before and after impact. The corresponding coefficient of restitution is taken from the average value of many impacts, as shown in figure 2.5.

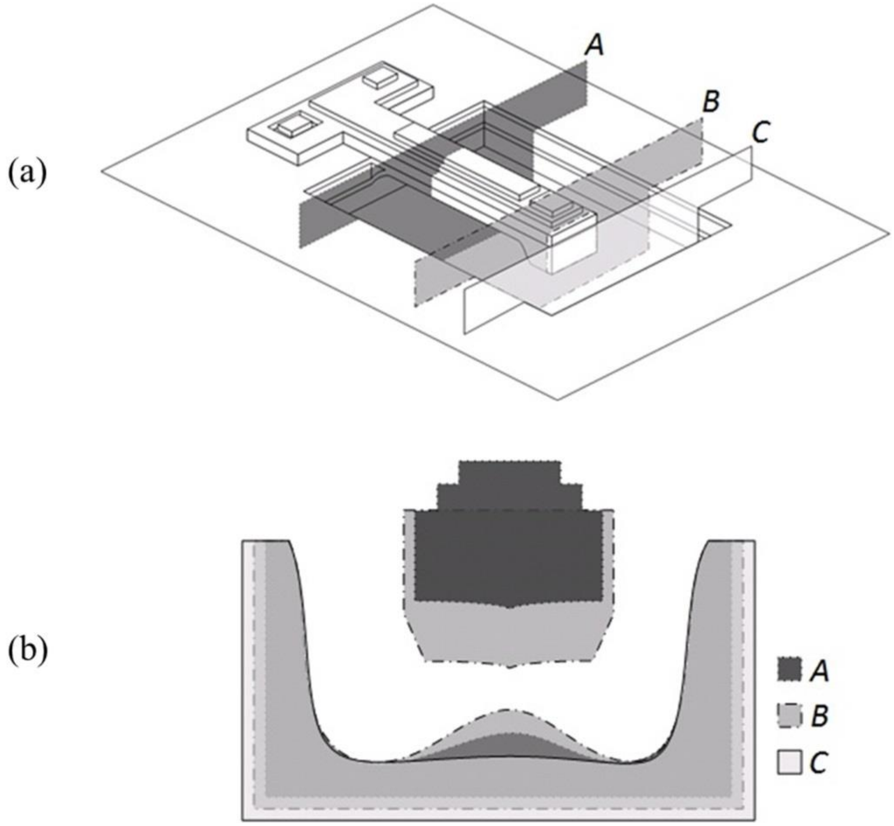

Figure 2.4 Cross-sectional diagram and expected ground surface: (a) schematic diagram of the test structure, (b) conceptual diagram of inferred cross-sections

For adhesion and squeeze film damping, a series of experiments was performed using ramped square waves. Defined in terms of frequency, voltage, and a duty cycle variable, λ, which determines the slope of the input signal, as shown in figure 2.6, the ramped square waveform was found to be effective for producing comparatively gentle contact events with gradual changes in contact time for adhesion measurements. Furthermore, immediately after break-off, the ramp-up keeps the proof-mass close to ground and accentuates squeeze-film damping effects.

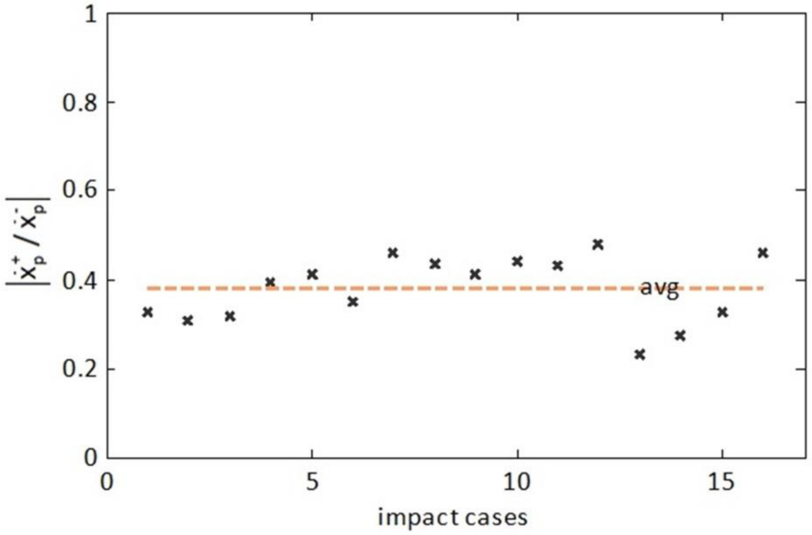

Figure 2.5 Ratio of proof mass velocity after impact to velocity before impact, for 16 sample bouncing events (300Hz square wave/300Hz sine wave)

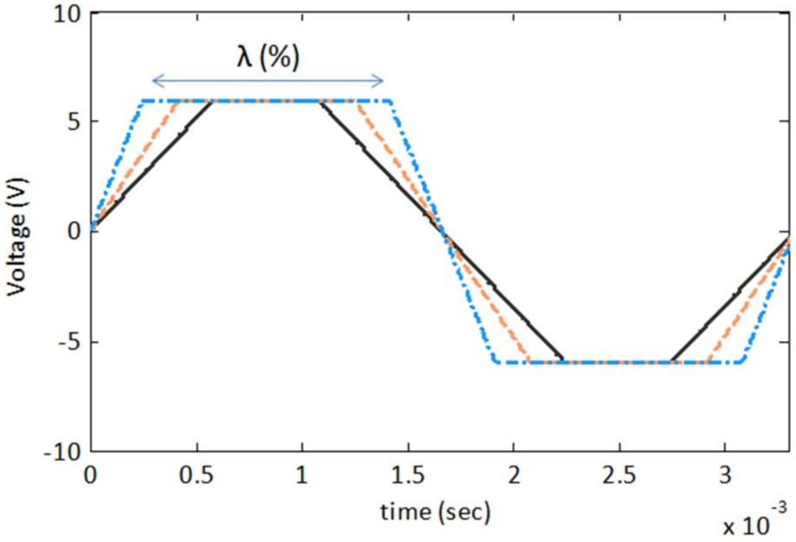

Figure 2.6 Sample ramped-square waveform used for adhesion and squeeze-film damping measurements.

To perform adhesion measurements, the pulling-off force from (2.13) acting on the proof mass is calculated using the actuator model and observed cantilever and proof mass diaplacement over the duration of a single maintained contact period. Figure 2.7 shows a sample simulation study, showing calculated pull-off force and adhesion force normalized to the driving force versus cantilever displacement.

As shown in figure 2.7, adhesion is taken to increase as contact time increases (with a linear trend proving consistent with experimental data), and the proof mass is released from the ground pulling-up force equals adhesion force. Figure 2.8 shows the adhesion force calculated from pull-off force at break-off versus contact duration for ramped square waves with varying λ at 5 Hz and 8 V amplitude. While a relatively limited range of contact durations is obtained in this manner, a linear trend in adhesion force with time is observed. This is consistent with some prior adhesion studies of microdevices, including [27-30]. Although these former studies have shown the linear relationship between adhesion and contact duration, there is not yet a fundamental explanation of the behavior. Previous studies either consider the lubricant layer between the surfaces [27-28] while others do not propose any analytical model for it but only explain the trend from the empirical observation [29]. Therefore, it seems that there is no study at this time which can provide an explicit description of such linear relationship between adhesion and contact duration where there is no liquid lubricant on the micro-scale surface.

Nonetheless, the linear trend of adhesion over contact duration, which has been experimentally observd in this work, might be describable considering other various former works on adhesion synthetically such as studies on the linear relationship between adhesion and normal force [22] and those on the correlation between adhesion and asperities of contact surfaces [28]. That is, it might be inferred that as contact time increases, by the normal force applied, so does the effective area of the elastic asperities in contact between the surfaces, consequently resulting in larger adhesion. Hence, the resulting adhesion model was identified using slope, C_a, and intesect, C_{a0}, constants as

$$f_a = C_a\left(t - t_c\right) + C_{a0} \tag{2.14}$$

Also visible in figure 2.7 is the oscillation of the of the proof mass after break-off, as it rises away from ground. This is a consequence of the sudden break-off against adhesion, and its peak amplitude and decay rate are used to fit the parameters of the simplified squeeze film damping model in (2.10). As shown in figure 2.9, by adjusting the effective squeeze film damping coefficient, C_s, and effective proof mass gap, g_p, such that the decay in oscillations are matched between the dynamic model and experimental results. Table 2.2 shows the coefficients obtained for the current test structure. Figure 2.10 shows an example of the agreement between the dynamic model with identified coefficients and a sample ramped-square wave over a full cycle period.

To check sensitivity of identified parameters to piezoelectric coefficient modeling, the above procedure was repeated assuming a piezoelectric gain function shifted by the equivalent of 20 μm of zero position of the proof mass, d_p, shown in figure 2.11. This offset was approximately equal to the maximum cycle-to-cycle deviation of static bending tests. Table 2.2 shows the comparison of contact dynamics model parameters under the two different piezoelectric forcing scenarios and this implies that the identified parameters are largely insensitive to error of the estimated piezoelectric gain behavior.

Based on the adhesion model in this work, the adhesion energy loss might be estimated by taking sum of the kinetic energy and potential energy and finding the difference at the point that the adhered proof mass detaches. Although it is not perfect since there is some energy loss due to other factors such as structural damping or squeeze-film effect, this was considered adequate to approximate the work done by the adhesion as shown in figure 2.12, and observe its significance. As illustrated in the figures, there are differences in both kinetic energy and potential energy between simulation results with and without adhesion. As shown in figure 2.12b, the area indicated with E_l implies the work done over time by adhesion.

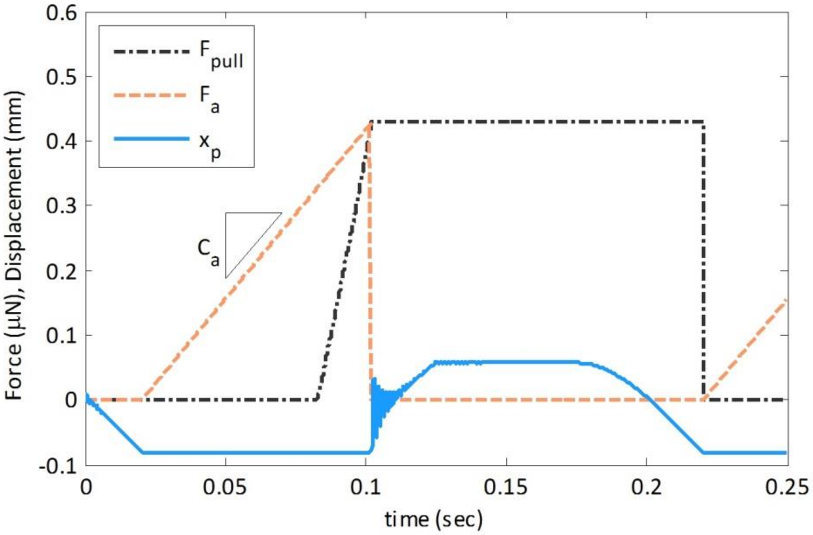

Figure 2.7 Sample proof mass position versus time with ramped-square wave, superimposed over inferred pull-off force.

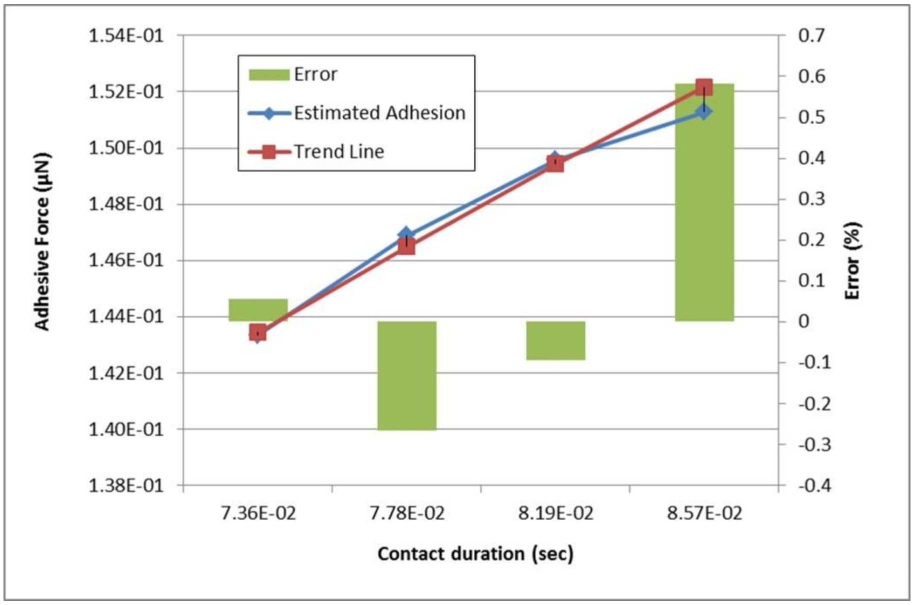

Figure 2.8 Inferred adhesion force versus contact duration for 5 Hz ramped-square waves.

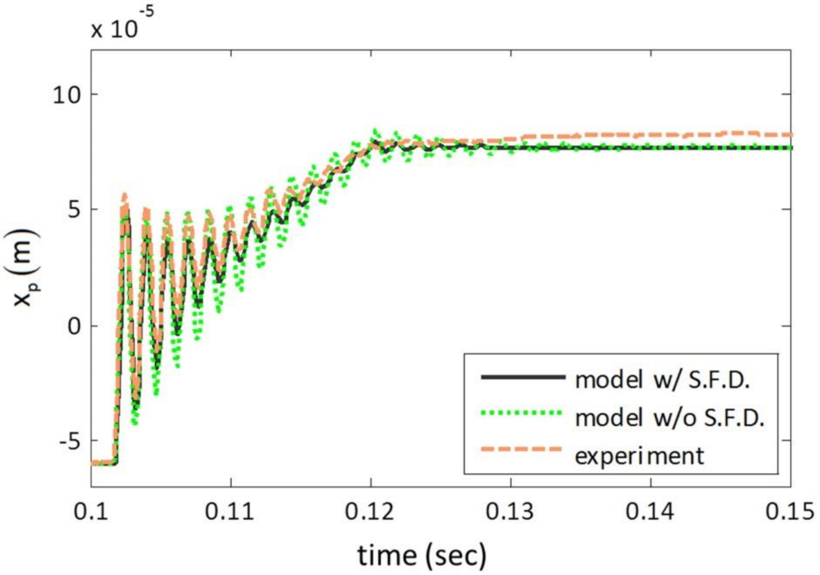

Figure 2.9 Comparison of decay in oscillations of displacement of the proof mass following break-off with and without squeeze film damping incorporated in the dynamic contact model.

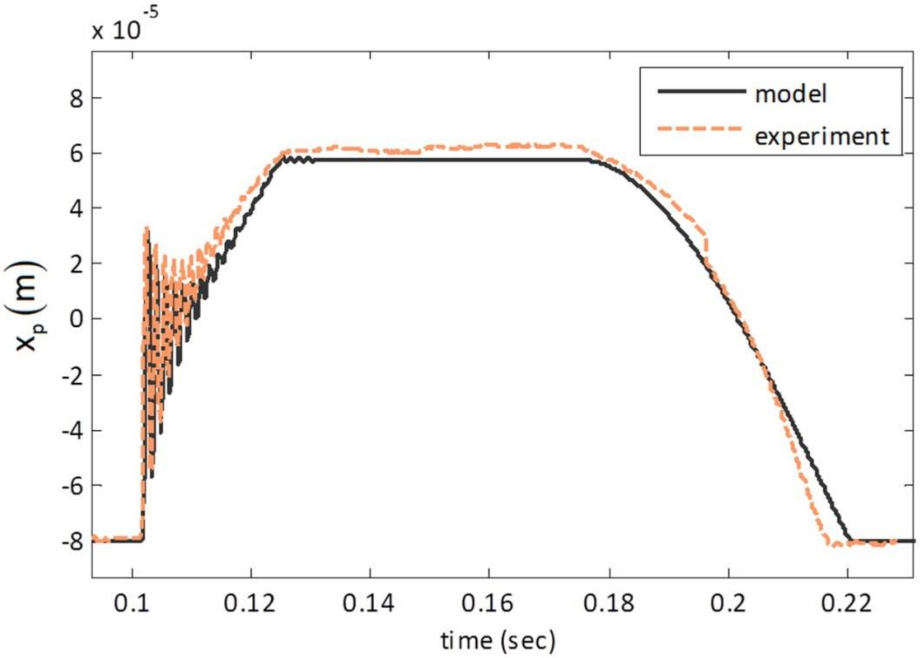

Figure 2.10 Sample response of experimental system and simulated system following model parameter identification to a ramped square wave (5 Hz, 8 V, λ = 25 %).

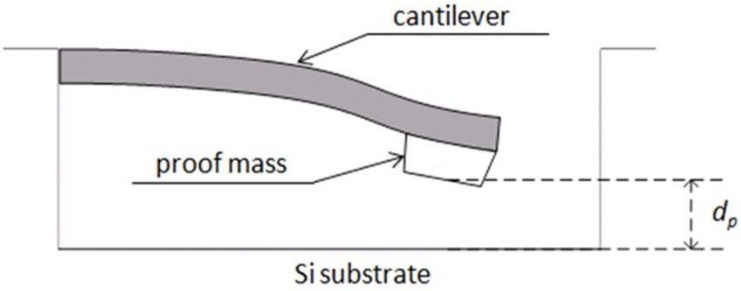

Figure 2.11 Idle position, d_p: the distance between the proof mass and the substrate surface while the system is idle

Table 2.2 Coefficients for impact model.

Coeff-icient	Forcing scenarios*		Related phenomenon	Unit
	Original	Altered		
α	0.378	0.378	CoR	-
C_a	1.700	2.120	Adhesion	μN/s
C_{a0}	$2.743\text{x}10^{-1}$	$2.550\text{x}10^{-1}$	Adhesion	μN
C_s	$1.747\text{x}10^{-15}$	$1.747\text{x}10^{-15}$	Squeeze-film damping	nNm^2s
g_p	58	58	Squeeze-film damping	μm

*Two scenarios to check sensitivity by varying the idle position of the proof mass: d_p = 70 μm for the original model, and d_p = 90 μm for the altered model

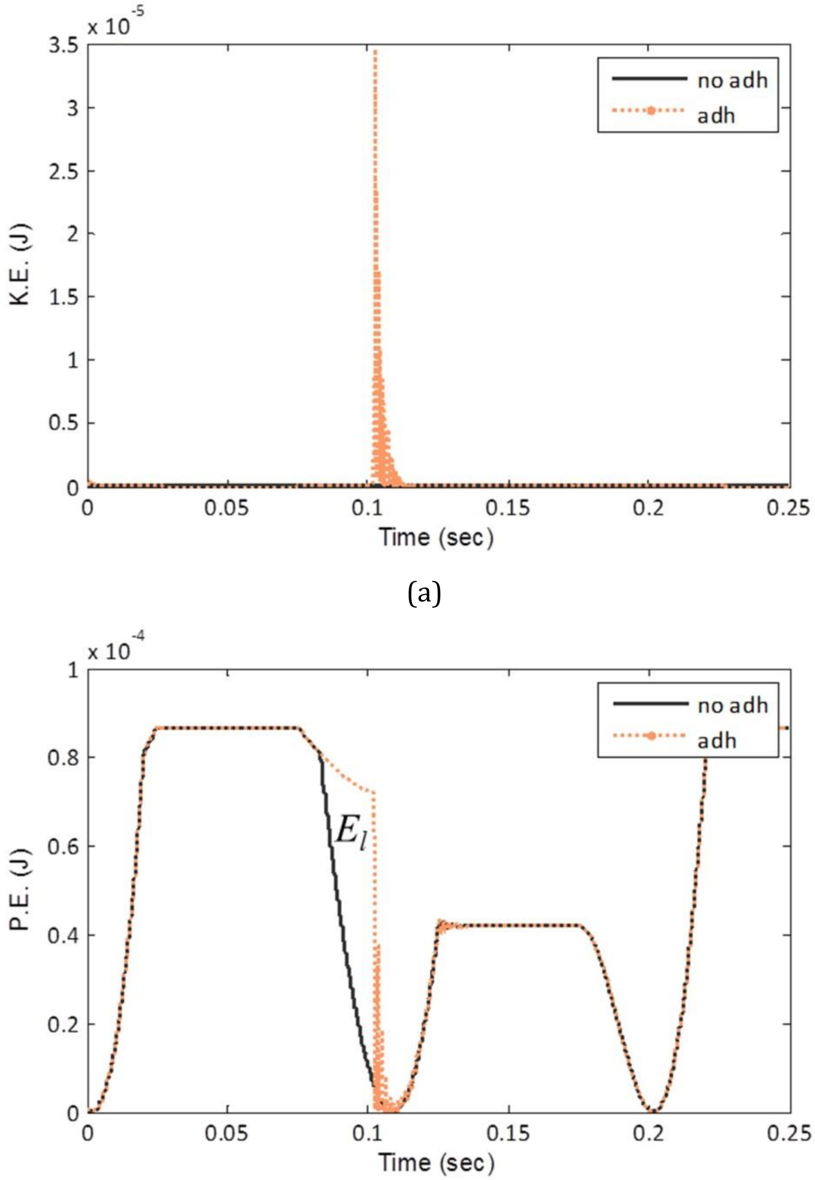

(a)

(b)

Figure 2.12 Energy comparison between simulation results with and without adhesion (a) kinetic energy (b) potential energy

2.5 Model Validation

To verify that the contact model identified from static, simple bouncing, and ramped-square wave experiments is effective for modeling a wider range of contact scenarios, several additional experiments were run with periodic input functions of varying form, frequency, and amplitude. A summary of test cases of square or sine input and 6 V or 8 V driving voltage at 5, 15, 50, and 100 Hz (16 cases total) is provided in table 2.3, with regard to presence and number of bouncing events, peak amplitude of oscillations after break-off, and contact duration. Results from the full 16 test cases are shown in Appendix A. The ranges of tested frequencies and waveforms were chosen considering the practical voltage inputs for micro-robots, which are typically low-power frequency square waves, with sine waves as a possible alternate. Voltages were limited to 6 and 8 V to avoid non-contact cases at lower voltages and higher voltage cases where piezoelectric driving force overpowered small-scale phenomena. Although some centimeter-scale micro-robots may utilize resonant frequencies, it was assumed that simple waveforms with lower frequencies would be still helpful to validate the contact model due to comparatively large time duration of contact interaction with the ground.

The simplified, lumped parameter model identified to describe system contact dynamics captures the majority of major events seen in the validation tests. Presence or absence of bouncing events was predicted correctly in all cases, although some predictions give a mismatch for the number of bounces in the cases at lower voltage inputs. About 60% of all test cases showed the identical number of bounces. Contact duration predictions are generally good, with error not greater than 30% in more than half of the test cases. Contact duration is least reliable for the cases of lower voltage input, with substantial errors seen in a few test cases. Peak oscillation error was lower than 30% in nearly all cases, with greater errors observed only for some square wave tests. Errors are attributed primarily to un-modeled minor vibration modes, particularly when excited by step inputs, and also to the complicated hysteretic behavior of piezoelectric actuation. Error may also arise from some small contribution of electrostatic attraction, primarily at higher frequencies; in the experimental setup, electrostatic force is minimized as a result of grounding the bottom PZT electrode, but if any electrostatic force exists, only its static effects are accounted for through the influence of electrostatic attraction on the calculated piezoelectric gain function. Nonetheless, even the worse test cases give a fair agreement with overall periodic time-response, as shown in figure 2.13a and 2.13b, despite the numerically quantified errors. Overall, 50% of all test cases showed less than 30% error in both peak oscillation error and contact duration predictions, and again, presence or absence of bouncing was predicted correctly in all cases.

Other representative responses are also shown in figure 2.14. Figure 2.14a shows the very close agreement between simulation and experimental results at low frequencies, using identified model parameters. At higher frequencies, such as the 50 Hz results in figure 2.14b-c, greater differences occur, with unmodeled minor vibration modes especially evident in the response to an 8 V sinusoidal input in figure 2.14c. This difference, however, does not severely increase even in higher driving frequencies as seen in figure 2.14d: the general response amplitude is quite close even when higher-mode oscillation amplitudes are off. Generally speaking, the match between simulation and real system behavior over the entire duration of periodic validation trajectories appears unusually good for a micro-scale dynamic contact model.

Figure 15 shows the small-scale contact force estimation for the 8 V, 100 Hz sine input case of which the time-series comparison is shown in figure 14d. It illustrates that the proposed model can provide the time-domain comparison of such small-scale forces and how they explicitly correlate each other along with the position of the proof mass. It is worth noting that in this scenario, all of the forces contribute significantly to system behavior.

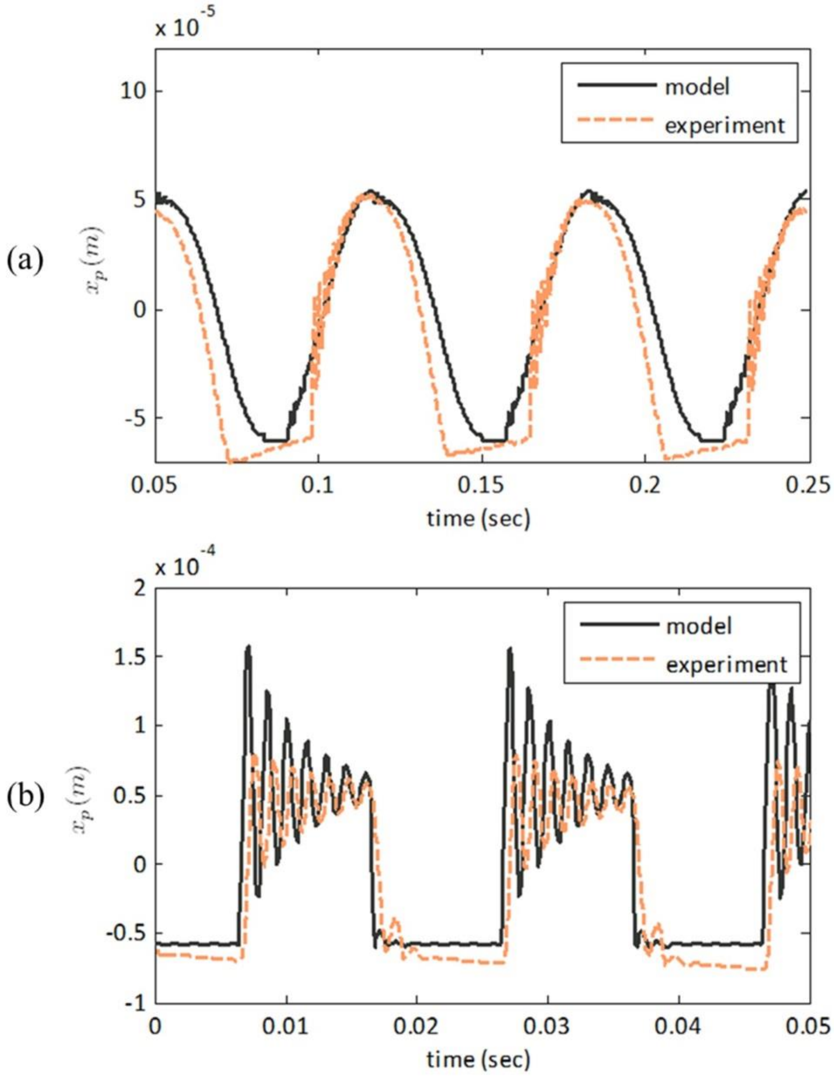

Figure 2.13 Sampling of validation test signal results, worst cases (a) sine wave 6V 15Hz, (b) square wave 6V 50Hz

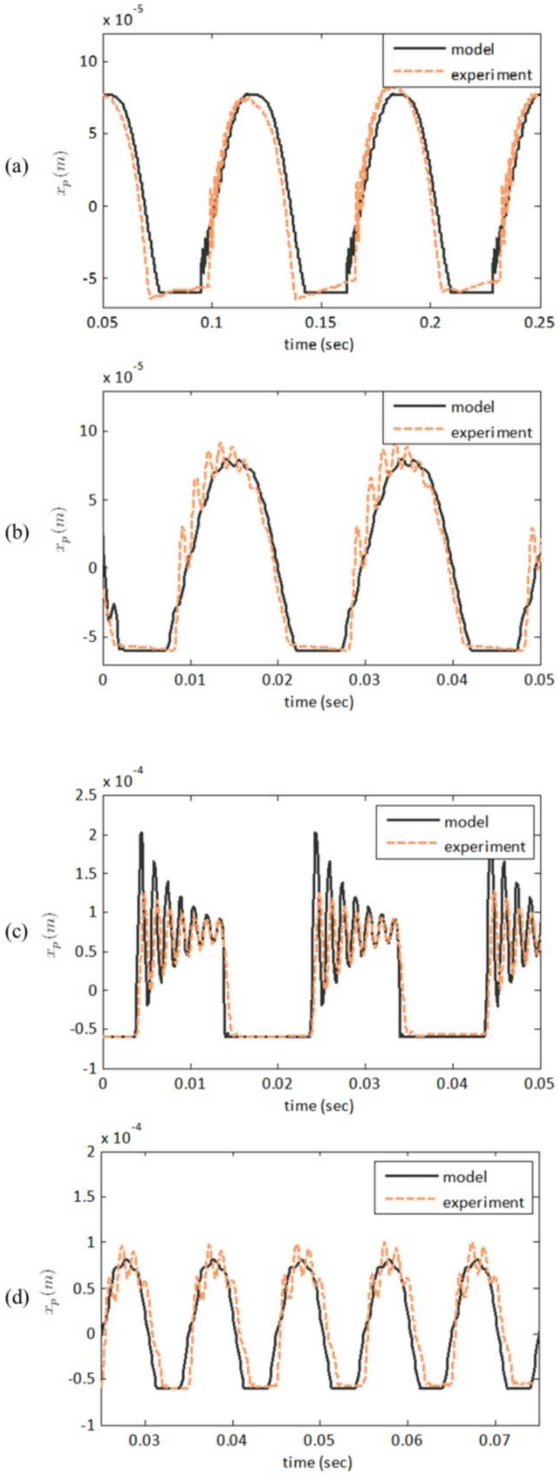

Figure 2.14 Sampling of validation test signal results, best cases
(a) sine wave 8V 15Hz, (b) sine wave 8V 50Hz, (c) square wave 8V 50Hz, (d) sine wave 8V 100Hz

Table 2.3 Summary of model validation results

Existence of bounce prediction correctly	No. of bounces correctly	Average error in no. of bounces	Average error in peak oscillation amplitude	Cases with error below 30%	Average error in contact duration	Cases with error below 30%
100%	75%	0.28	-9%	75%	20%	62.5%

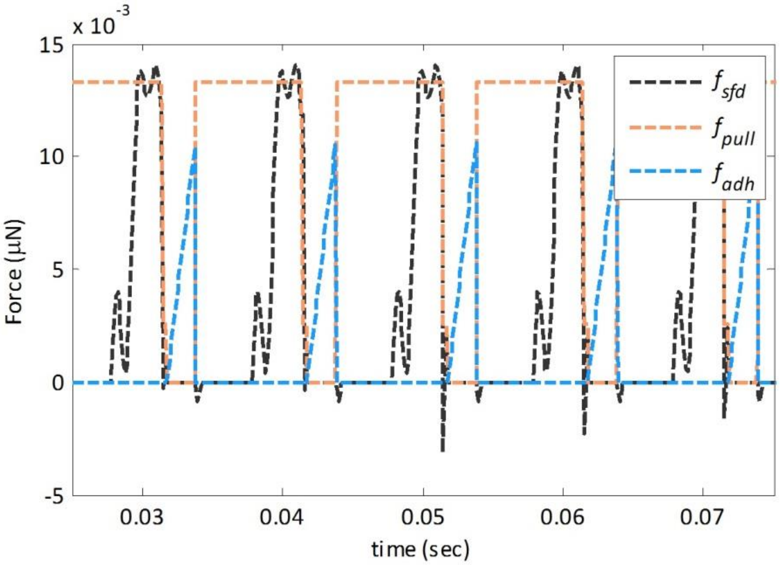

Figure 2.15 Small-scale force estimation for the case of sine wave 8V 100Hz

2.6 Discussion

The goal of this task was to develop a relatively simple model for contact dynamics of a micro-device, along with a procedure to quantify parameters in the model. Simple, in this context, indicated a primarily lumped-parameter model with a limited numbers of parameters, rather than potentially more accurate distributed or finite-element models. The major benefit of the completed model after parameter identification is that it provides good prediction in simulation of a variety of experimentally-measured transient and periodic phenomena.

The ability to replicate a variety of dynamic responses is unusual for a model of contact dynamics of a MEMS device with relatively large areas subject to surface interactions. Also important is that the model can be obtained when information about device geometries and surface conditions is limited. This model approach is able to do this, though, because it uses a subset of experimental system inputs and measured responses to quantify coefficients in a generic system model, rather than attempting to make predictions from specific system geometries and material properties. This means that the approach used here has limited utility for predicting behavior at the design stage of a given device, and is not at this time able to provide insight into the effects of material choices. On the other hand, once systematic identification is made, response of the system to alternative inputs, as provided by feedforward or feedback control, or perturbations to the contact model, made through adjustments to model parameters, can be estimated.

Regarding the specific model contents proposed in this paper, the main difference from most previous work with large contact areas in the use of piezoelectric actuation, such that electrostatic forces are less prominent than in other applications, and squeeze-film damping and adhesion forces tend to be more important. Meanwhile, while piezoelectric actuation is common in the more precisely defined contact interactions of atomic force microscopy and similar techniques, contact geometries studied here are much different. The forms for squeeze-film damping and adhesion forces have been chosen based on common forms used in references treating devices in dimensions similar to the micro-cantilever test structure tested in this paper, but reduced when possible so that each force is formulated with a simple few coefficients.   In terms of more general applications, the form for squeeze-film damping is not unusual. Meanwhile, the exact functional form (linear fit) of the adhesion force model may be dependent on the material combination used, though at least some region of linearly increasing adhesion force with contact time is often observed in other research, and the procedure for generating the pull-off force is generally applicable. Likewise, the hysteresis model for the PZT thin-film used here is entirely case specific, and much more sophisticated hysteresis models could replace it in other applications. Additionally, since electrostatic force is obscured in this hysteresis model, its contribution to the dynamics of the structure is ignored. This may contribute to error in responses under high driving frequencies. Hence, further development of the hysteresis model including the dynamic behavior of electrostatic force might reduce error. Finally, coefficient-of-restitution models for bouncing behavior have been applied to microsystems previously, but prove effective again in this work.

Similarly, the system identification approach proposed has some nice generally applicable attributes, and a few aspects that are not necessarily applicable in all cases. The provided sequence generally separates individual phenomena, although certain phenomena are not entirely isolated, such as hysteresis measurements and electrostatic forces. Likewise, if applied to other devices may not be able to reduce close range effects by shifting neutral position of other devices in the same manner that a piezoelectric cantilever can be polarized in opposite directions. One aspect of the procedure that can be useful to estimate the forces like adhesive force and squeeze-film damping force is the ramped-square input signal with various slopes, that has been designed and applied to the system.

CHAPTER 3

CHARACTERIZATION OF FOOT-TERRAIN INTERACTION OF PIEZOELECTRICALLY ACTUATED MICRO-ROBOTS

3.1 Introduction

Many micro-devices operate under the influence of inter-surface interactions, including various contact and short-range forces, which can make predicting micro-system dynamic response very difficult. This can occur because the contributions of these inter-surface phenomena to system dynamics can be very large compared to their influence on macro-scale systems. In particular, impact between surfaces typically makes dynamic modeling of micro-devices especially complicated. There have been numerous approaches to modeling the system response to impact of various micro-devices, including micro-switches [7-8][10][15][18-22], micro-gears [17], nano-indenters [33], vibration scavenging [16], and atomic force microscopy [13]. However, the existing models for impact in these micro-devices are based on a common assumption that the conditions of contact surfaces such as geometry and material properties are known, and complexity of the structures to be analyzed is often limited.

From a modeling technique point of view, the existing impact models introduced in the field of MEMS/NEMS as well as other areas of mechanical system research, including macro-scale robotics, can be sorted among several techniques. Coefficient of restitution (CoR) based models have been applied in various areas from specific micro-scale systems [16][20][35] to general systems [32][36-37] or from rigid systems [38] to flexible systems [39]. This technique has been proven efficient for models focusing on general behavior of dynamics under impacts over time instead of various time-independent factors affecting static single impact behavior. Numerical methods like asperity-based models [40] and spring force application at the contact tip [8][21] have also been used and shown good estimation of transient response to impact. Similar approaches such as compliant ground models have been also utilized in various areas such as macro-scale robotics [38][41] and MEMS switches [15]. This approach has shown good estimation in the case where the exact information on the surface geometry is assumed known. The authors have studied system identification techniques for modeling micro-cantilevers when geometry is unknown, though structural modeling was still based on several lumped-parameter assumptions and thus covered at most two vibration modes [42]. There are other methods like modal coordinate analysis for flexible systems [32][39], MEMS switches [9][15-16][20], atomic force microscopy [13] and micro-resonator [43]. As introduced in such various studies, modal coordinate analysis provided a fairly close approximation for conventional flexible systems.

A common feature of these models is that impact influence is estimated using only states associated with the physical point where contact occurs. However, small micro-devices may be affected throughout the whole structure by external impact over a very short time period and it is not easy to measure the dynamic responses accurately due to their small size and limitations in measuring instruments. Furthermore, it is even harder to estimate responses to impact disturbance for micro-systems without a stationary base, such as the walking robots in this work, since responses may appear chaotic. Thus, conventional impact models dealing with only the contact point do not provide good predictions or reconstructions of performance in the case of comparatively unconstrained, small-scale actuation structures.

In this work, we propose an alternate form for modeling contact dynamics between a foot of a walking micro-robot and the ground using an expanded coefficient of restitution matrix, a CoR matrix hereafter, that will be seen to provide a fair estimation of robot motion over various test environments without specified geometry or ground material. In addition to describing the behavior of short-duration impact events, the robots will be used to estimate the magnitude of other small-scale forces of various interactions between short-range surfaces, such as electrostatic attraction and squeeze-film damping, to better understand challenges as micro-robots become even smaller in size. The proposed modeling method is expected to be applicable to microstructures that are best modeled as continuous, modal structures with specific points of contact with their surroundings. Furthermore, the model and experimental information about foot behavior is intended to aid in developing gait patterns for further miniaturized thin-film piezoelectric micro-robots. Using experimental comparisons based on two micro-robot prototypes, the proposed modeling method will be validated and discussed.

3.2 Test Devices

The dynamic modeling of micro-robotic foot impact is tested using two prototype robots actuated by bulk lead-zirconate-titanate (PZT) ceramics; one is referred to as a quadruped bulk PZT robot (QBPZTR) and the other a hexapod bulk PZT robot (HBPZTR). "Bulk" piezoelectric material is highlighted to distinguish the robots from associated micro-robots based on piezoelectric thin-films, for whom the robots tested in this work are intended to provide information about foot-terrain interaction [5]. The current robots were designed for two different approaches to assembling comparatively small but simple walking robots. These robots have leg structures with thickness more than 100 μm and maximum robot lengths on the order of 2 cm, strong enough to endure repetitive tests on impact with various ground surfaces but also having small enough dimensions and inertia for the effects of various short-range forces to be observed.

Figure 3.1 shows the design and figure 3.2 the assembly process for each robot. The QBPZTR was assembled with two PZT-Brass-PZT (STEMINC SMBS1515T06P750) composite strips attached to a silicon piece which is mounted to an aluminum block to reduce the influence of wire tethers on robot motion. By etching the electrodes on the PZT, each strip can be operated as two separate legs. For the HBPZTR, 150 μm thick PZT ceramic blocks (Naval Type VI, cut to shape by a silicon dicing saw) were attached to a bulk micro-machined silicon structure using conductive epoxy. In this configuration, the PZT functions as actuators while most of leg structure is composed of silicon. Both robots have additional "feet" either bulk micro-machined or attached by adhesive beneath the tips of legs to better approximate full-fledged walking micro-robots, and also to allow for a large degree of lumped-parameter modeling of foot-interaction characteristics with reduction of structural modeling complexity. Figure 3.3 shows examples of completed robot prototypes.

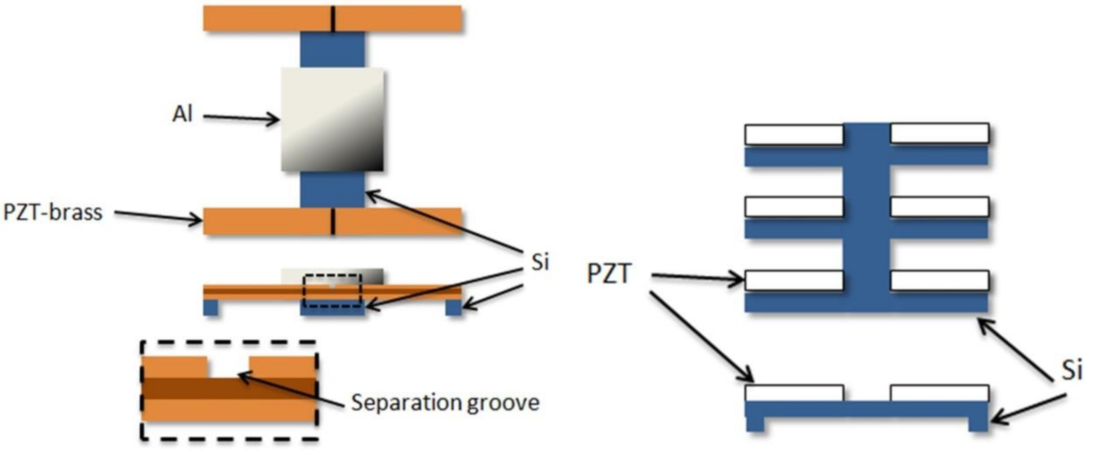

(a) (b)

Figure 3.1 Micro-robot prototypes based on bulk PZT ceramics: (a) the quadruped bulk PZT robot (QBPZTR) is based on assembly of off-the-shelf PZT bimorphs to machined silicon and aluminum components, (b) the hexapod bulk PZT robot (HBPZTR) is based on direct assembly of small PZT ceramic strips to a micro-machined silicon chassis and leg structure.

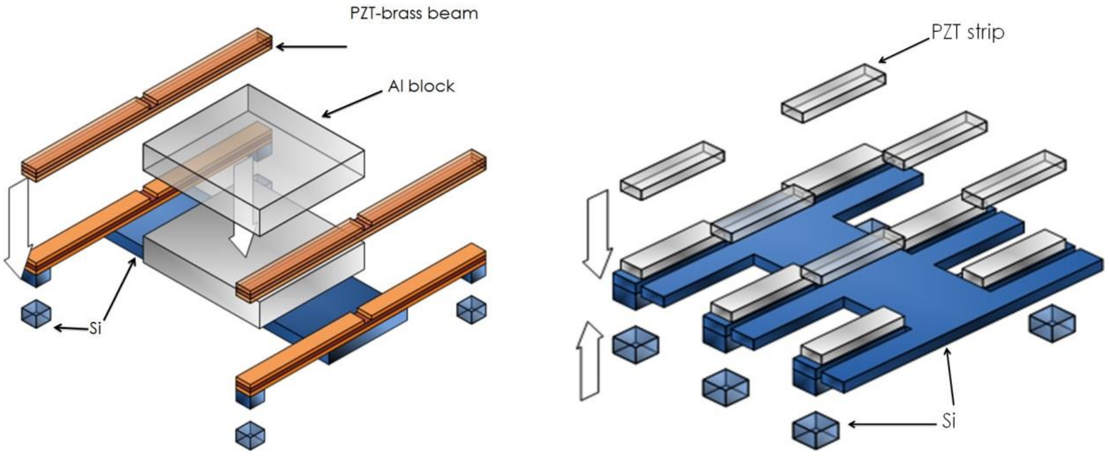

(a) (b)

Figure 3.2 Assembly process of (a) QBPZTR, (b) HBPZTR shows locations where PZT ceramic blocks and silicon feet are adhered to silicon structure (with additional Al body mass in case of QBPZTR)

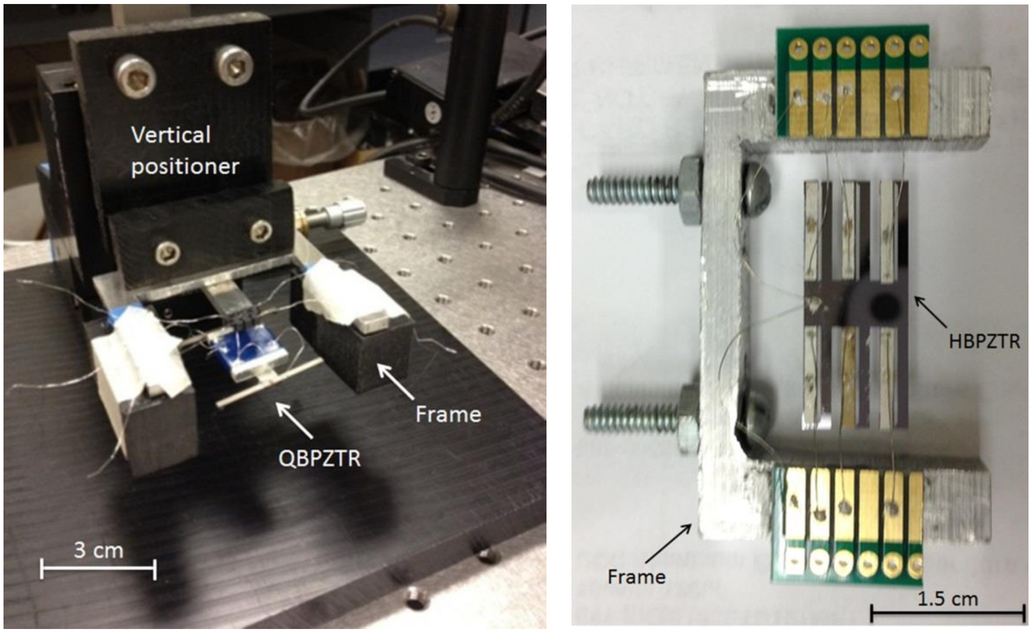

(a) (b)

Figure 3.3 Photos with dimensions of (a) QBPZTR tethered in test apparatus, (b) HBPZTR after PZT ceramic assembly

Only vertical motion is focused on in this work. This is in part due to limitations on experimental equipment, but also because we see the first task in understanding micro-robot foot-terrain interaction to be analyzing the bouncing, firm contact, and/or sticking of micro-robot feet during vertical motion. Based on this assumption, the QBPZTR was designed from the beginning to have vertical motion only, as shown in figure 3.4a. In quasi-static operation, when voltage is applied, by the difference in extended lengths between the PZT layers and brass layer at the middle, the tip of the leg bends up and down, creating the foot motion. On the other hand, the HBPZTR is originally designed to have both vertical and lateral motions at the tip of the leg. However, in this paper, the shin part below the thigh for each leg is amputated and an additional "foot" is attached to the bottom of the thigh tip to consider vertical actuation only.

3.3 Robot Dynamic Model

3.3.1 Structure & PZT forcing model

As shown in figures 3.1-3.4, after assembly, the devices tested in this work have a generally compliant solid structure, which implies that dynamic motion is best described using modal vibration models for continuous structures. While static displacements of each individual leg are largely independent, structural deformation in response to time-varying inputs is distributed over the entire mechanical structure. In addition, due to small size and the tens-of-microns gap from the ground, dynamics are largely affected by impact with the ground and various micro-scale forces like squeeze-film damping. This combination of factors differs from most macro-scale contact modeling, but has been difficult to capture in previous models of micro-scale contact, especially for systems such as walking micro-robots where fixed contact geometry is not present.

To begin contact modeling, a modal identification method was selected to derive equations of motion for describing the system response to various excitations. The system dynamics for both tested robots can be expressed in a lumped-parameter fashion in modal coordinates as follows,

$$\ddot{\mathbf{q}} + \mathbf{\Lambda_C}\dot{\mathbf{q}} + \mathbf{\Lambda_K}\mathbf{q} = \mathbf{B_d}\mathbf{u_d} + \mathbf{B_w}\mathbf{u_w} \tag{3.1}$$

where $\mathbf{q}$ indicates a state vector representing modal contributions in displacement dimension. $\mathbf{\Lambda_C}$ and $\mathbf{\Lambda_K}$ stand for diagonal matrices of modal damping terms and squared natural frequencies, respectively. The two terms on the right side of (3.1) indicate a driving force term and a disturbance input terms where $\mathbf{u_d}$ is a vector of voltage inputs to legs and $\mathbf{u_w}$ is a vector of disturbances from feet. $\mathbf{B_d}$ and $\mathbf{B_w}$ represent the input matrices for driving forces and disturbance forces, respectively.

Modal dynamics may be described in terms of physical coordinates by applying a transformation matrix, $\mathbf{\Phi}$,

$$\mathbf{q} = \mathbf{\Phi}^{-1}\mathbf{x} \tag{3.2}$$

where **x** represents a position vector in physical coordinates. Then, the equations of motion in physical coordinates can be described as follows,

$$\mathbf{M\ddot{x}} + \mathbf{C\dot{x}} + \mathbf{Kx} = \mathbf{F_d} + \mathbf{F_w} \tag{3.3}$$

where **M**, **C**, and **K** represent equivalent mass, damping and stiffness matrices. For the QBPZTR, **x** is a 5-by-1 vector representing vertical positions of 4 feet and the center of body. For the HBPZTR, **x** represents a 6-by-1 vector of 6 feet position. $\mathbf{F_d}$ and $\mathbf{F_w}$ are the equivalent distributed driving force vector and the equivalent disturbance input vector, respectively. $\mathbf{F_w}$, in turn, can be then expressed as a summation of forces experienced during contact, $\mathbf{F_I}$ and small-scale non-contact forces, $\mathbf{F_{SS}}$,

$$\mathbf{F_w} = \mathbf{F_I} + \sum \mathbf{F_{ss}} \tag{3.4}$$

The system orders are intentionally limited to be relatively small (capturing 5 and 6 vibration modes, respectively) considering the continuous structure, despite less accuracy of the modal model, for three reasons. First, measurement of motion at many more locations is difficult since motions of the system structures are mostly small, with magnitudes of 10 ~ 20 μm. Second, it reduces the complexity of quantifying discrete impact influences on system dynamics and detecting and quantifying the existence of other nonlinear small-scale forces, given the large number of possible sources of disturbance. Third, considering unknown and changeable ground conditions, further detail provided by a higher-order structural model would be smaller than the uncertainty produced by ground interactions.

These models have been derived assuming linear structural dynamics with linear piezoelectric forcing inputs, despite the fact that there is known hysteresis in the bending actuation of piezoelectric composite beams. This assumption is also made to keep the model simple, as the influence of hysteresis in tested bulk PZT beam actuation is found to be comparatively small over the low voltage ranges used in the ensuing experiments which are below 10 V with maximum error less than 5% at 0 V, as shown in figure 3.4. Furthermore, in the majority of experiments, square waves have been used for input voltage signals, to anticipate simple switching inputs available to low-power micro-robots, and this produces a case where knowledge of only a single piezoelectric gain is required.

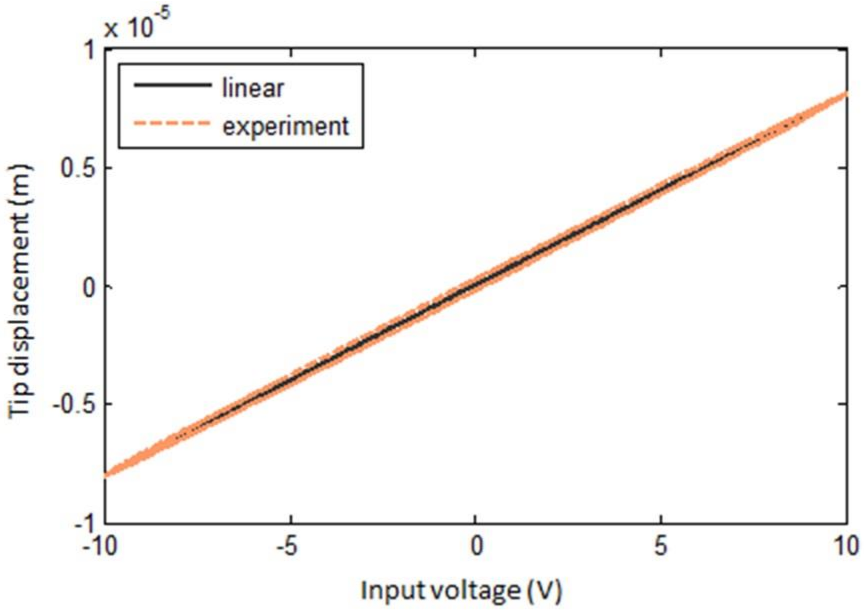

Figure 3.4 Displacement versus voltage with sinusoid input signal

3.3.2 Impact model

Analytical method

As previously mentioned, existing impact models are generally not directly effective for modeling continuous micro-robotic structures without a fixed base. Hence, a modeling approach for this situation has been developed and described below. Although the commonly used concept of a coefficient of restitution (CoR) is central to this approach, not only the velocity of a contact point but also those of the remaining physical points in the model are modified at the instant of impact, with a CoR determining motion immediately following impact. This approach to impact modeling is based on the following assumptions:

Assumption 1: The coefficient of restitution at contact point is constant over time, for given foot and terrain materials. This implies a conventional CoR relationship at the impact point,

$$\dot{x}^{+} = -\alpha \dot{x}^{-}$$

where α *is a constant representing a coefficient of restitution.*

Assumption 2: Structural motion right after the impact is determined by the dominant mode shape associated with the location and direction of the impact.

Assumption 2 is based on the knowledge that response of a continuous structure to an input is determined by the superpositions of mode shapes with the position and direction of an applied force. This assumption is considered valid in this work since it is discovered during the frequency sweeping for both tested robots that major vibration modes are well separated in frequency and that deflection of the tip of each leg is most strongly associated with a single vibration mode (though the same mode may not be dominant for each leg).

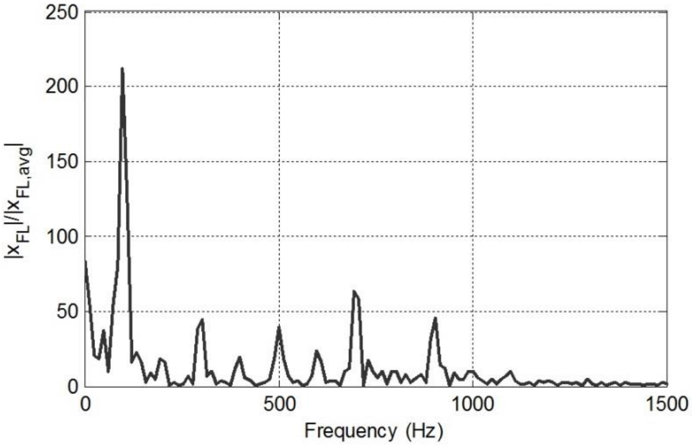

Figure 3.5 Single-sided amplitude spectrum relative to average value for fore-left leg of QBPZTR where X_{FL} and $X_{FL,avg}$ are the displacement vector of the fore-left leg and its average amplitude, respectively.

The most prominent vibration modes, those incorporated in the modal models, were those modes with resonant frequencies below 1.5 kHz and displacement magnitude 25 times larger than average in frequency spectrum of the time-domain response of leg operated in-air with 10 V white-noise voltage input, as shown in figure 3.5. Hence, only a single mode shape is used to derive the CoR matrix for a given foot of each tested robot.

In this section, we derive the CoR matrix defining impact motion based on the above assumptions, while in section 4 we will show that this contact model describes the actual behavior well. Let $\mathbf{J_I}$ be an impact impulse over contact duration t^- to t^+, or

$$\mathbf{J_I} = \int_{t^-}^{t^+} \mathbf{F_I} dt \tag{3.5}$$

Using Φ, modal transformation matrix, the impact impulse in modal coordinates can be obtained,

$$\mathbf{j_I} = \Phi^{-1}\mathbf{J_I} = \int_{t^-}^{t^+} \Phi^{-1}\mathbf{F_I} dt = \int_{t^-}^{t^+} \mathbf{f_I} dt \tag{3.6}$$

For a model consisting of *m* modes, the impact impulse in modal coordinates can be expressed as individual elements,

$$\mathbf{j_I} = \begin{bmatrix} j_{I,1} & j_{I,2} & \cdots & j_{I,m} \end{bmatrix}^T \tag{3.7}$$

Let inertial contribution to motion by each mode be represented by a set of parameters, $\eta_1, \eta_2, \ldots, \eta_i, \ldots, \eta_m$, then modal momentum change during impact can be expressed as follows,

$$\dot{\mathbf{q}}^+ - \dot{\mathbf{q}}^- = \begin{bmatrix} \eta_1 j_{I,1} & \eta_2 j_{I,2} & \cdots & \eta_m j_{I,m} \end{bmatrix}^T \tag{3.8}$$

Based on *Assumption 2*, let the k^{th} mode be dominant and govern structural motion right after the impact then,

$$\dot{\mathbf{q}}^+ - \dot{\mathbf{q}}^- \simeq \begin{bmatrix} 0 & 0 & \ldots & 0 & \dot{q}_k^+ - \dot{q}_k^- & 0 & \ldots & 0 \end{bmatrix}^T = \begin{bmatrix} 0 & 0 & \ldots & 0 & \eta_k j_{I,k} & 0 & \ldots & 0 \end{bmatrix}^T \tag{3.9}$$

This can be transformed back to the physical coordinates,

$$\dot{\mathbf{x}}^{+} - \dot{\mathbf{x}}^{-} = \Phi\left(\dot{\mathbf{q}}^{+} - \dot{\mathbf{q}}^{-}\right) \simeq \Phi\begin{bmatrix} 0 & 0 & \ldots & 0 & \dot{q}_k^{+} - \dot{q}_k^{-} & 0 & \ldots & 0 \end{bmatrix}^T = \phi_k \eta_k j_{I,k} \tag{3.10}$$

where, ϕ_i is i^{th} column vector in the transformation matrix, Φ,

$$\Phi = \left[\phi_1 \;\; \phi_2 \;\; \cdots \;\; \phi_i \;\; \cdots \;\; \phi_m\right] \tag{3.11}$$

Equation (3.10) can be expressed as follows,

$$\dot{\mathbf{x}}^{+} - \dot{\mathbf{x}}^{-} = \phi_k \eta_k j_{I,k} = \frac{\phi_k}{\phi_{k,c}} \phi_{k,c} \eta_k j_{I,k} \tag{3.12}$$

where c indicates the index of the contact foot and $\phi_{k,c}$ is c^{th} element of the column vector ϕ_k. By *Assumption 1*, CoR at the contact foot is consistent,

$$\frac{\dot{x}_c^{+}}{\dot{x}_c^{-}} \simeq \alpha \tag{3.13}$$

Here, α represents CoR at the contact foot. The above can be also written as follows,

$$\dot{x}_c^{+} - \dot{x}_c^{-} = \left(\alpha - 1\right)\dot{x}_c^{-} \tag{3.14}$$

in the c^{th} row from (3.10), substitute (3.14) then,

$$\phi_{k,c} \eta_k j_{I,k} = \left(\alpha - 1\right)\dot{x}_c^{-} \tag{3.15}$$

If (3.15) is substituted into (3.12), the following can be obtained,

$$\dot{\mathbf{x}}^{+} - \dot{\mathbf{x}}^{-} = \frac{\phi_k}{\phi_{k,c}}\left(\alpha - 1\right)\dot{x}_c^{-} \tag{3.16}$$

Let

$$\beta_c = \frac{\phi_k}{\phi_{k,c}}\left(\alpha - 1\right) \tag{3.17}$$

Substitute equation (3.17) into equation (3.16), the change in physical coordinate velocity after impact can be written as a function of contact point velocity at impact,

$$\dot{\mathbf{x}}^{+} - \dot{\mathbf{x}}^{-} = \beta_c \dot{x}_c^{-} \tag{3.18}$$

Instead of using the above form, a matrix form of CoR can be obtained which is easier to incorporate into numerical simulation models. From (3.18),

$$\dot{\mathbf{x}}^{+} - \dot{\mathbf{x}}^{-} = \frac{\boldsymbol{\phi}_k}{\phi_{k,c}}\left(\alpha - 1\right)\dot{x}_c^{-} = \begin{bmatrix} \phi_{k,1} / \phi_{k,c} \\ \phi_{k,2} / \phi_{k,c} \\ \vdots \\ \phi_{k,c} / \phi_{k,c} \\ \vdots \\ \phi_{k,m} / \phi_{k,c} \end{bmatrix} \left(\alpha - 1\right)\dot{x}_c^{-} \tag{3.19}$$

Let *c* = 1 then,

$$\dot{\mathbf{x}}^{+} = \begin{bmatrix} \alpha & 0 \\ \dfrac{\left(\alpha - 1\right)}{\phi_{k,c}} \begin{bmatrix} \phi_{k,2} \\ \phi_{k,3} \\ \vdots \\ \phi_{k,m} \end{bmatrix} & \mathbf{I}_{5x5} \end{bmatrix} \dot{\mathbf{x}}^{-} \tag{3.20}$$

Let

$$\beta_{c'} = \frac{\left(\alpha - 1\right)}{\phi_{k,c}} \begin{bmatrix} \phi_{k,2} \\ \phi_{k,3} \\ \vdots \\ \phi_{k,m} \end{bmatrix} \tag{3.21}$$

Then, from (3.20),

$$\dot{\mathbf{x}}^{+} = \begin{bmatrix} \alpha & 0 \\ \beta_{c'} & \mathbf{I}_{(m-1)\mathrm{x}(m-1)} \end{bmatrix} \dot{\mathbf{x}}^{-} = \mathbf{R}_{CoR}\dot{\mathbf{x}}^{-} \tag{3.22}$$

where, $\mathbf{R}_{CoR}$ represents the CoR matrix.

For instance, figure 3.6b shows the location and direction of impact force for the HBPZTR, $\mathbf{F_I}$, during impact at the front, left leg. In this case, the 6th mode, shown in figure 3.6c, can be considered as the most dominant mode and governs the instant motion of the structure right after impact. Here, m = 6 and k = 6, then,

$$\dot{\mathbf{x}}^{+} = \begin{bmatrix} \alpha & 0 \\ \beta_{c'} & \mathbf{I}_{5x5} \end{bmatrix} \dot{\mathbf{x}}^{-} = \mathbf{R}_{CoR}\dot{\mathbf{x}}^{-} \tag{3.23}$$

where,

$$\beta_{c'} = \frac{(\alpha - 1)}{\phi_{6,1}} \begin{bmatrix} \phi_{6,2} \\ \phi_{6,3} \\ \vdots \\ \phi_{6,6} \end{bmatrix} \tag{3.24}$$

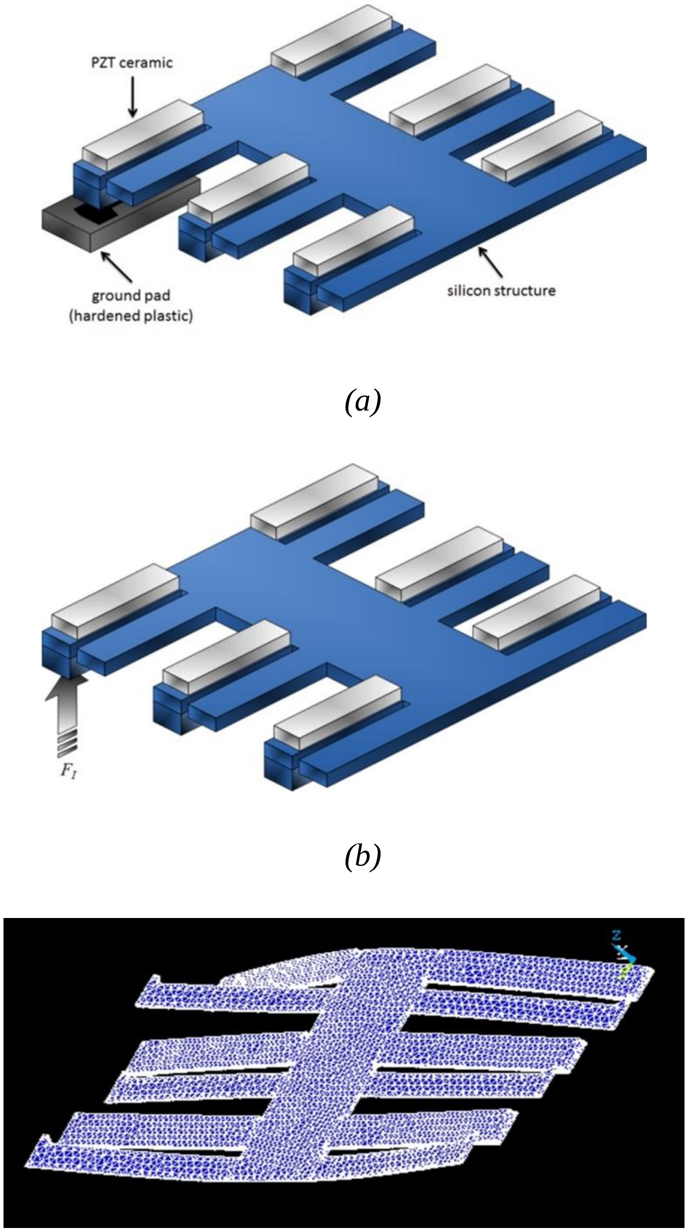

(c)

Figure 3.6 Location and direction of impact force for the HBPZTR: (a) experimental setup, single point interaction, (b) equivalent impact force, (c) 6th mode shape estimated by modal harmonic analysis with ANSYS

3.3.3 Other short range forces under consideration

Like other micro-devices with similar dimensions such as MEMS switches [7-8][15-16][18-21][42], micro-cantilevers [13], or micro-resonators [43], small-scale forces may affect the system dynamics. Based on previous works, two forces have been chosen: electrostatics and squeeze-film damping. Adhesion and friction are excluded in this current work for simplicity, by using non-sticking, smooth "ground" pads under a robot foot and focusing only on vertical behavior. The existence of these forces at a measurable level is verified by empirical observation as will be discussed later in this paper. It should be noted that lumped-parametric form has been used for mathematical expression of these forces to allow for a simple identification procedure. Thus, electrostatic force between parallel surfaces has been formulated as follows,

$$F_e = C_e \frac{V^2}{\left(x_c + g_e\right)^2} \tag{3.25}$$

where, C_e represents the coefficient of electrostatics considering the effective area and the permittivity of free space, V indicates the voltage difference, and g_e stands for the effective distance at idle between the bottom of the PZT block and the ground.

Squeeze-film damping force also has a similar generic form with a few parameters,

$$F_{sfd} = -b_{sfd} \frac{\dot{x}_c}{\left(x_c + g_d\right)^3} \tag{3.26}$$

where, b_{sfd} represents the effective coefficient of the squeeze-film damping and g_d stands for the effective neutral gap between the foot surface and the ground. The unknown coefficients in (3.25) and (3.26), C_e and b_{sfd}, are obtained experimentally by a procedure described in Section 3.4.3.

3.4 Experimental analysis

In this section, we describe the experimental setup for measuring dynamic micro-robot behavior during foot-terrain impact, and show that this behavior can be well approximated using the model described in Section 3.3.

3.4.1 Test setups

Figure 3.7 shows test setup for both robots. As shown in the figure, the tested robots are suspended in-air with bonded wires and their height can be adjusted up and down using a micro-positioner. Using this test setup, structural dynamics are first modeled by isolating the systems from any influence of the foot-ground interaction. Also, by adjusting the height of the robots, a very narrow gap with range of 10 to 30 μm between a foot and the ground pad can be achieved, which enables analysis on system responses over various gaps for characterization of the small-scale forces and impact behavior. This is important, because the small-scale forces, as shown in equations (3.25)-(3.26), are functions of the gap between surfaces.

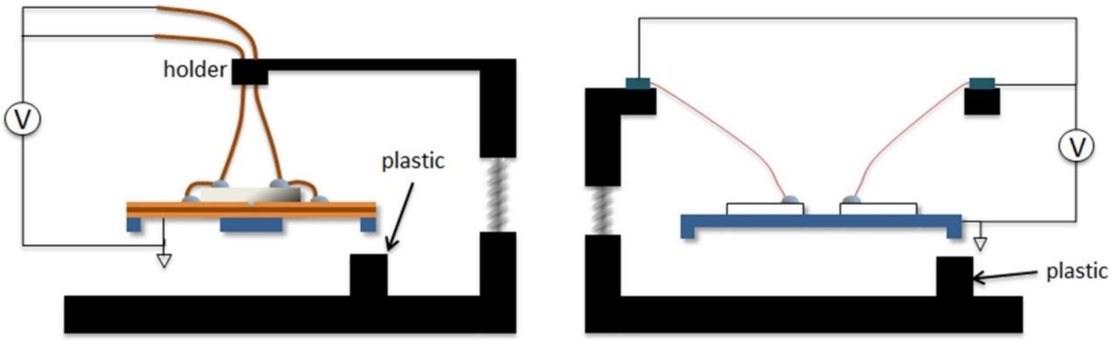

(a) (b)

Figure 3.7 Test setup for structure model: (a) QBPZTR, (b) HBPZTR

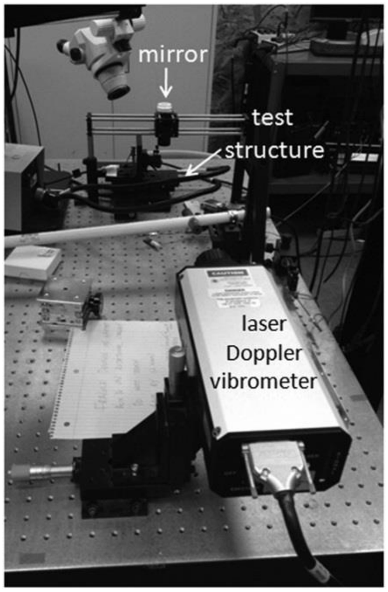

Figure 3.8 Photograph of the laser Doppler vibrometer setup

While suspended in-air, motion of the robots has been measured using interferometry instrumentation, a laser Doppler vibrometer (Polytek PSV-400) shown in figure 3.8. Without influence of disturbances from the ground, modeling of structural dynamics could be conducted to obtain equation (3.1) using modal analysis with measured data. In addition, further experimental data and simulation results with various periodic voltage inputs have been compared to validate the model and to improve its accuracy. Figures 3.9 and 3.10 show a sample comparison between experimental data and simulation results in response to a square wave input where there is no interaction between a foot and the ground due to a foot-terrain gap distance greater than 3 cm. The structural model derived for each prototype robot is shown in appendix. It should be noted that, in each of the prototype robots, one or two modes are associated with vibration of the robot body against the stiffness of the wires tethered to a power supply, rather than structural vibration of the robot itself and, therefore, these modes were filtered out from the experimental data for comparison with the data acquired by simulating the model.

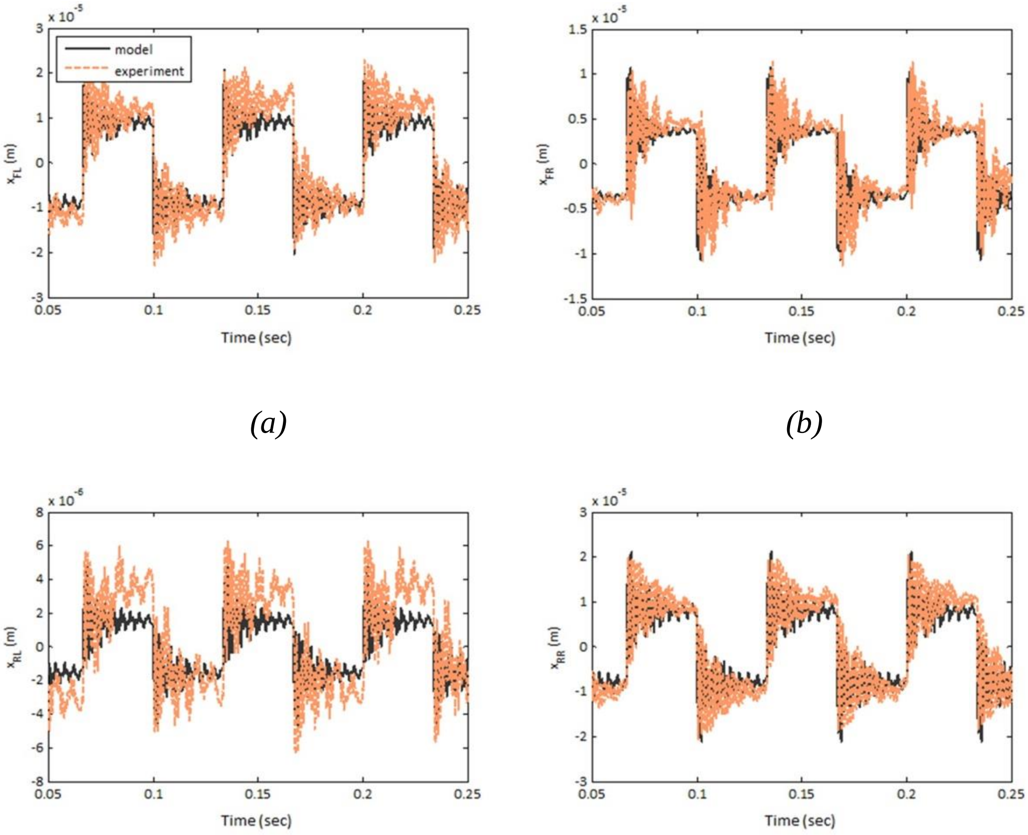

(a) *(b)*

(c) *(d)*

Figure 3.9 Response comparisons between model and experimental data (QBPZTR) for all feet with an excitation of 8V/15Hz/square-wave input to the fore-left leg: (a) fore-left leg, (b) fore-right leg, (c) hind-left leg, (d) hind-right leg

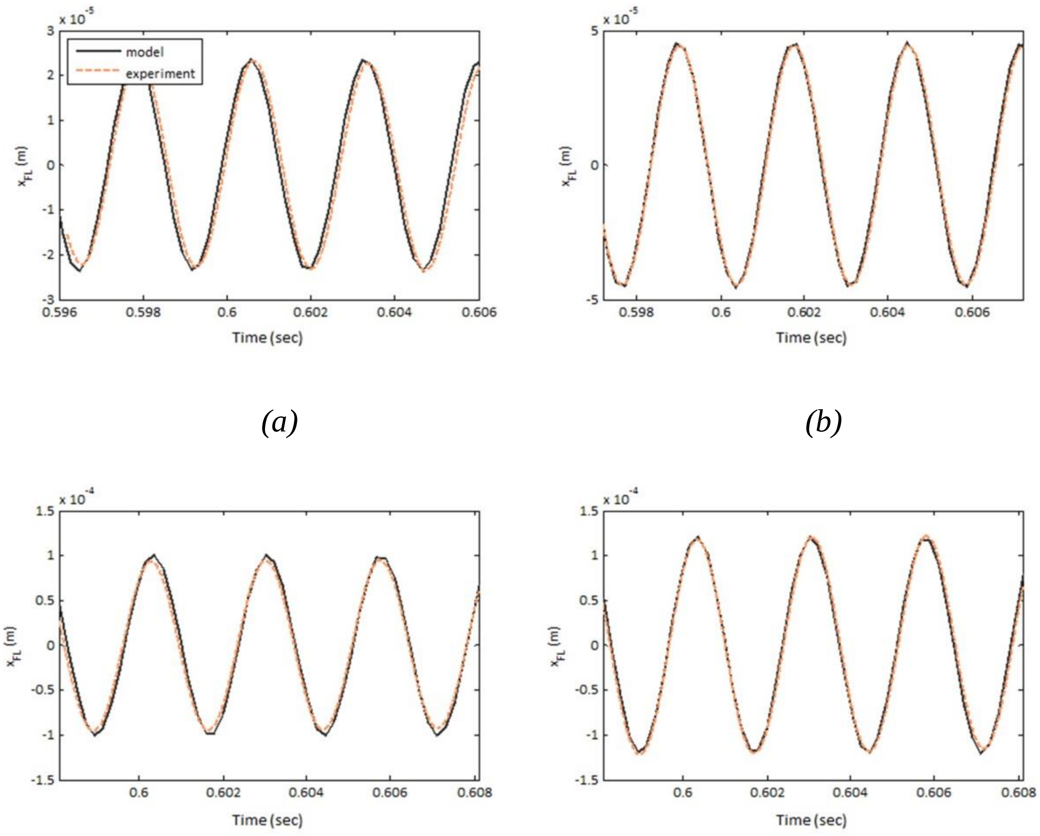

(a) *(b)*

(c) *(d)*

Figure 3.10 Response comparisons between model and experimental data (HBPZTR) for actuated foot with different voltages (a) 15V input, (b) 20V input, (c) 25V input, (d) 30V input

3.4.2 Impact model validation

System responses to impact disturbance

As shown in figure 3.11, system response to impact disturbance can be isolated (perfectly in theory for a fully-known, entirely linear system, or approximately for the actual experimental systems) by synchronizing and subtracting two different sets of the experimental data with the same voltage inputs: one set with the distance about 10 ~ 20μm between a foot and the ground where there are contacts between them and the other with farther than 3 cm where no contact occurs. In mathematical expressions, this process can be simply shown as follows,

$$\bar{\mathbf{x}} = \tilde{\mathbf{x}}_{close} - \tilde{\mathbf{x}}_{in-air} \tag{3.27}$$

where, $\bar{\mathbf{x}}$ is the processed data of system response to disturbance at feet while $\tilde{\mathbf{x}}_{close}$ indicates the measured data without existence of contact and $\tilde{\mathbf{x}}_{in-air}$ with contact. Thus,

$$\mathbf{M}\ddot{\tilde{\mathbf{x}}}_{in-air} + \mathbf{C}\dot{\tilde{\mathbf{x}}}_{in-air} + \mathbf{K}\tilde{\mathbf{x}}_{in-air} = \hat{\mathbf{F}}_{\mathbf{d}} \tag{3.28}$$

$$\mathbf{M}\ddot{\tilde{\mathbf{x}}}_{close} + \mathbf{C}\dot{\tilde{\mathbf{x}}}_{close} + \mathbf{K}\tilde{\mathbf{x}}_{close} = \hat{\mathbf{F}}_{\mathbf{d}} + \hat{\mathbf{F}}_{\mathbf{I}} + \sum \hat{\mathbf{F}}_{\mathbf{SS}} \tag{3.29}$$

For the QBPZTR, influence of the small-scale contact forces is much smaller than for HBPZTR and it could be assumed that the last term, $\sum \hat{\mathbf{F}}_{\mathbf{SS}}$, in equation (3.29) is negligible compared to impact force $\hat{\mathbf{F}}_{\mathbf{I}}$ .This is because the robot has an aluminum block at the center heavier than the rest of the robot system, Si framework and bulk PZT ceramics. This processed experimental data can be then used for further analysis of impact influence on the system.

For the HBPZTR, small-scale forces were quantified and included into the model using experimental measurements with small gaps but no contact analyzing impact behavior since their effect on the system dynamics is significant; this will be discussed in the following section. Then, the same procedure has been used with equation (3.29) for impact disturbance estimation assuming that the small-scale forces can be approximated well.

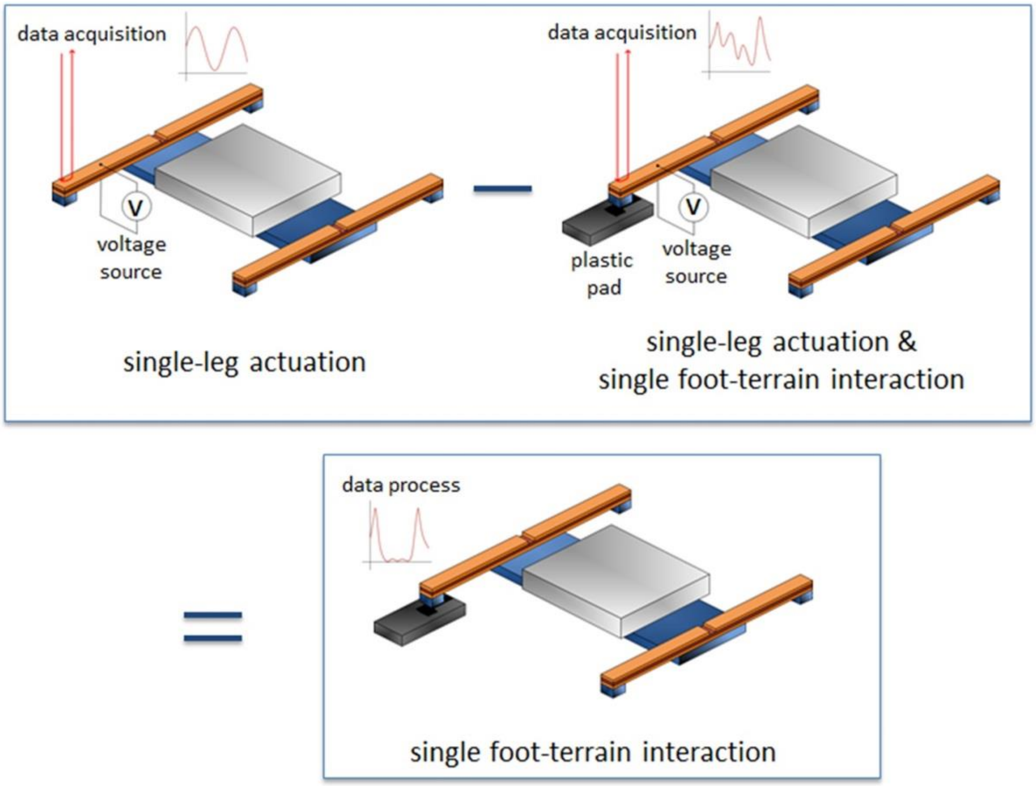

Figure 3.11 Analysis scenario; subtracting in-air dataset and contact experimental dataset (QBPZTR)

Empirical validation of impact model using numerical analysis on the processed data

The impact model was derived based on the two assumptions. With analysis on the processed experimental data introduced in the previous section, the proposed impact model can be verified by experimental validation of the degree to which these assumptions hold true. The 1st assumption can be simply validated by observing various experimental data. Figure 3.12 shows the computed CoR over various experimental data of the tested robots, where estimated CoR at each impact, $\tilde{\alpha}$, is computed,

$$\hat{\alpha} = \frac{\dot{\tilde{x}}_c^+}{\dot{\tilde{x}}_c^-} \tag{3.30}$$

where, $\dot{x}_c^-$ and $\dot{x}_c^+$ are the measured velocities of the foot right before and after impact with the ground.

The periodic voltage input signals used here are shown in table 3.1. As can be seen, while the experimental value for a is not perfectly constant, it varies over a relatively narrow range, of -0.51±0.11 for the HBPZTR on a Si substrate and -0.49±0.10 for QBPZTR on a hardened plastic substrate.

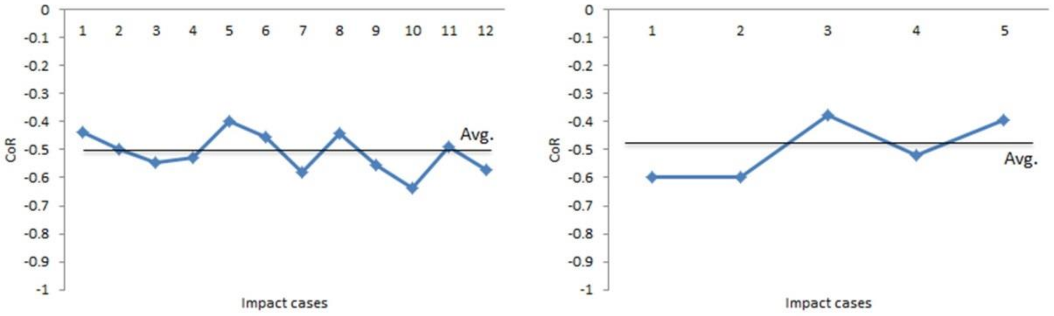

(a) *(b)*

Figure 3.12 Computed CoR over various experimental data (a) HBPZTR, (b) QBPZTR

Table 3.1 Tested periodic voltage input signals.

	QBPZTR	HBPZTR
Waveform	sine / square	sine / square
Frequency range (Hz)	15 ~ 1,000	20 ~ 900
Voltage range (V)	2 ~ 10	3 ~ 30

It should be sufficient to validate the 2nd assumption if numerical analysis on the processed experimental data provides that the instant motion is related mostly to the dominant mode shape. Since the proposed impact model treats velocity change at the instant of impact, the following quantity, a ratio of velocity change to contact foot velocity right before impact, can be considered,

$$\beta_{\dot{\mathrm{x}}} = \frac{\dot{\bar{\mathbf{x}}}^{+} - \dot{\bar{\mathbf{x}}}^{-}}{\tilde{x}_{close,c}^{-}} \tag{3.31}$$

As figure 3.13a shows, for HBPZTR, this quantity is very consistent over various experimental data using voltage inputs in table 3.1, where the 1st element represents the contact foot coordinate. This quantity can be then normalized with the element of the contact foot,

$$\beta_{\dot{x}/\mathrm{c}} = \frac{\beta_{\dot{x}}}{\beta_{\dot{x},\mathrm{c}}} \tag{3.32}$$

Another approach can be also considered. Instead of using velocity quantities, it is possible to estimate external force numerically using experimental data. Since experimental data is obtained using vibrometer, the raw data is a set of velocities. Hence, accelerations and positions can be also estimated using numerical computations as follows,

$$\ddot{\bar{\mathbf{x}}}(i) \simeq \frac{\dot{\bar{\mathbf{x}}}(i+1) - \dot{\bar{\mathbf{x}}}(i)}{t_s} \tag{3.33}$$

$$\bar{\mathbf{x}}(i+1) \simeq \bar{\mathbf{x}}(i) + \dot{\bar{\mathbf{x}}}(i) \cdot t_s \tag{3.34}$$

where, t_s is a sampling time of the measured data. Then, the external impact force estimation can be estimated,

$$\hat{\mathbf{F}}_{\mathbf{e}}(i) \simeq \mathbf{M}\ddot{\bar{\mathbf{x}}}(i) + \mathbf{C}\dot{\bar{\mathbf{x}}}(i) + \mathbf{K}\bar{\mathbf{x}}(i) \tag{3.35}$$

if impact occurs at $i=k$, then the following quantity can be considered as the estimated impact force.

$$\hat{\mathbf{F}}_{\mathbf{I}}(k) \simeq \hat{\mathbf{F}}_{\mathbf{e}}(k+1) - \hat{\mathbf{F}}_{\mathbf{e}}(k) \tag{3.36}$$

Likewise, this quantity can be normalized with the element of the contact foot.

$$\hat{\mathbf{F}}_{\mathbf{I}/c} = \frac{\hat{\mathbf{F}}_{\mathbf{I}}}{\hat{f}_{\mathbf{I},c}} \tag{3.37}$$

For the HBPZTR case, as shown in figure 3.13b and 3.13c, there exists a very consistent trend in the quantities presented in equation (3.32) and (3.37).

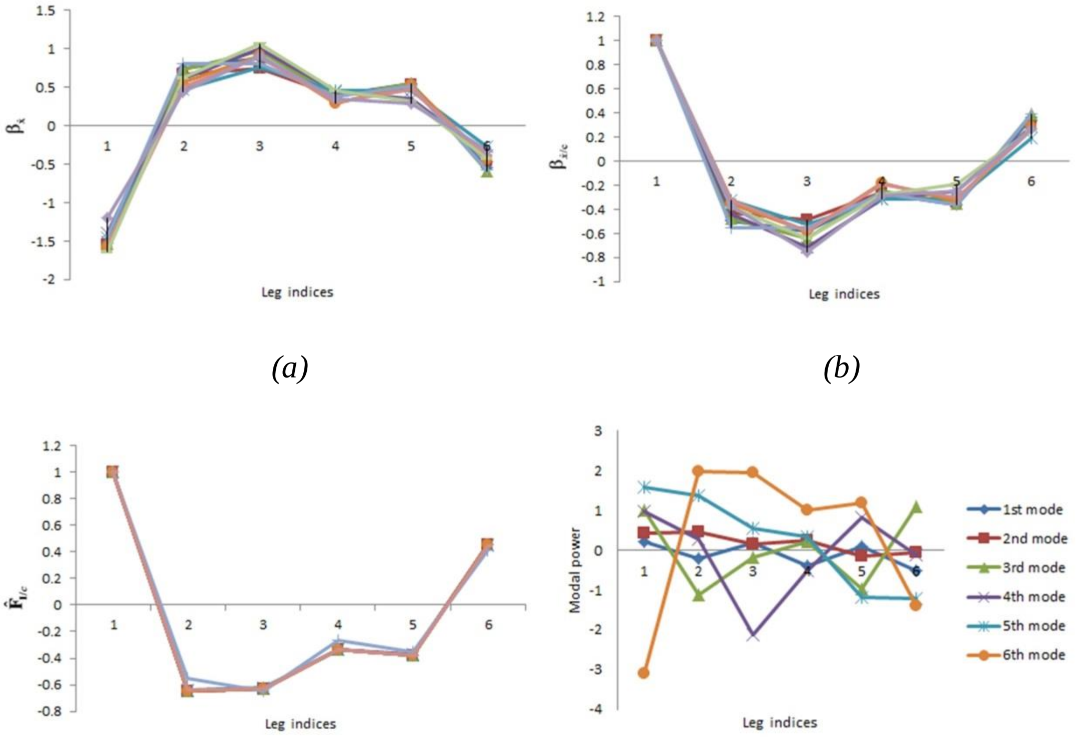

(a) *(b)*

(c) *(d)*

Figure 3.13 Impact trends in various experimental quantities for HBPZTR (a) $\beta_{\dot{x}}$, a ratio of velocity change to contact foot velocity right before impact, (b) $\beta_{\dot{x}/c}$, normalized $\beta_{\dot{x}}$ with the element of the contact foot, (c) $\hat{\mathbf{F}}_{\mathbf{I}/c}$, normalized impact force with the element of the contact foot, (d) comparison of modal contributions

As previously proposed by the 2nd assumption, this trend is very similar to one of the structural mode shapes. The comparison between the derived quantities and the 6th mode shape of the HBPZTR is illustrated in figure 3.14. As shown, the agreement presented in the figure implies that the instant impact behavior might be approximated with even single mode shape. This provides validation for the 2nd assumption as well as the proposed impact model with derivation of the CoR matrix.

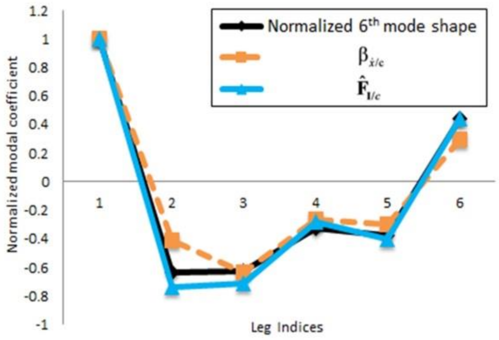

Figure 3.14 Comparison between numerical quantities and a dominant mode shape for HBPZTR

3.4.3 Verification of the existence and quantification of small-scale forces for HBPZTR

For the HBPZTR, small-scale forces are quantified and included into the model since the influences of such forces on this much less massive system are more prominent than on the QBPZTR. Intermediate distances of about 20 to 40 µm between a foot surface and the ground can be obtained by adjusting the height of the robots using vertical micro-positioner shown in figure 3.3a. At this particular range of gap, a foot does not successfully make a contact with the ground but small-scale forces affect the system dynamics in a measureable way. Figure 3.15 shows comparison of experimental data sets for the HBPZTR over various voltage inputs and inter-surface gaps; 3 cm and 25 µm. As illustrated in the figure, comparing the two cases using the same voltage input but different gaps, it can be seen that the magnitude of the foot motion decreases as the distance between a foot and the ground is small.

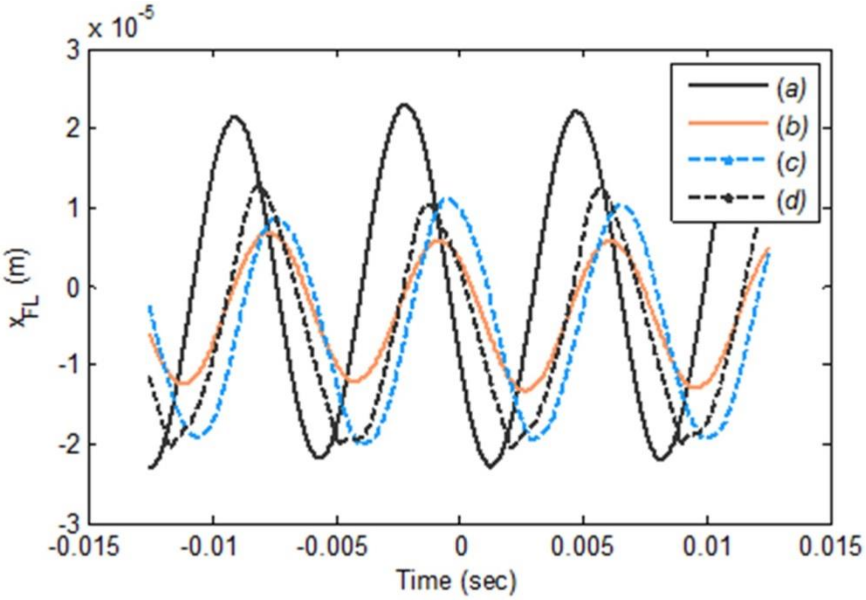

Figure 3.15 Experimental data for vertical foot velocity with silicon ground pad, varying gap from ground pad, d and voltage input, Vin. (a) d > 3 cm, Vin = 10V (b) d = 25 μm, Vin = 3V (c) d = 25 μm, Vin = 6V (d) d = 25 μm, Vin = 10V

Testing with various ground pads, shown in figure 3.16, implied that at least two small forces significantly affect the foot motion, assumed to be a squeeze-film damping force and an electrostatic damping force arising as shown in figure 3.16a, with squeeze-film damping localized at the robot foot and electrostatic effects distrusted over the leg as associated with the input voltage.

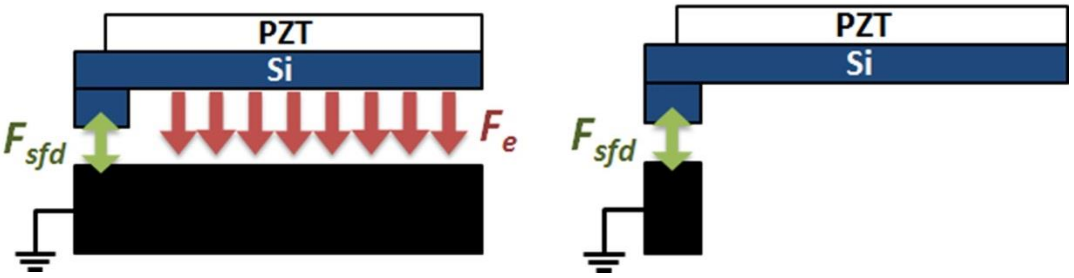

(a) (b)

Figure 3.16 Tested ground pads for HBPZTR (a) long pad, (b) short pad

To test this assumption, a second ground configuration with a short ground pad, shown in figure 3.16b was inserted and trends in motion amplitude measured experimentally as shown in figure 3.17, in an attempt to isolate the various effects. Cases shown include motion without a ground pad, motion over a short pad with a smaller and larger initial gap, and for a long ground pad at the larger initial gap. Voltage is gradually increased, though without reaching the point of contact during leg motion

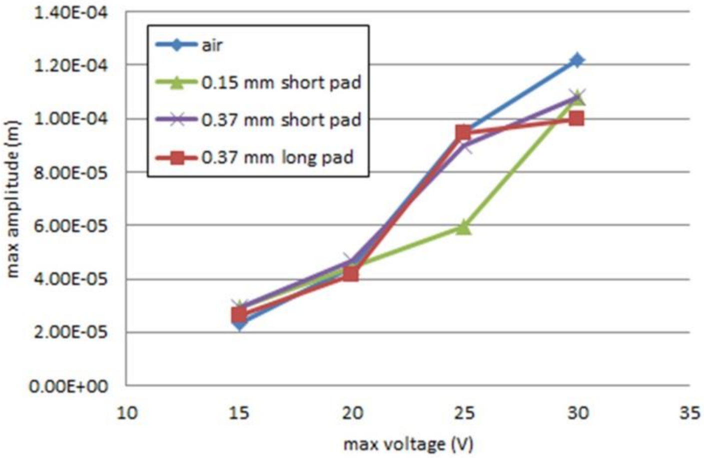

Figure 3.17 Existence of small-scale forces implied from experimental analysis on different gaps and pads

As figure 3.17 shows, in all cases as voltage increased there was an overall amplitude reduction compared to air. This is attributed to the fact that as maximum voltage input (MVI) increases, amplitude of vertical movement of the operating leg increases as well, resulting in smaller minimum gap from the ground pad during actuation which induces larger influence of small-scale forces, predominantly squeeze-film damping. Comparing the two cases using the same short ground pad but different initial gaps, there is a large difference at 25 V MVI, which indicates that squeeze-film damping has begun to significantly act in the case of the 0.15 mm initial gap. By 30 V MVI, the difference between the two cases is small since squeeze-film damping acts significantly in both cases. Comparing two cases using the same initial gap but different pads in length, the case using long pad shows slightly larger amplitude at 25 V MVI, attributed to the electrostatic force. This then returns to a comparable amplitude at 30 V MVI, which is believed to be a result of squeeze-film damping again becoming the dominant nonlinear effect without contact when the gap becomes very small between the leg and the ground.

Additional comparison between experimental data and simulation results in time-domain responses is shown in figure 3.18. Simulation studies implied that magnitude reduction is due to squeeze-film damping and sinusoidal output "tilting" to the right is mostly due to electrostatics as shown in figure 3.18. Using experimental comparison with the simulation results, each small-scale force has been quantified and added to the model using similar procedure previously suggested one of our previous works.

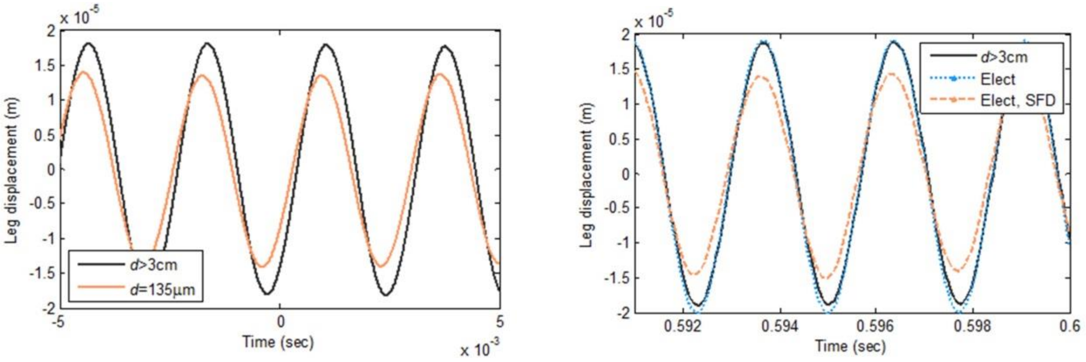

(a) *(b)*

Figure 3.18 Validation of small-scale forces between foot and ground using 10 V voltage input (a) experimental data, (b) simulation studies

3.5 Experimental Validation

The dynamic and impact models for each robot have been validated using further experimental comparisons. Figure 3.19 and 3.20 show the experimental comparisons of QBPZTR which are the response of 5 different points for the same excitation while figure 3.21 and 3.22 show those of HBPZTR comparing the response of the actuated leg using 3 different inputs. Validation is focused on the comparison in time-series responses. However, it is not easy to directly compare the simulation result and the experimental data despite using periodic voltage inputs as shown in figure 3.19 and 3.21 since the resulting impact response does not repeat over a single period, but rather over several successive periods, and there is significant random variation. However, it can be still seen in both cases that the overarching periods and amplitudes of the simulation and experimental responses are consistent and similar to each other.

Using the feature of periodic voltage inputs, the time-series responses have been mapped into circular coordinates as shown in figure 3.20 and 3.22. One circular rotation indicates one periodic cycle of the input and the distance from origin indicates physical height from the ground meaning that the origin is the ground position. This plot provides better understanding in comparison of trends and behaviors of system responses over various disturbances including impact with the ground as shown in the figure. For the QBPZTR, as shown in figure 3.20, the response amplitudes of the bouncing foot and most other feet are approximated well except the fore-right foot. The impact behavior at the bouncing foot is, especially, captured well showing similar repetitive trend in magnitude and oscillation in-air after break-off.

For the HBPZTR, experimental validation was conducted by comparing responses at the bouncing foot using three different test cases: 10 V sine input with 10 μm gap, 10 V square input with 10 μm gap, and 10 V square input with 5 μm gap. As shown in figure 3.22, the proposed impact model provides a fair approximation for the HBPZTR as well showing similar trend in bounce and oscillation in-air. Especially, figure 3.22 shows that the number of bouncing for single period varies according to test cases and it is captured by the model quite well. It implies that three oscillations per step are visible, that the relative amplitudes are consistent, and that impacts mostly occur at the same points in the cycles for the three cases. It should be noted, however, that the model fails to capture the fact that one oscillation is typically much smaller than the others in two of the cases as shown in figure 3.22a and 3.22b, and the model misses a few bounces in the third case as shown in figure 3.21c and 3.22c. Although the model estimation for each robot is not perfect, it is fairly good overall given the complexity of interaction and comparatively simple model, and the trend of impact influence is well captured as shown in these figures.

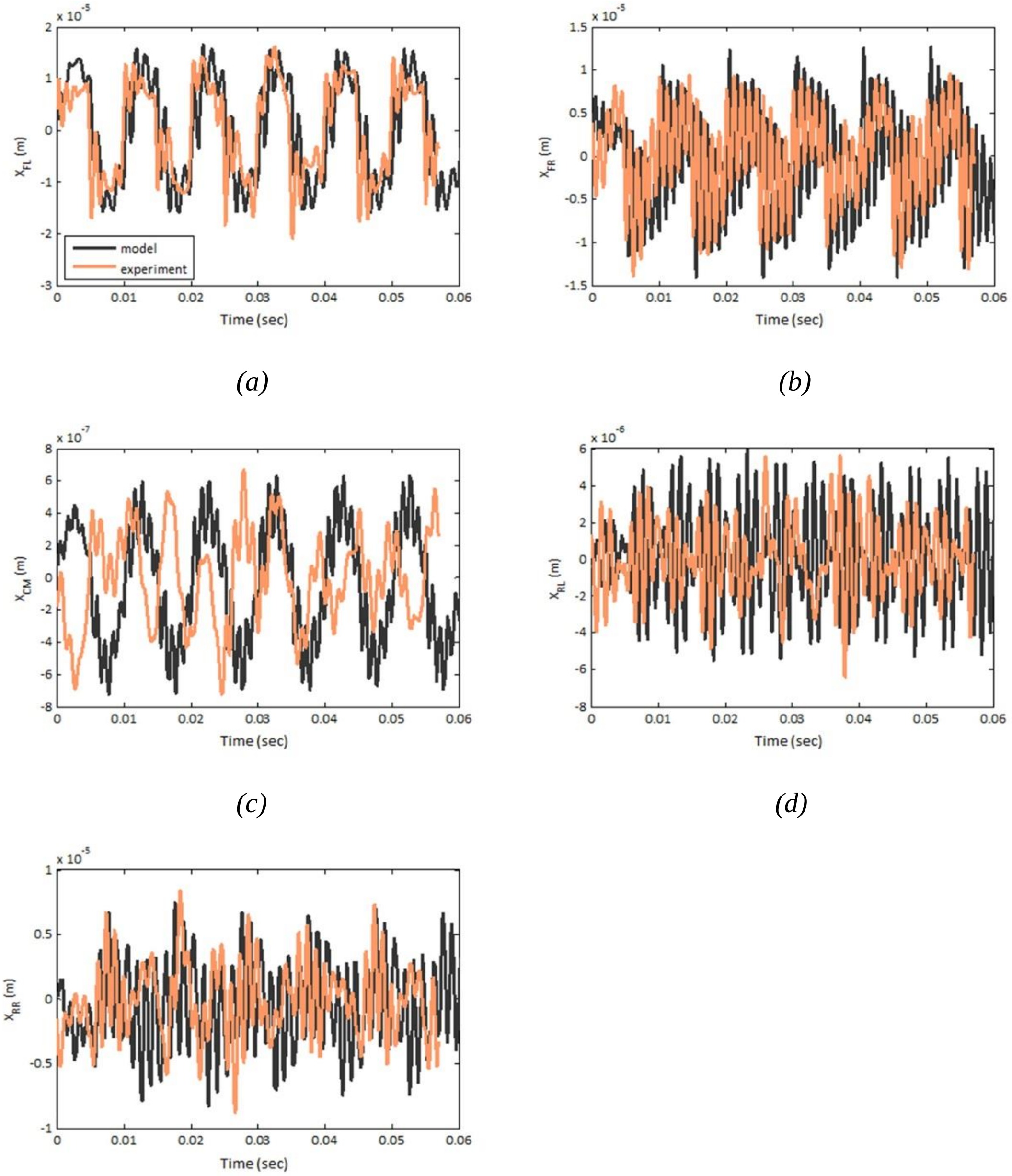

(a) *(b)* *(c)* *(d)* *(e)*

Figure 3.19 Comparison (QBPZTR) of displacements in time-domain responses (a) fore-left leg, (b) fore-right leg, (c) center of body, (d) hind-left leg, (e) hind-right leg

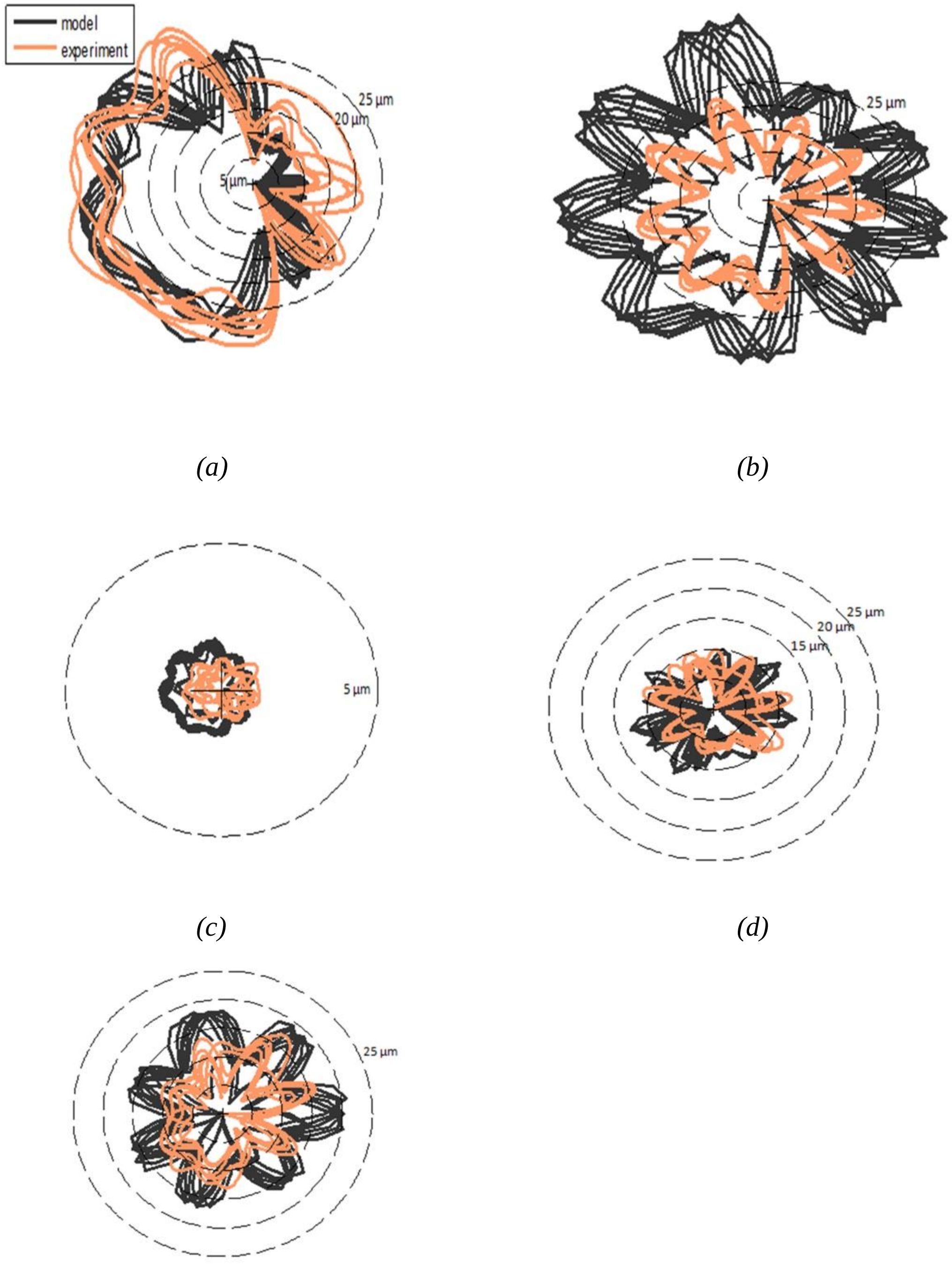

(a) *(b)*

(c) *(d)*

(e)

Figure 3.20 Time response comparison - circular plot (QBPZTR) (a) fore-left leg (bouncing leg), (b) fore-right leg, (c) center of body, (d) hind-left leg, (e) hind-right leg

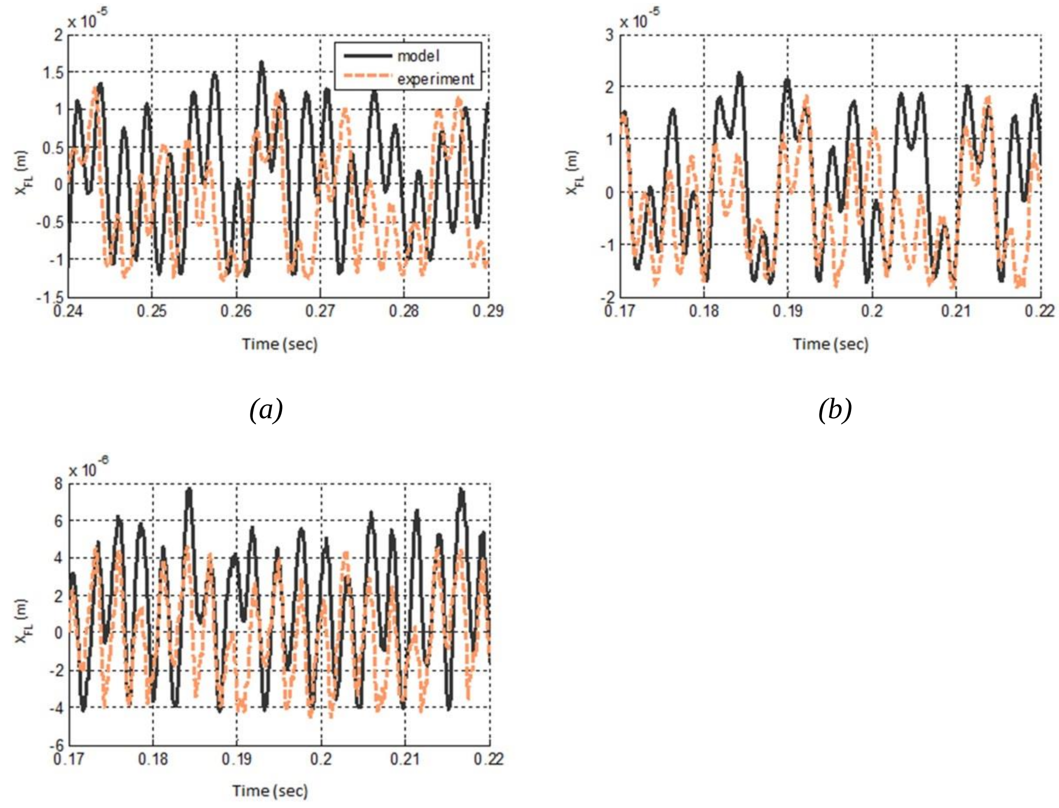

(a) *(b)*

(c)

Figure 3.21 Time response comparison (HBPZTR) using 3 different inputs (a) 10 V sine wave with 10 um gap, (b) 10 V square wave with 10 um gap, (c) 10 V square wave with 5 um gap

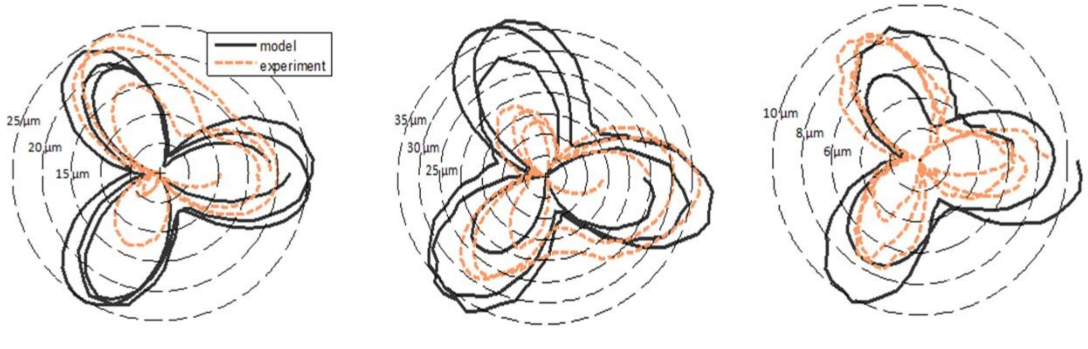

(a) *(b)* *(c)*

Figure 3.22 Time response comparison - circular plot (HBPZTR) using 3 different inputs (a) 10 V sine wave with 10 um gap, (b) 10 V square wave with 10 um gap, (c) 10 V square wave with 5 um gap

For the HBPZTR, existence of small-scale forces was validated by comparing simulation results with and without such forces and the experimental data as shown in figure 3.23. The diagrams in figure 3.23 show the relative levels of three quantified descriptions of vertical motion: average leg height, number of bounces over a fixed time period, and peak leg height. In each of the three scenarios discussed above and by each of the three criteria, simulations with small-scale forces included came much closer to matching experimental data than simulations without. This is crucial for modeling full gait motion of walking robots, since lateral leg actuation contributed to locomotion of robots is made mostly when there is contact between the leg and the ground, Full gait simulation, though, is beyond the scope of this chapter and is future work.

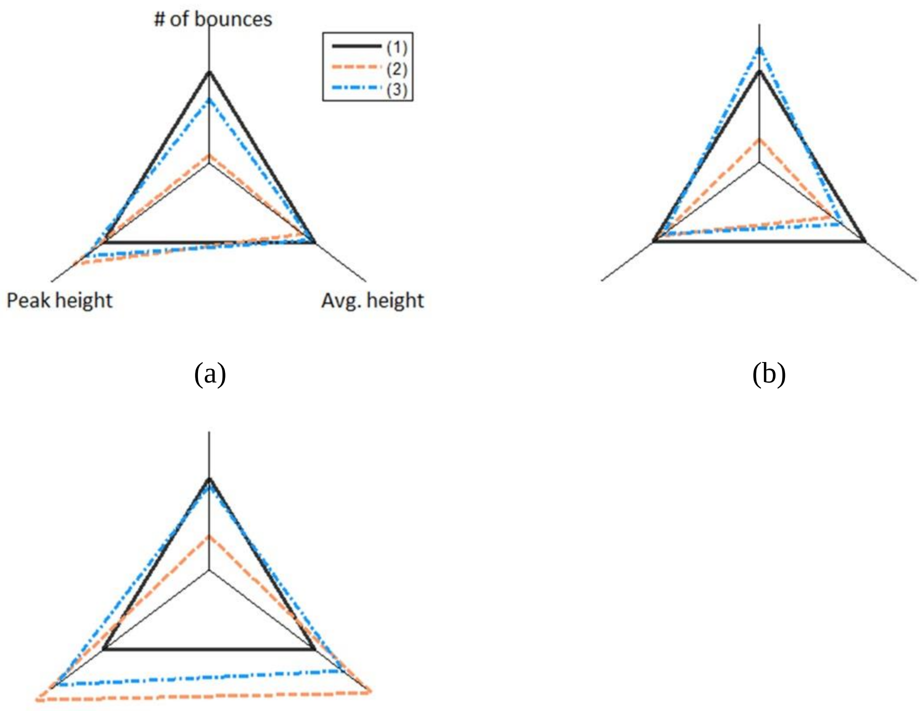

(a) (b)

(c)

Figure 3.23 Existence of small-scale forces

(a) 10 V sine wave with 10 um gap, (b) 10 V square wave with 10 um gap, (c) 10 V square wave with 5 um gap (1) experimental data (2) simulation data without small-scale forces (3) simulation data with small-scale forces

Table 3.2 Numerical comparisons between model and measured data.

	10 V sine wave input / 10 µm gap		10 V square input / 10 µm gap		10 V square input / 5 µm gap	
	experiment	model	experiment	model	experiment	model
# of bounce (per second)	260	180	160	200	220	200
Peak height (µm)	23.5	23.0	36.2	28.5	8.6	11.0
Avg. height (µm)	14.8	17.3	23.6	21.4	6.8	9.9

Table 3.3 Parameter quantification for each robots.

Quantities	HBPZTR	QBPZTR
ω_1 *(Hz)*	89.5	15.0
ω_2	134.0	86.0
ω_3	314.6	181.0
ω_4	368.5	724.0
ω_5	660.0	893.0
ω_6	2910	-
α *(on hardened plastic)*	0.498	0.49
α *(on silicon)*	0.51	-
C_e	1e-9	-
b_{sfd}	1e-12	-
System mass (g)	0. 16	2.7

CHAPTER 4

DYNAMIC MODELING AND SIMULATION STUDIES OF THIN-FILM PIEZOELECTRICALLY ACTUATED WALKING ROBOTS, MILLIPEDE PROTOTYPES

4.1 Introduction

There have been numerous dynamic models for walking robots introduced by previous researchers. For non-micro-robots, a commonly applied theoretical approach is a model associating a kinematic chain of robot links with the ground using a lumped dynamic model [38][45][46][47][48]. In many cases, such a dynamic model is simplified and the error due to the simplification is compensated by various control strategies. Along with this approach, some studies utilize a compliant ground model providing good results in contact behavior estimation [38][41][45]. Some studies neglect kinematic relationship between robot parts and the ground and use only a simplified lumped model for contact dynamics [49]. For special objectives in contact during walking, contact dynamics are sometimes associated with additional models such as adhesion [50] or hydrodynamic pressure [51].

Although the models in these studies present good estimations in experimental comparisons or provide the intended results according to their purposes, these approaches may not be available for micro-robots. The contact dynamics in micro-robot locomotion can be different due to significant influence of small-scale contact forces such as electrostatics, adhesion, or squeeze-film damping between a foot and the ground. Hence, a conventional contact model used in non-micro-robots might not provide good estimation. Furthermore, since many micro-/nano-robots have non-rigid continuous mechanical structures, the commonly used method of solving kinematics between parts is not necessarily available.

Thus, different approaches have been introduced for micro-robot walking dynamics. One example is application of biomimetic design, studying insect locomotion due to micro-robots' similarity in size. However, in existing works robot size is on the order of tens-of-millimeters, which is much larger than the thin-film micro-robots of this work [52], or explicit validation with experimental comparison is not present. Direct application of the studies of insect locomotion analysis might be another method to model the walking dynamics of the robots. However, despite novel theoretical analysis of insect locomotion [53], such studies might not be applicable since insect legs consist of parts and joints like non-micro-robot legs although they may provide helpful ideas for specific purposes in contact mechanism between a foot and the ground. (for example, a strong adhesion between an insect foot and the ground due to a fabric structure [54] can be applied to the design of the robot foot surface.)

The objective of the work in this chapter is to apply the modeling procedure based on experimental system identification to the generation of accurate walking dynamic models for the micro-robots. To accomplish this goal, established in the previous tasks were procedures for characterization of disturbance from foot-terrain interaction and modeling of structural dynamics. To achieve those respective objectives, a micro-cantilever test structure and micro-machined robots with relatively simple structures were developed and tested. In this task, the proposed modeling technique is applied to more delicate and sensitive walking robots, millipede prototypes, shown in figure 1.2b and 4.1. A millipede prototype is designed to have 30 legs in total to compensate typical weaknesses of thin-film MEMS robots such as small weight bearing capability and high possibility of leg failures due to their thin, delicate and complex structures. Despite simpler leg configuration than a hexapod prototype shown in figure 1.3, each leg system of millipede design is also capable of m-DoF motion with both vertical and in-plane actuations, although those actuators are electrically coupled.

(a)

(b)

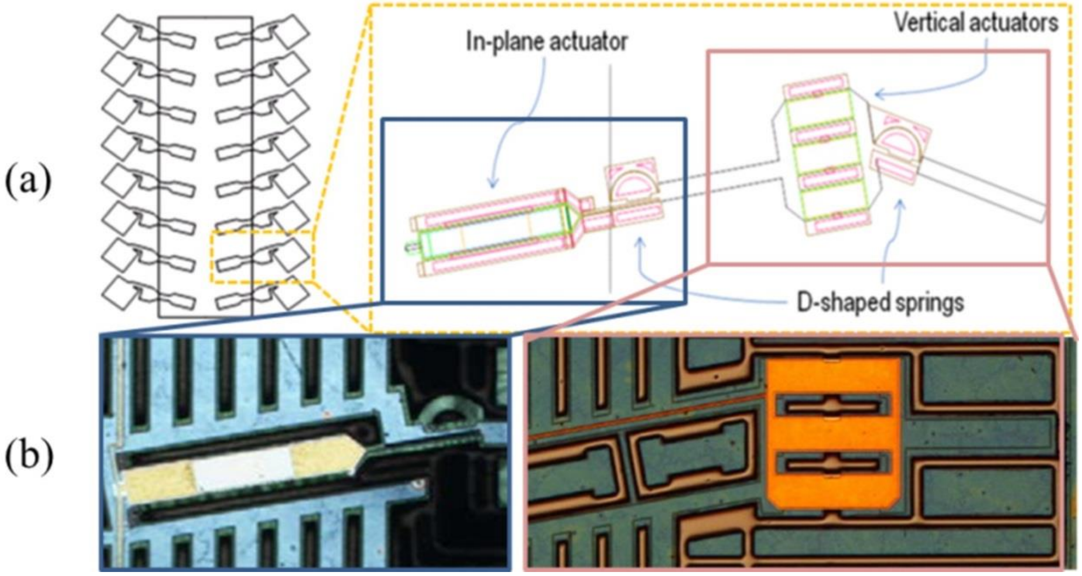

Figure 4.1 (a) Schematic top view and a leg system of millipede design (b) real photos of lateral and vertical actuators

In this task, using the proposed experimental modal identification procedure, vertical motion of the robot is modeled. However, since the current prototype device is in-chip as shown in figure 4.2 and capable of vertical actuation only, experimental data is limited to vertical motion at the center of the robot body. Thus, dynamic modeling is based on single degree-of-freedom system. The model is then plugged into a lumped dynamic model of both vertical and lateral motions of the body and two alternating legs with the foot-terrain interaction model applied. This model uses estimated effective point-mass of a leg and lateral dynamics of the robot. The walking model is simulated with a numerical engineering tool, MATLAB^{TM}. The simulation studies with this model investigate the effects of various ground conditions on the robot locomotion. Such ground conditions include electrostatics, adhesion, squeeze-film damping, and CoR, which are modeled based on the findings from the previous tasks with the micro-cantilever and the "bulk" piezoelectric ceramic micro-robots. By perturbing such factors, influences of ground conditions on the walking dynamics are investigated and analyzed. The result from this task is expected to provide helpful idea for design of both leg geometries and control input sequences that are robust against variation of the ground conditions.

4.2 Test Micro-Robot: Millipede Design

While a hexapod or quadruped robot design has many potential benefits for micro-scale walking robots, such as space to provide a large range of motion at the tip of a leg with m-DoF motion, there are weaknesses due to delicate structures with small number of legs: relatively low weight bearing capacity and large influence of leg actuation failure. To compensate these weaknesses, a millipede design was developed by increasing number of legs with sacrifice of the range of motion of single leg stroke. Figure 4.2 shows real photos of the millipede prototypes released from wafers, indicating locations of the lateral and vertical actuators. (The two sub-photos are of the different prototypes but included here for the description of the actuator locations.) The detailed geometry of single leg dimensions was determined by a design optimization process using simple multi-body dynamic model as shown in figure 4.3 and the dimensions including the optimized parameters of single leg configuration are shown in table 4.1. Among the shown parameters, only the lengths of the links are the optimized variables, while stiffness and damping properties were previously obtained from actuator modeling and experimental characterization. More detailed explanation of this model will be presented in the following section.

Table 4.1. Parameters for out-of-plane leg model of millipede prototype robot

parameters	values	description
L_S	$2.5\text{x}10^{-4}$ m	length of the shin
L_T	$2.5\text{x}10^{-4}$ m	length of the thigh
L_H	$2.5\text{x}10^{-4}$ m	length of the hip
$k_{op,l}$	$1.05\text{x}10^{-5}$ Nm	out-of-plane stiffness of lateral actuator
$b_{op,l}$	$3.4\text{x}10^{-9}$ Nms	out-of-plane damping coefficient of lateral actuator
$k_{op,v}$	$7.74\text{x}10^{-8}$ Nm	out-of-plane stiffness of vertical actuator
$b_{op,v}$	$1.2\text{x}10^{-10}$ Nms	out-of-plane damping coefficient of vertical actuator
τ_{op}	0.0057 Nm	torque input generated by vertical actuator at the hip

For leg actuation, the same thin-film piezoelectric actuation mechanism shown in figure 1.3a and 1.3c is used for both hexapod and millipede prototypes. Vertical and lateral actuators are separately operated to increase maneuverability and enlarge the manipulation workspace.

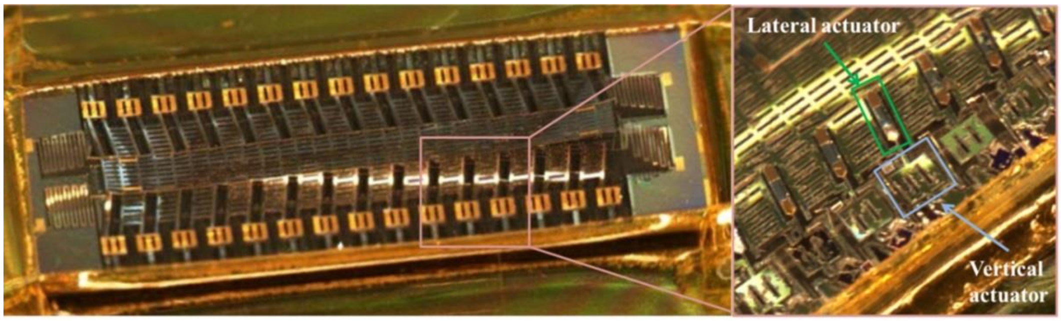

Figure 4.2 Released millipede prototype

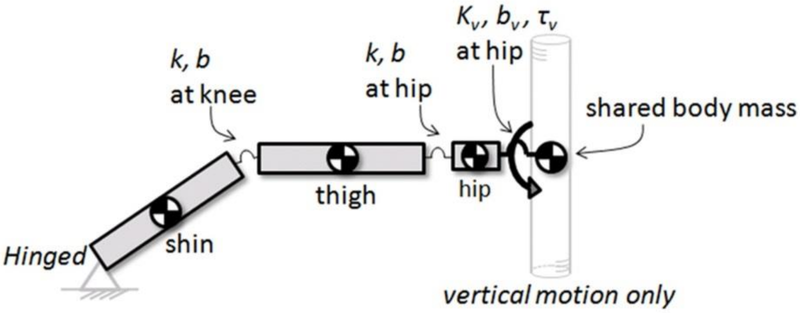

Figure 4.3 Planar out-of-plane dynamic model for design optimization of the prototype leg

The currently tested prototype, however, which is the first of the millipede designs to have been completed, does not have lateral actuators. Thus, only vertical motion can be measured experimentally. Since several prototypes with both lateral and vertical actuators have been recently manufactured, they will be tested and analyzed in the near future.

4.3 Modeling Procedure

4.3.1 Dynamic model of vertical motion of the robot body

4.3.1.1 *Multi-body dynamic model for design optimization*

As shown in figure 4.3, the multi-body dynamic model used for the leg configuration design in the previous section is based on several assumptions: a simply-supported foot-terrain contact point, a point mass body, and body motion limited to vertical displacement with no friction. A dynamic equation of motion for vertical actuation is derived by Newton-Euler equations. For design, optimization concept was used based on the following objective function,

$$\max_{\kappa} \dot{y}_b\left(t_f\right) \quad \text{s.t.} \quad y_b\left(t_f\right) > 0 \tag{4.1}$$

where, y_b indicates the vertical displacement of the body mass and t_f is the time when the response reaches the first peak. κ represents a set of the design parameters,

$$\kappa \triangleq \left\{L_S, \quad L_T, \quad L_H,\right\} \tag{4.2}$$

As described in table 4.1, these are the lengths of the links of a leg. Shown in equation 4.1 is that the objective of the design optimization is focused on maximization of average velocity and weight bearing capacity over a specific period of time. This model is validated with experimental comparison later in this section **4.3.1**.

4.3.1.2 *Dynamic model derived by modal analysis on experimental data*

In addition to the multi-body dynamic model prepared prior to experimental testing, an empirical model is derived using experimental data to apply and validate the dynamic modeling procedure introduced in the previous tasks. Among the manufactured prototype devices, one with only vertical actuators was tested and analyzed, so far. Therefore, experimental investigation is focused on measuring vertical motion of the robot body responding to 14 V step inputs. Like the modeling procedures in the previous tasks, modal identification is applied to the acquired experimental data and then the derived equations of motion are mapped to physical system with mass, damping, and stiffness matrices. Since the device is in-chip and all feet are not detached from the board, the model is a single-DoF system and mathematical expression is as follows,

$$m_b \ddot{y}_b + c_{b,v} \dot{y}_b + k_{b,v} y_b = G_v V(t) \tag{4.3}$$

where m_b indicates the effective mass of the robot body, $c_{b,v}$ and $k_{b,v}$ are damping and stiffness coefficients, respectively. y is the vertical displacement of the body and G_v is the voltage gain to force and V is voltage input. The voltage gain, G_v, is treated as a linear constant, as only a constant voltage is applied.

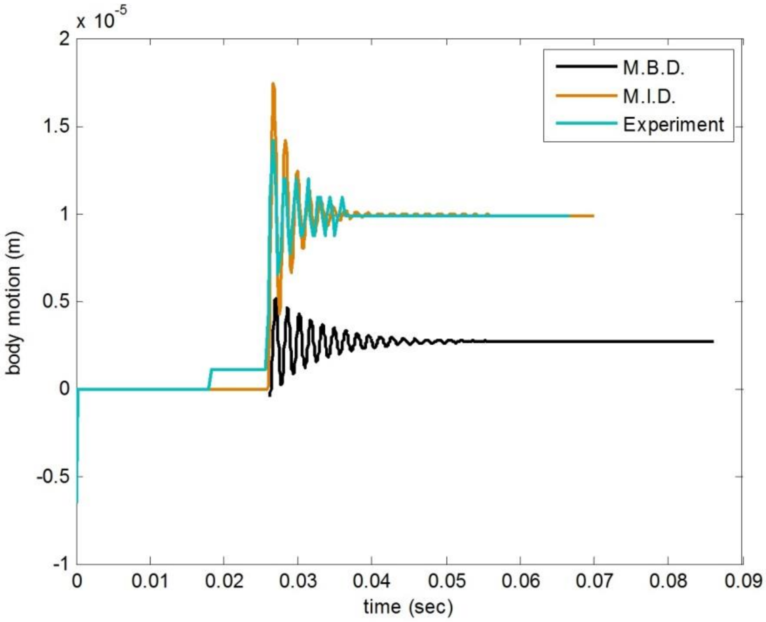

Figure 4.4 Body motion comparison between Multi-Body Dynamic (MBD) model, Modal Identification Dynamic (MID) model, and experimental data

Figure 4.4 shows comparison of the response to a 14 V step input of the three different cases: the multi-body dynamic model used for the design, the modal identification model represented by equation (4.3) and the experimental data. The magnitude of the multi-body dynamic model is rather small but the governing frequencies of all data are similar even though the multi-body dynamic model is not based on the experimental data. This is likely because the out-of-plane stiffness of the knee joint in the multi-body dynamic model is assumed very large compared to that of the hip. This implies that the vertical motion of the body is mostly contributed by only single vertical actuation at the hip, and such vertical actuators are less prone to fabrication error. It should also be noted that while the original displacement estimate was too low, the vertical displacement is projected from an oblique camera angle, and should be treated as only approximate.

4.3.2 Lumped dynamic model for locomotion

Since the current test prototype is in-chip and feet are not released from the chip as shown in figure 4.2, the measuring point of the device is limited to the center of the body. Thus, instead of using the dynamic modeling procedure proposed in the previous tasks for the entire robot structure, a dynamic model for walking simulation is derived by assuming 3-object lumped linear dynamic system as shown in figure 4.5. For structural characteristics such as stiffness and damping ratio between the body and the feet, the dynamic model represented by equation (4.3) in the previous section is plugged into a lumped dynamic model for the robot walking simulation. As illustrated in figure 4.5, motions of two switching legs and the corresponding amount of the body mass are considered. The effective mass of a leg is estimated roughly with structural dimensions and added to the model. Hence, the equations of vertical motion are composed as follows,

$$\mathbf{M} = \begin{bmatrix} m_b & 0 & 0 \\ 0 & m_l & 0 \\ 0 & 0 & m_l \end{bmatrix}, \mathbf{C_V} = \begin{bmatrix} 2c_{b,v} & -c_{b,v} & -c_{b,v} \\ -c_{b,v} & c_{b,v} & 0 \\ -c_{b,v} & 0 & c_{b,v} \end{bmatrix}, \mathbf{K_V} = \begin{bmatrix} 2k_{b,v} & -k_{b,v} & -k_{b,v} \\ -k_{b,v} & k_{b,v} & 0 \\ -k_{b,v} & 0 & k_{b,v} \end{bmatrix} \quad (4.4)$$

where, **M** is the mass matrix consisting of the body mass, m_b, and two of the estimated leg mass, m_l. $\mathbf{C_V}$ and $\mathbf{K_V}$ are the damping matrix and the stiffness matrix, respectively. Here, $c_{b,v}$ and $k_{b,v}$ are the damping and the stiffness coefficients experimentally obtained in the previous section. The equations of the vertical lumped dynamics can be then expressed as follows,

$$\mathbf{M}\ddot{\mathbf{X}}_{\mathbf{V}} + \mathbf{C}_{\mathbf{V}}\dot{\mathbf{X}}_{\mathbf{V}} + \mathbf{K}_{\mathbf{V}}\mathbf{X}_{\mathbf{V}} = \mathbf{F}_{\mathbf{D,V}} + \sum \mathbf{F}_{\mathbf{SS}} + \mathbf{F}_{\mathbf{I}} \tag{4.5}$$

here, $\mathbf{X}_{\mathbf{V}}$ represents vertical displacements of the body and the two switching legs. $\mathbf{F}_{\mathbf{D,V}}$ is the driving input force vector, and $\mathbf{F}_{\mathbf{SS}}$ and $\mathbf{F}_{\mathbf{I}}$ are the short-range force vector and the impact force vector, respectively. For the contact/impact model, the model proposed in analysis of the micro-cantilever test structure is applied here. That is, contact interaction is approximated with the short-range forces and restitution ratio, and the starting values for such factors are selected based on the quantification results in the micro-cantilever testing since it is originally intended to have dynamic environment similar to that of the thin-film walking robots.

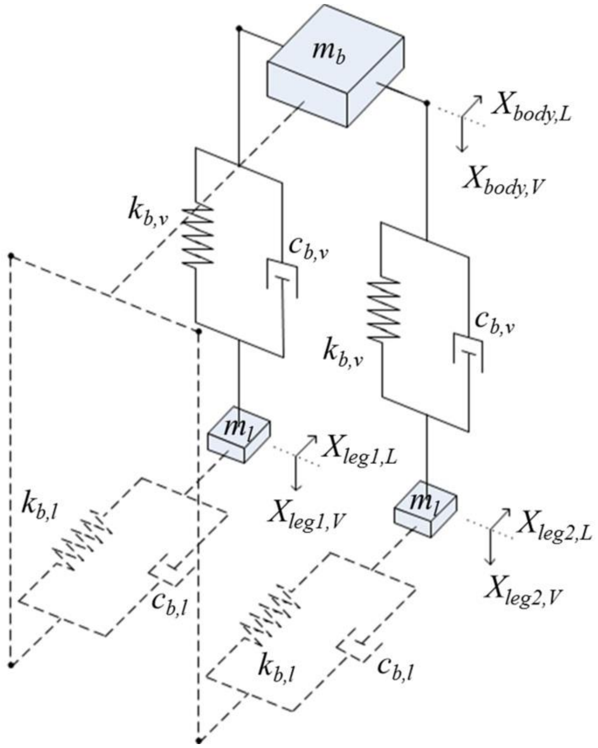

Figure 4.5 Schematic diagram of lumped dynamic model for walking simulation

Additionally, since lateral motion of the body is not experimentally measured and characterized, the lateral dynamic system is approximated based on rough calculation using structural dimensions. The following is the mathematical expression of the lateral dynamic model,

$$\mathbf{M}\ddot{\mathbf{X}}_{\mathbf{L}} + \mathbf{C}_{\mathbf{L}}\dot{\mathbf{X}}_{\mathbf{L}} + \mathbf{K}_{\mathbf{L}}\mathbf{X}_{\mathbf{L}} = \mathbf{F}_{\mathbf{D,L}} + \mathbf{F}_{\mathbf{f}} \tag{4.6}$$

where, $\mathbf{C_L}$ and $\mathbf{K_L}$ are the damping matrix and the stiffness matrix for lateral dynamics, respectively, and $\mathbf{F_{D,L}}$ is the driving input force vector for lateral actuation and $\mathbf{F_f}$ is the friction force active only when a foot is in contact with the ground. This friction force is currently arbitrary and assumed to be related to adhesion force in vertical dynamics since experimental analysis on lateral motion of the robot has not been conducted and friction force behavior during locomotion has not been analyzed.

In simulation, equations (4.5) and (4.6) simultaneously run over time for vertical and lateral dynamics of the robot locomotion and affect each other whenever a contact with the ground occurs. The flowchart in figure 4.6 shows this contact algorithm. As illustrated, only when a foot makes a contact with the ground and friction force exists so that the foot on the ground can push the body, the robot can proceed forward. In the meantime, various short-range contact forces and a CoR affect the vertical motion of the foot.

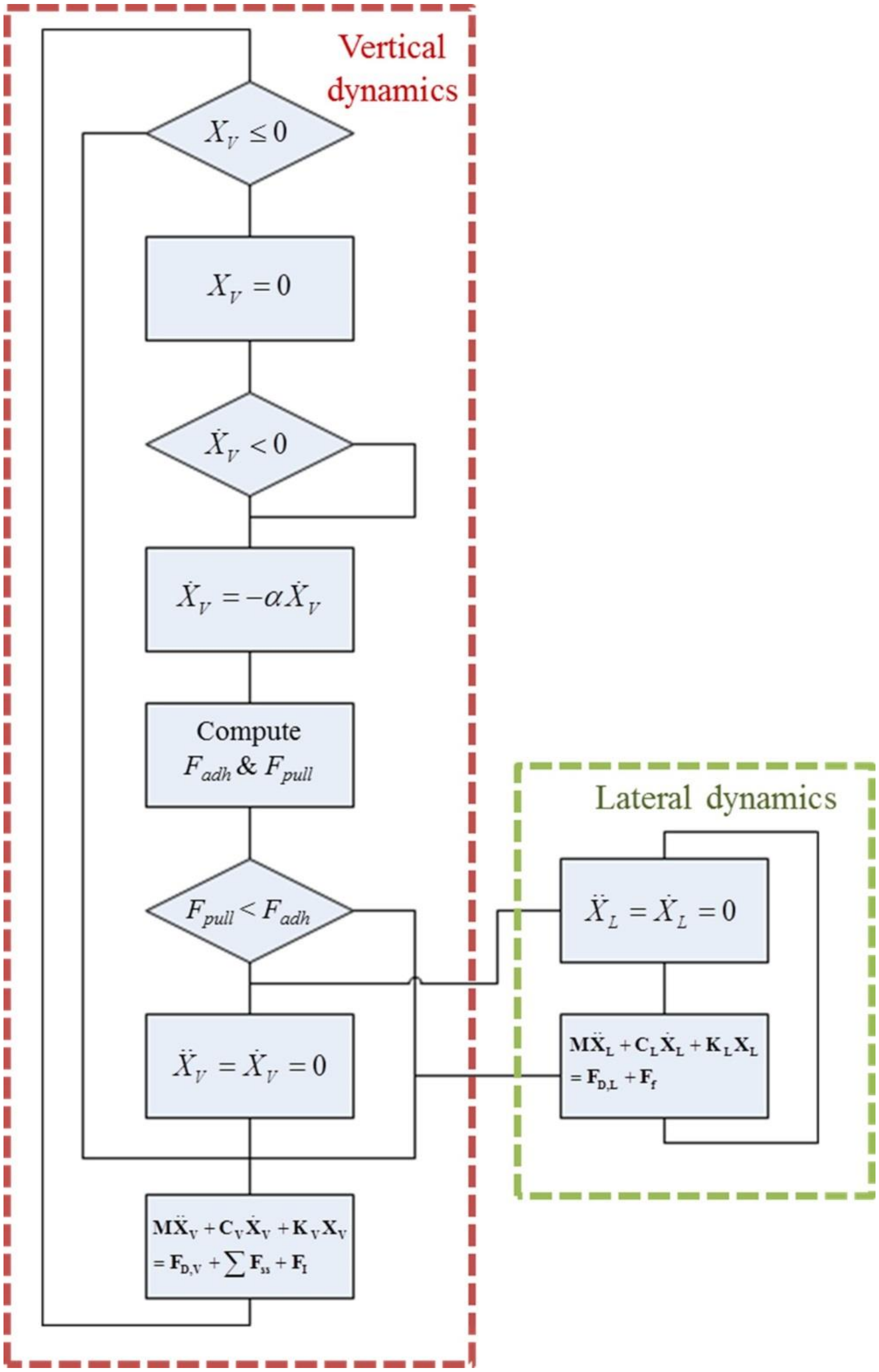

Figure 4.6 Flowchart of lumped dynamic model algorithm

4.4 Simulation Studies of Locomotion

4.4.1 Simulation studies with foot-terrain interaction

With the lumped dynamic model for locomotion of the millipede robot introduced in the previous section, a series of simulation studies are carried out. The objective of the simulation studies is characterization of the effects of the ground conditions on walking dynamics of the micro-robot on account of design of the on-off input sequences robust against variance/changing of the ground conditions.

In more detail, by perturbing coefficients of the short-range contact forces and the CoR, their effects on the system dynamics are characterized by analyzing the time-series responses based on the given conditions. As the reference/starting ground conditions, the results of the micro-cantilever testing are applied. The perturbation ranges of such coefficients are shown in table 4.2.

Table 4.2 Ranges of the tested coefficients of the ground conditions in simulation studies

	Range	**Related phenomenon**
C_e	$1\text{x}10^{-13} \sim 1\text{x}10^{-7}$ nNm^2/V^2	Electrostatics
C_{sfd}	$1\text{x}10^{-18} \sim 1\text{x}10^{-15}$ nNm^{2}s	Squeeze-film damping
C_{adh}	$1\text{x}10^{-8} \sim 0.1$ N/s	Adhesion
α (CoR)	$0.1 \sim 0.9$	Coefficient of restitution

Figure 4.7 shows examples of simulation studies with two different ground conditions, implying ground conditions significantly affect the walking behavior. For example, much greater body oscillation is produced in the first case, as a consequence of much different electrostatic attraction.

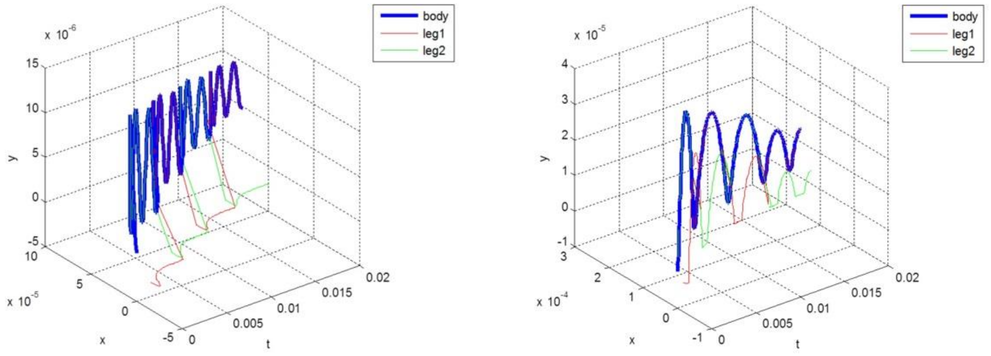

(a) *(b)*

Figure 4.7 Simulation examples showing both vertical and lateral displacement in time domain (a) $C_e = 1 \text{x} 10^{-8}$, $C_{sfd} = 1 \text{x} 10^{-18}$, $C_{adh} = 1 \text{x} 10^{-8}$, $\alpha = 0.7$
(b) $C_e = 1 \text{x} 10^{-12}$, $C_{sfd} = 1 \text{x} 10^{-18}$, $C_{adh} = 1 \text{x} 10^{-2}$, $\alpha = 0.7$

Motivated by the above examples, by changing factors of ground conditions such as the coefficient of the electrostatic force, trends of their influences were analyzed. Figure 4.8-10 show the trends in time-domain walking dynamics of each short-range contact force, respectively. As electrostatic force increases, maximum amplitudes of vertical motion of the body and the legs decrease and the in-plane travel displacement of the system also decreases. On the contrary, the number of foot bounces on the ground and the foot-terrain contact duration increase. It should be noted that there are critical values of the electrostatic coefficient that provide a local maximum and minimum of vertical displacement, number of bounces, and contact duration. The other two short-range forces show similar trends that there is a critical value of each coefficient that represents the maximum travel displacement. One difference between the two forces is that the number of bounces keeps decreasing as adhesion increases. As the trend of weight of a payload, various values of body mass were also simulated. As shown in figure 4.11, a heavier payload results in smaller vertical displacement of the body as well as the in-plane travel distance, as would be expected. The number of bounces anticipated also increases for a heavier payload while contact duration decreases as the weight becomes larger than some critical value, 0.2 mg in the plot.

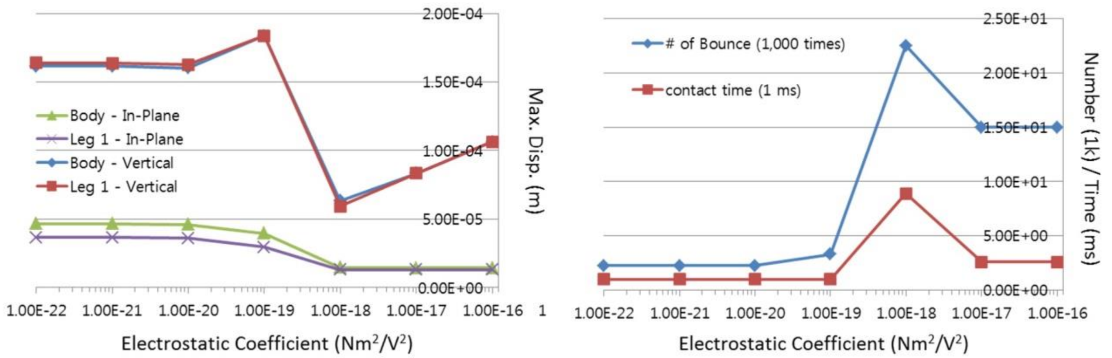

(a) *(b)*

Figure 4.8 Trends of walking dynamic characteristics over electrostatic coefficient, C_e (a) maximum displacement in vertical and lateral directions (b) number of bounces and maximum contact duration

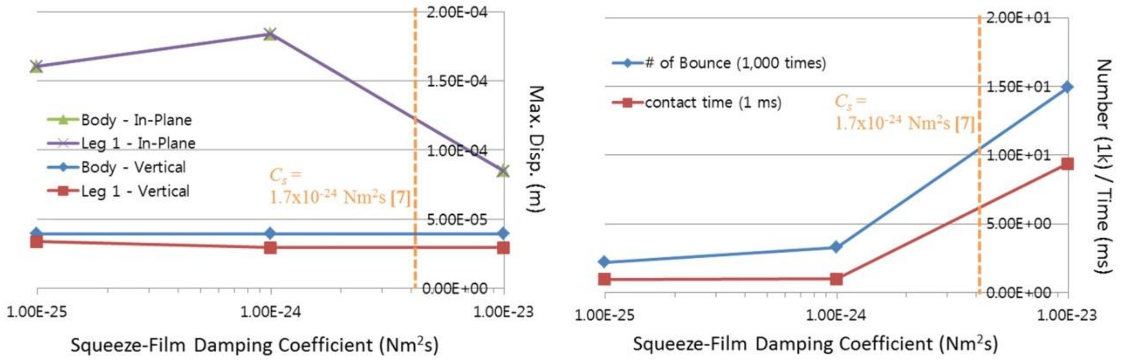

(a) *(b)*

Figure 4.9 Trends of walking dynamic characteristics over squeeze-film damping coefficient, C_{sfd} (a) maximum displacement in vertical and lateral directions (b) number of bounces and maximum contact duration

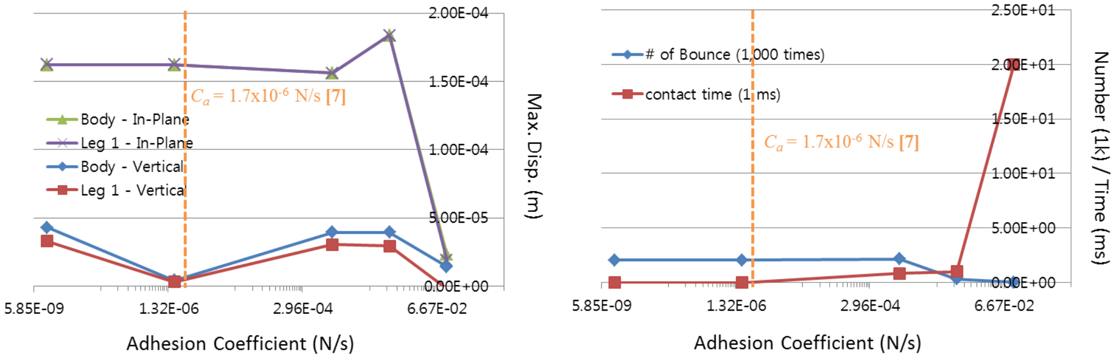

(a) *(b)*

Figure 4.10 Trends of walking dynamic characteristics over adhesion coefficient, C_{adh} (a) maximum displacement in vertical and lateral directions (b) number of bounces and maximum contact duration

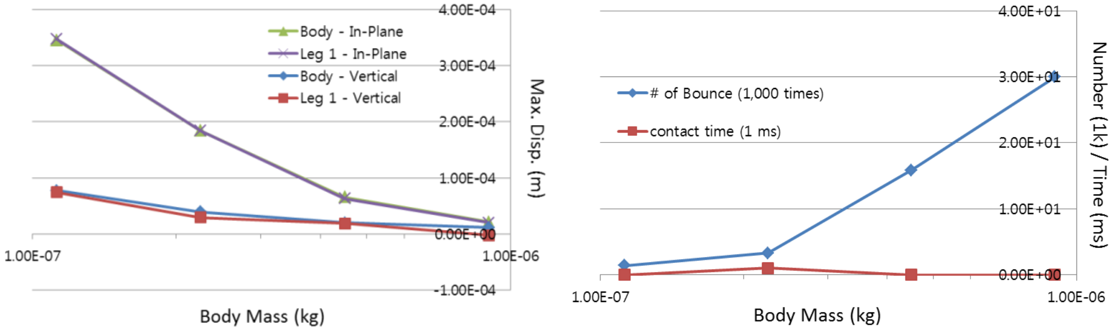

(a) *(b)*

Figure 4.11 Trends of walking dynamic characteristics over body mass, m_b (a) maximum displacement in vertical and lateral directions (b) number of bounces and maximum contact duration

4.4.2 Concepts for control input sequence design

Since there is no thin-film PZT walking robot prototype fully released from wafers, locomotion testing on a robot and verification of the simulation model are not available. Thus, in this work, only several potential suggestions for design of the input sequences are presented. More explicit design of the control input sequences will be conducted in the near future when the thin-film PZT walking robot prototypes are available for testing.

The results achieved by the simulation studies can be used for design of control input sequences that increases some dynamic performances during locomotion such as average vertical displacement of the body, maximum travel distance with small input energy. Although implementation of piezoelectric sensors in micro-structures is on-going, it is not easy to utilize them for feedback control due to large noise due to various disturbances described previously. Hence, the first possible control input design is the open-loop control. One of the previous works in the laboratory is an open-loop minimal energy on-off control strategy for single micro-robot leg shown in figure using optimization techniques for finding the best robust input sequence [6]. To this work, instead of considering the worst-case dynamic system with a bounded uncertainty, the worst-case ground conditions with a bounded range of the short-range contact forces can be applied.

If implementation of micro-sensors in the robot system is successfully realized and feedback control is possible, various control design strategies can be considered depending on specific objectives. For example, if the objective is the minimization of energy consumption with the desired displacement at a specific time, another previous work in the laboratory can be applied which is an on-off adaptive controller based on stochastic approximation [44]. If the objective is to obtain large adhesion at the contact area between feet and the ground for crawling on the wall, the objective can be focused on maximizing the contact duration using the numerical adhesion model included in the system dynamics previously derived.

4.5 Discussion

In this chapter, two different dynamic models for the vertical motion of a millipede leg were presented. One is a multi-body dynamic model, which is used for the leg configuration design, and the other is a model derived by modal identification with the measured data. These two models were then compared along with the measured data and it was shown that there is no large difference between them in natural frequency and damping behavior. This strengthens the reliability of the design optimization result for a single leg using the multi-body dynamic model.

Using the model derived by modal analysis, a lumped vertical walking model has been derived and a lumped in-plane dynamic model has been also derived by rough estimation with structural dimensions of the leg. Combining the lumped vertical and in-plane models, simulation studies for locomotion of the robot were conducted and the dynamic characteristics during walking were analyzed. It was confirmed that the ground condition significantly affects the system dynamics and there are some trends of the factors representing the ground condition such as electrostatics, adhesion, and squeeze-film damping. Considering that the numerical ranges of such forces are practical based on the results of the micro-cantilever test structure [11], these trends might be useful for the further investigations on the walking dynamic behavior of thin-film PZT walking robots as well as for design of input sequences robust and energy-efficient against changeable/unknown environmental conditions.

However, there are key limitations in this task that weaken the reliability of the simulation results. The first and the most important limitation is that the lumped model for walking dynamics combining the vertical and in-plane dynamics is derived based on many assumptions that have yet to be experimentally verified. Although the vertical dynamics is derived based on the experimental data, it is only of the vertical motion of the body and the effective mass of a leg as well as the in-plane dynamics are roughly calculated. Furthermore, even though the millipede prototype has more compliant localized joints/actuators compared to the “bulk” PZT robotic structures [12], the system still has continuous structure with high resonant frequencies at joints. Thus, to increase the reliability of the combined model for analysis of the walking dynamics, it is required to replace it with more accurate dynamic models for both vertical and in-plane motions using the modeling procedure proposed [11][12]. To further increase the reliability of this task, more experimental analysis with different ground pads representing various short-range contact forces at the foot-terrain interaction can be used for validation of the results.

Although design of control input sequences is not presented in this work due to absence of a thin-film PZT robot prototype completely released from a wafer, the results from the simulation studies imply that such simulation studies may provide some bounded conditions for design of robust control input sequences with low energy consumption for both open-loop and closed-loop control strategies. The simulation studies can be also utilized for design of input sequences for other specific objectives such as high adhesion between feet and the ground and minimum oscillation of the body, etc. Again, reliability of this simulation studies can be improved in the future by the dynamic models derived by the modeling procedure proposed in the previous tasks if more prototypes which are capable of both vertical and in-plane actuation or fully released from wafers are available for testing.

CHAPTER 5

CONCLUSION

5.1 Conclusion and Discussion

5.1.1 Summary

The key results in this dissertation can be summarized as follows, with details on the respective components to follow:

- Modeling of small-scale contact forces without knowledge of contact surface geometries and material characteristics.
- Dynamic modeling of walking micro-robotic structures.
- Simulation studies with a thin-film micro-robot prototype, millipede.

5.1.2 Modeling of small-scale contact forces without knowledge of contact surface geometries and material characteristics

Using a cantilever-type thin-film piezoelectric actuator, this task introduced a procedure for model identification of contact dynamics of a piezoelectric microsystem without full knowledge of contact surface geometry. The model uses simple lumped-parameter components that whose parameters can be identified with relatively simple experimentation. Certain piezoelectric nonlinearities plus squeeze-film damping and adhesion effects and a coefficient-of-restitution characterizing the surfaces in question are incorporated into the model. Experimental validation indicates that the model overall provides a fair approximation of transient and periodic behavior over various driving frequencies and waveforms in time series responses. Effects that are captured well include amplitude and phase shifts in response to sinusoidal inputs, presence or absence of bouncing at contact, and attenuation rates of transient oscillations. Less well modeled are the peak amplitude of oscillation, duration of contact and high mode oscillation in the air at driving frequencies faster than 50Hz, although in most cases agreement of experimental and simulated responses are quite good.

The results of this modeling effort are next applied to more practical device applications. The primary application area is micro-robotics, where even though it is difficult to predict coefficients before hand over many terrains, for design of gait inputs a designer can look at the response to system inputs over a range of coefficients, and pick input sequences producing a robust response. In other circumstances, it may be possible to perform partial or complete identification while initiating locomotion and use the resulting information to provide trajectories with desirable behavior.

5.1.3 Dynamic modeling of walking micro-robotic structures

Using two different prototype micro-robots operated with bulk PZT ceramics, this task proposes a modeling procedure for the robots' foot-terrain interaction including characterization of structural dynamics and impact behavior as well as quantification of a few small-scale contact forces. Structural dynamics were modeled by conventional modal analysis and are based on a lumped-parameter fashion with relatively small system orders. This feature simplifies system identification process with a limited number of parameters while the estimation is fairly good overall considering a variety of unknown factors that might significantly affect the system dynamics, such as exact geometries or material properties of contact surfaces.

The impact model is described by a CoR matrix which is based on the two fundamental assumptions; that coefficient of restitution at the contact foot is constant over various voltage input signals for a specific ground surface and instant motion of a continuous structure at the moment of impact is governed by a dominant mode shape which is determined by location and direction of the impact. These assumptions were validated by numerical analysis on the "processed" experimental data which is obtained by synchronizing and subtracting the experimental data sets with and without the existence of contact. By experimental validation, it was shown that a single mode shape might be adequate to approximate the system response to instantaneous impact disturbance. For the HBPZTR, experimental observation revealed a few small-scale contact forces have significant influence on dynamic response within about 30 μm gap between a foot and the ground for robots less than 0.2 g in mass. Observing system responses over various gaps between surfaces, ground pads with different length to isolate each short-range force, and static voltage applied to them, such forces were quantified and included into the model.

Further experimental validation shows that the proposed model for each prototype micro-robot provides relatively good approximations to a variety of test environments with different voltage inputs and gaps between surfaces. It should be noted that only one leg at a time has been operated and single contact point has been tested on purpose since the work in this paper is the starting point for modeling of the foot-ground interaction phenomena during micro-robot walking. Multiple contact point interaction over walking is a major need as future work.

5.1.4 Simulation studies with a thin-film micro-robot prototype, millipede

Though it is not possible for now to experiment on the thin-film micro-robots fully released from wafers, simulation studies with an analytical model obtained by combining the in-plane and out-of-plane dynamic models of thin-film millipede prototype have been carried out. Various phenomena that appeared in the preceding research on the cantilever and the bulk PZT robots, such as foot's chattering on the ground and magnitude reduction due to electrostatics, could be also observed in the simulation.

However, the effective coefficients of the small-scale forces and COR should be identified via further experimental analysis. Furthermore, the simulation model assumes that there exist only two modes in the motion of the legs for a single walking cycle. That is, all the legs can be replaced with two imaginary legs, switching each other's role: supporting and lifting. However, since the real robot motion during locomotion may not be perfectly symmetric based on the gait sequence it uses, this assumption could not be valid. Therefore, it is hardly possible to estimate the real thin-film micro-robot locomotion with these simulation studies.

For all that, it is likely that the foot-terrain interaction model obtained by the preceding research also provides a reasonable result in this simulation model with a similar range of magnitudes for the small-scale forces. Moreover, it could also be seen via this simulation that the combination of the out-of-plane motion and the in-plane motion is important for efficient walking. This is because the foot should stay on the ground to push the ground backward for the pure forwarding motion of the body. Thus, another potential future work would be to design a control input sequence which may avoid any unnecessary vibration of the foot as it approach to the ground and increase the foot's rest time on the ground.

5.2 Future works

5.2.1 Design of on-off input sequences for vertical actuation of walking leg

The analysis on the micro-cantilever test structure and the bulk PZT micro-robots showed that how the small-scale forces may affect the vertical motion and the ground-impact responses of systems having dynamics representative of millimeter-scale micro-robots. However, these studies do not suggest what kind of driving force is necessary to achieve the high dynamic performance of the micro-robot legs. Moreover, as seen in the simulation studies with the millipede prototype, the vibration of the foot due to the vertical motion of the leg may significantly affect the walking performance of the robot since a pure forwarding motion can be achieved only when the foot of the supporting leg stays on the ground. Hence, it might be reasonable to assign as a future work to design an input signal that provides the high performance of the leg motion considering such small-scale forces in the micro-environment identified by the works so far. This work can be defined as design of an on-off input signal for vertical actuation of the leg that minimizes the unnecessary chattering of the foot on the ground by reducing the approaching velocity of the foot as it approaches to the ground. Figure 5.1 shows the conceptual plots of the vertical displacements of the body part and two switching legs as well as input voltages applied to them.

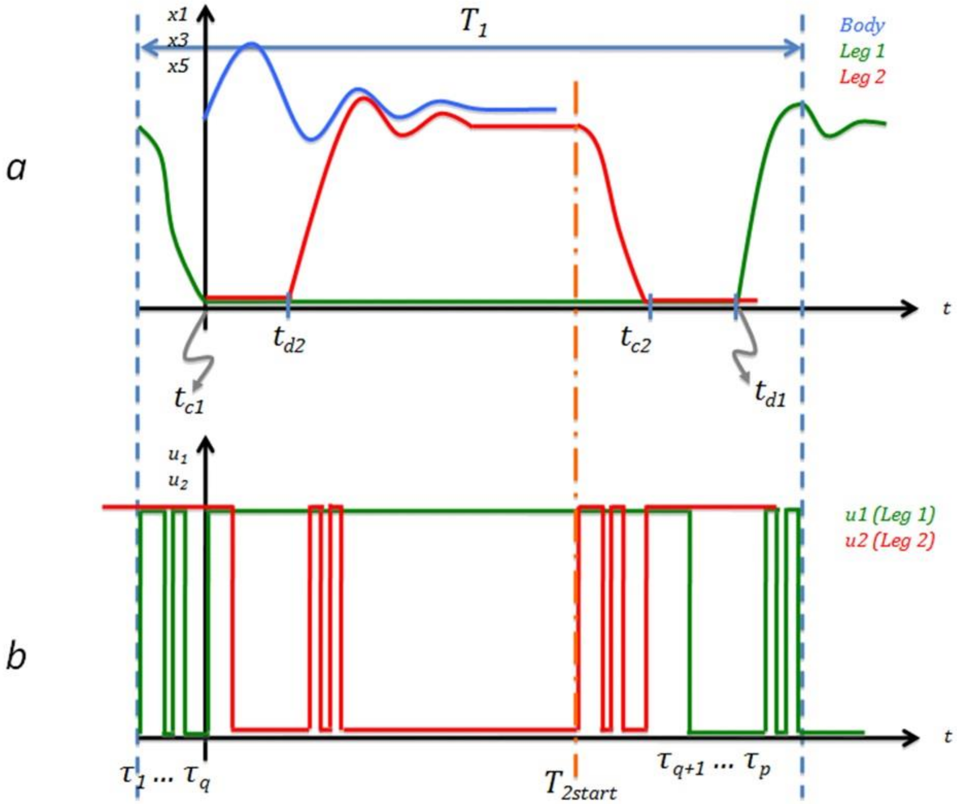

Figure 5.1 Optimal on-off voltage input for vertical actuation of leg

a. vertical displacement b. voltage inputs

As the figure shows, two legs switch their roles, supporting and lifting, and when a foot is falling, using a specific sequence of on-off voltage input, the velocity of the foot immediately before the collision to the ground will be minimized by using analytical and mathematical approach. Optionally, applying similar on-off signals will also minimize the unnecessary vibration of a foot right after the release from the ground. By this work combined with the foot-terrain interaction model we proposed and verified in Chapter 3, it is expected that a theoretical approach for efficient inputs can be established for the future use in design of the full locomotion model. In addition, these sequences can be tested in simulation against variations in surface conditions, to identify inputs that are likely to maintain efficient walking motions as the environment changes.

5.2.2 Testing of multiple-leg walking

The research conducted so far is mostly related to single leg operation at any point in time. That is, the design of the thin-film robot leg and the analysis of the micro-cantilever test structure are based on an individual leg system. Moreover, even the testing on the bulk PZT micro-robots is based on single leg operation with single leg ground interaction. Therefore, for more practical analysis of the micro-robot walking in the micro-environment, testing of multiple-leg operated micro-robot is essential. It is expected, though, that the previous analysis on single foot-terrain interaction carried out with the bulk PZT micro-robot will provide a fairly good starting point for this work.

5.2.3 Design of energy-efficient walking gait sequences

Assuming that all the works introduced above are successfully accomplished, it is expected that walking-gait sequences for the micro-robots providing high speed with low energy consumption can be designed. Figure 5.2 shows a basic concept considering two switching legs. As it illustrates, by designing an appropriate switching time of these two legs analytically, more effective forward motion can be achieved. In fact, since the thin-film walking micro-robots have relatively large numbers of legs, various combinations of walking leg sequences can be devised.

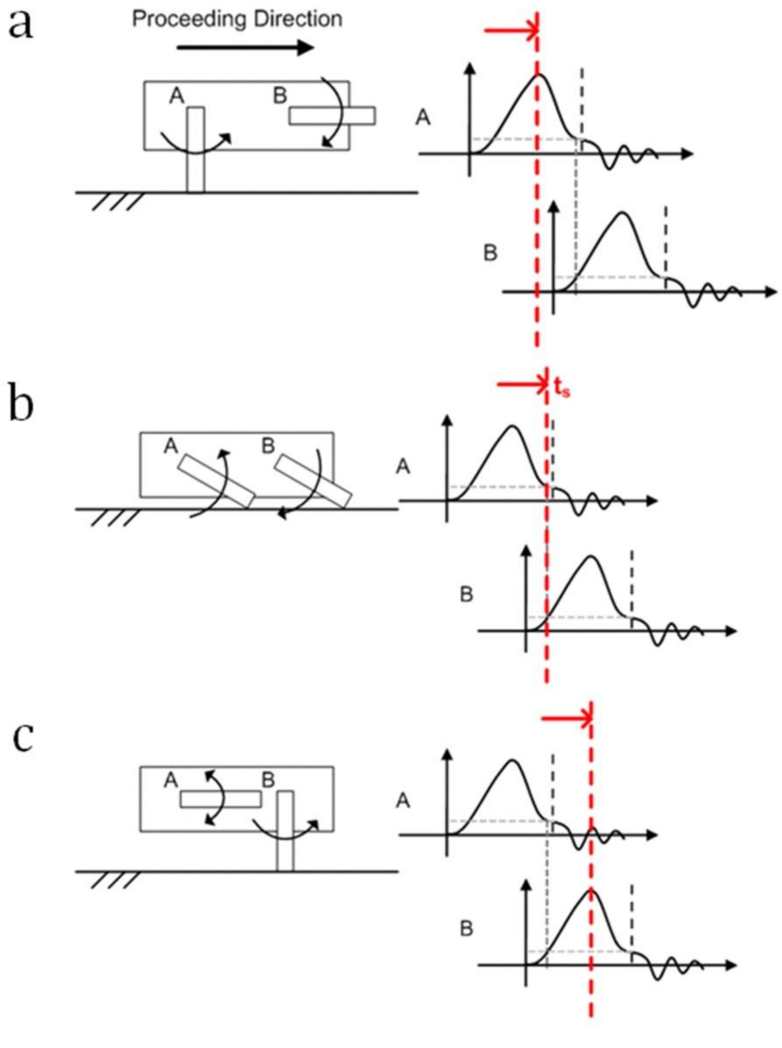

Figure 5.2 Conceptual diagram of gait sequence (a→b→c)

APPENDICES

Appendix A. Sampling of All Test Cases

A full set of measurements from 16 validation test cases is shown below in table A.1.

Table A.1 Sampling of 16 test cases

Freq. (Hz)	Volt. (V)	Signal	No. of bounces	Peak oscillation amplitude (μm)	Error	Contact duration (ms)	Error
5	6	Square	Sim: 2 Exp: 3	Sim: 211 Exp: 186	-13%	Sim: 97 Exp: 98	1%
5	6	Sine	Sim: 1 Exp: 1	Sim: 114 Exp: 125	9%	Sim: 31 Exp: 75	58%
5	8	Square	Sim: 1 Exp: 1	Sim: 264 Exp: 210	-25%	Sim: 99 Exp: 97	-2%
5	8	Sine	Sim: 0 Exp: 0	Sim: 136 Exp: 146	-7%	Sim: 72 Exp: 82	12%
15	6	Square	Sim: 0 Exp: 0	Sim: 216 Exp: 236	8%	Sim: 0 Exp: 0	0%
15	6	Sine	Sim: 0 Exp: 0	Sim: 114 Exp: 124	8%	Sim: 7 Exp: 24	70%
15	8	Square	Sim: 0 Exp: 0	Sim: 264 Exp: 212	-24%	Sim: 33 Exp: 32	-3%

15	8	Sine	Sim: 0 Exp: 0	Sim: 138 Exp: 148	-7%	Sim: 19 Exp: 26	26%
50	6	Square	Sim: 5 Exp: 3	Sim: 212 Exp: 160	-32%	Sim: 2.7 Exp: 5.1	47%
50	6	Sine	Sim: 1 Exp: 2	Sim: 114 Exp: 94	21%	Sim: 1.8 Exp: 5.4	67%
50	8	Square	Sim: 1 Exp: 1	Sim: 252 Exp: 184	-42%	Sim: 9.2 Exp: 8	-15%
50	8	Sine	Sim: 1 Exp: 1	Sim: 140 Exp: 152	8%	Sim: 5.1 Exp: 6.5	21%
100	6	Square	Sim: 0 Exp: 0	Sim: 205 Exp: 152	-34%	Sim: 0 Exp: 0	0%
100	6	Sine	Sim: 1 Exp: 1	Sim: 117 Exp: 137	15%	Sim: 0.4 Exp: 1.8	78%
100	8	Square	Sim: 1 Exp: 1~2	Sim: 264 Exp: 194	-36%	Sim: 4.2 Exp: 3.1	-35%
100	8	Sine	Sim: 1 Exp: 1	Sim: 142 Exp: 156	9%	Sim: 2.6 Exp: 2.3	-13%

Appendix B. Structural Models for the Tested Robots

	QBPZTR	HBPZTR
M	$\begin{bmatrix} 1.92E02 & -1.87E02 & -2.32E03 & -7.08E02 & 3.31E02 \\ -1.87E02 & 1.82E02 & 2.26E03 & 6.88E02 & -3.21E02 \\ -2.32E03 & 2.26E03 & 2.81E04 & 8.56E03 & -4.00E03 \\ -7.08E02 & 6.88E02 & 8.56E03 & 2.61E03 & -1.22E03 \\ 3.31E02 & -3.21E02 & -4.00E03 & -1.22E03 & 5.69E02 \end{bmatrix}$	$\begin{bmatrix} 10.57 & -13.17 & -5.69 & 29.09 & 18.71 & -13.30 \\ -13.17 & 23.18 & 9.62 & -44.63 & -23.94 & 23.62 \\ -5.69 & 9.62 & 4.42 & -19.50 & -10.26 & 9.90 \\ 29.09 & -44.63 & -19.50 & 92.42 & 52.25 & -45.29 \\ 18.71 & -23.94 & -10.26 & 52.25 & 33.44 & -24.10 \\ -13.30 & 23.62 & 9.90 & -45.29 & -24.10 & 24.40 \end{bmatrix}$
C	$\begin{bmatrix} 7.44E04 & -7.23E04 & -8.99E05 & -2.74E05 & 1.28E05 \\ -7.23E04 & 7.02E04 & 8.73E05 & 2.66E05 & -1.24E05 \\ -8.99E05 & 8.73E05 & 1.09E07 & 3.31E06 & -1.55E06 \\ -2.74E05 & 2.66E05 & 3.31E06 & 1.01E06 & -4.71E05 \\ 1.28E05 & -1.24E05 & -1.55E06 & -4.71E05 & 2.20E05 \end{bmatrix}$	$\begin{bmatrix} 9.95E01 & -1.10E02 & -4.99E01 & 2.63E02 & 1.77E02 & -1.04E02 \\ -1.10E02 & 2.83E02 & 1.23E02 & -5.77E02 & -2.38E02 & 2.88E02 \\ -4.99E01 & 1.23E02 & 5.78E01 & -2.56E02 & -1.04E02 & 1.27E02 \\ 2.63E02 & -5.77E02 & -2.56E02 & 1.23E03 & 5.48E02 & -5.89E02 \\ 1.77E02 & -2.38E02 & -1.04E02 & 5.48E02 & 3.38E02 & -2.30E02 \\ -1.04E02 & 2.88E02 & 1.27E02 & -5.89E02 & -2.30E02 & 3.02E02 \end{bmatrix}$
K	$\begin{bmatrix} 1.11E07 & -9.60E06 & -3.42E06 & 2.07E07 & 2.06E07 & -5.40E06 \\ -9.60E06 & 2.06E08 & 8.23E07 & -4.05E08 & -9.37E07 & 2.27E08 \\ -3.42E06 & 8.23E07 & 3.48E07 & -1.63E08 & -3.53E07 & 9.23E07 \\ 2.07E07 & -4.05E08 & -1.63E08 & 8.02E08 & 1.88E08 & -4.48E08 \\ 2.06E07 & -9.37E07 & -3.53E07 & 1.88E08 & 7.15E07 & -9.42E07 \\ -5.40E06 & 2.27E08 & 9.23E07 & -4.48E08 & -9.42E07 & 2.56E08 \end{bmatrix}$ $\begin{bmatrix} 8.51E07 & -8.65E07 & -1.01E09 & -3.21E08 & 1.49E08 \\ -8.65E07 & 8.82E07 & 1.02E09 & 3.27E08 & -1.52E08 \\ -1.01E09 & 1.02E09 & 1.20E10 & 3.79E09 & -1.77E09 \\ -3.21E08 & 3.21E08 & 3.79E09 & 1.21E09 & -5.63E08 \\ 1.49E08 & -1.52E08 & -1.77E09 & -5.63E08 & 2.62E08 \end{bmatrix}$	
$\mathbf{R}_{CoR}$	$\begin{bmatrix} 0.39 & 0 & 0 & 0 & 0 \\ -0.11 & 1 & 0 & 0 & 0 \\ -0.06 & 0 & 1 & 0 & 0 \\ -0.10 & 0 & 0 & 1 & 0 \\ -0.32 & 0 & 0 & 0 & 1 \end{bmatrix}$	$\begin{bmatrix} -0.50 & 0 & 0 & 0 & 0 & 0 \\ 0.59 & 1 & 0 & 0 & 0 & 0 \\ 0.97 & 0 & 1 & 0 & 0 & 0 \\ 0.40 & 0 & 0 & 1 & 0 & 0 \\ 0.42 & 0 & 0 & 0 & 1 & 0 \\ -0.42 & 0 & 0 & 0 & 0 & 1 \end{bmatrix}$

REFERENCES

[1] Ebefors T., Mattsson J. U., Kälvesten E., and Stemme G., 1999. "A Walking Silicon Micro-Robot". *The 10th Int. Conference on Solid-State Sensors and Actuators (Transducers '99)*, Sendai, Japan, June 7-10, 1999, pp 1202-1205.

[2] Gao B., Guo S., 2011. "Dynamic Mechanics and Electric Field Analysis of an ICPF Actuated Fish-like Underwater Microrobot". *Proceeding of the IEEE, Int. Conf. on Automation and Logistics, Chongqing, China, August, 2011,* pp 330-335

[3] Donald B. R., Levey C. G., McGray C. D., Paprotny I., and Rus D., 2006. " An Untethered, Electrostatic, Globally Controllable MEMS Micro-Robot". *Journal of Microelectromechanical Systems*, 15(1), pp 1-15.

[4] Yesin K. B., Vollmers K., and Nelson B. J., 2006. "Modeling and Control of Untethered Biomicrorobots in a Fluidic Environment Using Electromagnetic Fields". *The International Journal of Robotics Research*, 25(5-6), pp 527-536

[5] Rhee C.-H., Pulskamp J. S., Polcawich R. G., and Oldham K. R., 2012. "Multi-Degree-of-Freedom Thin-Film PZT-Actuated Microrobotic Leg". *Journal of Microelectromechanical Systems*, 21(6), pp 1492-1503.

[6] Edamana B., Hahn B., Pulskamp J. S., Polcawich R. G., and Oldham K., 2011. "Modeling and Optimal Low-Power On-Off Control of Thin-Film Piezoelectric Rotational Actuators". *IEEE/ASME Transaction on Mechatronics*, 16(5), pp 884-896.

[7] Do C., Cychowski M., Lishchynska M., Hill M., and Delaney K., 2010. "Integrated Modeling of Nonlinear Dynamics and Contact Mechanics of Electrostatically Actuated RF-MEMS Switches". *Annual Conference on IEEE Industrial Electronics Society (Glendale AZ)*, pp 2293-2298.

[8] McCarthy B., Adams G. G., McGruer N. E., and Potter D., 2002. "A Dynamic Model, Including Contact Bounce, of an Electrostatically Actuated Microswitch". *Journal of Microelectromechanical Systems*, 11(3), pp 276-283.

[9] Czaplewski D. A., Dyck C. W., Sumali H., Maddad J. E., Kuppers J. D., Reines I., Cowan W. D., and Tigges C. P., 2006. “A Soft-Landing Waveform for Actuation of a Single-Pole Single-Throw RF MEMS Switch”. *Journal of Microelectromechanical Systems*, 15(6), pp 1586-1594.

[10] Wang T., and Asokanthan S. F., 2011. “Bouncing Dynamics in MEMS Based Switching Structures”. *Proc. Of ENOC (Rome, Italy)*.

[11] Ryou J. H., and Oldham K. R., 2012. “Model Identification for Impact Dynamics of a Piezoelectric Microactuator”. *J. Micromech. Microeng.,* 22, pp 115002.

[12] Ryou J. H., and Oldham K. R., 2013. “Characterization of Foot-Terrain Interaction of Piezoeletrically Actuated Micro-Robots”. Submitted *to Smart Materials and Structures*.

[13] Lee S. I., Howell S. W., Raman A., and Reifenberger R., 2002. “Nonlinear Dynamics of Microcantilevers in Tapping Mode Atomic Force Microscopy: a Comparison between Theory and Experiment”, *Physical Review B*, 66, pp 115409-1-115409-10.

[14] Hagleitner C., Bonaccio T., Rothuizen H., and Eleftheriou E. 2007. “Modeling, Design, and Verification for The Analog Front-End of a MEMS-Based Parallel Scanning-Probe Storage Device”. *IEEE Journal of Solid-State Circuits*, 8, pp 1779-1789.

[15] Guo Z. J., McGruer N. E., and Adams G. G., 2007. “Modeling, Simulation and Measurement of The Dynamic Performance of an Ohmic Contact, Electrostatically Actuated RF MEMS Switch”, *Journal of Micromechanics and Microengineering*, 17, pp 1899-1909.

[16] Field R. V., and Epp D. S., 2006. “Development and Calibration of a Stochastic Dynamics Model for The Design of a MEMS Inertial Switch”. *Sensors and Actuators A*, 134, pp 109-118.

[17] Teodurescu M., Theodossiades S., and Rahnejat H., 2008. “Impact Dynamics of Rough and Surface Protected MEMS Gears”. *Tribology international*, 42, pp 197-

205.

[18] Decuzzi P., Demelio G. P., Pascazio G., and Zaza V., 2006. "Bouncing Dynamics of Resistive Microswitch with an Adhesive Tip". *Journal of Applied Physics*, 100, pp 024313.

[19] Park Y. H., Miyazaki Y., and Park K. C., 2003. "High Fidelity MEMS Switch Model". *Nanotechnology*, 1, pp 416-419.

[20] LaRose R. P., and Murphy K. D., 2009. "Impact Dynamics of MEMS Switches". *Nonlinear Dynamics*, 60(3), pp 327-339.

[21] Granaldi A., and Decuzzi P., 2006. "The Dynamic Response of Resistive Microswitches: Switching Time and Bouncing". *Journal of Micromechanics and Microengineering*, 16(7), pp 1108.

[22] Zhang W., Baskaran R., and Turner K., 2003. "Tuning The Dynamic Behavior of Parametric Resonance in a Micromechanical Oscillator". *Applied Physics Letters*, 82, pp 130.

[23] Oldham K., Rhee C.-H., Ryou J. H., Polcawich R., and Pulskamp J., 2009. "Lateral Thin-Film Piezoelectric Actuators for Bio-Inspired Micro-Robotic Locomotion". *ASME Micro- and Nano-systems Symposium (San Diego, CA)*.

[24] Qiu Z., Pulskamp J., Lin X., Rhee C.-H., Wang T., Polcawich R., and Oldham K., 2010. "Large Displacement Vertical Translational Actuator Based on Piezoelectric Thin Films". *Journal of Micromechanics and Microengineering*, 20(7), pp 075016.

[25] Oldham K., Pulskamp J., Polcawich R., and Dubey M., 2008. "Thin-Film PZT Lateral Actuators with Extended Stroke". *Journal of Microelectromechanical Systems*, 17(4), pp 890-899.

[26] Maia N. M. M., and Silva J. M. M., 2001. "Modal Analysis Identification Techniques". *Phil. Trans. R. Soc. Lond. A*, 359, pp 29-40.

[27] Bhushan B., Liu H., and Hsu S. M., 2004. "Adhesion and Friction Studies of Silicon

and Hydrophobic and Low Friction Films and Investigation of Scale Effects". *Journal of Tribology*, 126, pp 583-590.

[28] Chilamakuri S. K., and Bhushan B., 1999. "A Comprehensive Kinetic Meniscus Model for Prediction of Long-Term Static Friction". *J. Appl. Phys.*, 86, pp 4649.

[29] Luengo G., Pan J., Heuberger M., and Israelachvili J. N., 1998. "Temperature and Time Effect on The Adhesion Dynamics of Poly(Butyl Methacrylate) (PBMA) Surfaces". *Langmuir*, 14(14), pp 3873-3881.

[30] Persson B., Albohr O., Tartaglino U., Volokitin A. I., and Tosatti E., 2005. "On The Nature of Surface Roughness with Application to Contact Mechanics, Sealing, Rubber Friction and Adhesion". *Journal of Physics: Condensed Matter*, 17, pp R1-R62.

[31] Taya M., Almajid A. A., Dunn M., and Takahashi H., 2003. "Design of Bimorph Piezo-Composite Actuators with Functionally Graded Microstructure". *Sensors and Actuators A*, 107, pp 248-260.

[32] Wagg D. J., 2006. "A Note on Coefficient of Restitution Models Including The Effects of Impact Induced Vibration". *Journal of Sound and Vibration*, 300, pp 1071-1078.

[33] Odegard G. M., Gates T. S., and Herring H. M., 2005. "Characterization of Viscoelastic Properties of Plymeric Materials Through Nanoindentation". *Experimental Mechanics*, 45, pp 130-136.

[34] Krylov S., and Barnea D. I., 2005. "Bouncing Mode Electrostatically Actuated Scanning Micromirror for Video Applications". *Smart Mater. Struct.*, 14, pp 1281-1296.

[35] Salapaka M. V., Chen D. J., and Cleveland J. P., 2000. "Linearity of Amplitude and Phase in Tapping-Mode Atomic Force Microscopy". *Phys. Rev.* B, 61, pp 1106-1115.

[36] Tornambè A., 1999. "Modeling and Control of Impact in Mechanical Systems:

Theory and Experimental Results". *IEEE transactions on automatic control*, 44, pp 294-309.

[37] Silva M. F., Tenreiro Machado J. A., and Lopes A. M., 2005. "Modelling and Simulation of Artificial Locomotion Systems". *Robotica*, 23, pp 595-606.

[38] Hurmuzlu Y., and Marghitu D. B., 1999. "Rigid Body Collisions of Planar Kinematic Chain with Multiple Contact Points". *The International Journal of Robotics Research*, 13, pp 82-92.

[39] Guo A., and Batzer S., 2004. "Substructure Analysis of a Flexible System Contact-Impact Event". *Journal of Vibration and Acoustics*, 126, pp 126-131.

[40] Greenwood J. A., and Williamson J. B. P., 1966. "Contact of Nominally Flat Surfaces". *Proceedings of the Royal Society of London, Series A, Mathematical and Physical Sciences*, 95, pp 300-319.

[41] Bruneau O., and Ouezdou F. B., 1997. "Compliant Contact of Walking Robot Feet". *Proceeding of the third ECPD international conference on advanced robotics, intelligent automation and active systems, Bremen, Germany, September 26 28, 1997.*

[42] Ryou J. H., and Oldham K. R., 2012. "Model Identification for Impact Dynamics of a Piezoelectric Microactuator". *J. Micromech. Microeng.*, 22, pp 115002.

[43] Dick A. J., Balachandran B., DeVoe D. L., and Mote Jr C. D., 2006. "Parametric Identification of Piezoelectric Microscale Resonator". *J. Micromech. Microeng.*, 16, pp 1593-1601.

[44] Hahn B., and Oldham K. R., 2012. "A Model-Free ON-OFF Iterative Adaptive Controller Based on Stochastic Approximation". *IEEE Transactions on Conrol Systems Technology*, 20(1), pp 196-204.

[45] Sreenath K., Park H.-W., Poulakakis I., and Grizzle J. W., 2011. "A Compliant Hybrid Zero Dynamics Controller for Stable, Efficient and Fast Bipedal Walking on MABEL". *The International Journal of Robotics Research*, 30(9), pp 1170-1193.

[46] Silva M. F., Machado J.A. T., and Barbosa R. S., 2006. “Complex-order Dynamics in Hexapod Locomotion”. *Signal Processing*, 86, pp 2785-2793.

[47] Mistry M., Buchli J., and Schaal S., 2010. “Inverse Dynamics Control of Floating Base Systems Using Orthogonal Decomposition”. *2010 IEEE International Conference on Robotics and Automation, Anchorage Convention District*, *May 3-8, 2010, Anchorage, Alaska, USA.*

[48] Potkonjak V., Svetozarevic B., Jovanovic K., and Holland O., 2011. “Anthropomimetic Robot with Passive Compliance – Contact Dynamics and Control”. *19th Mediterranean Conference on Control and Automation, Aqula Corfu Holiday Palace, Corfu, Greece, June 20-23, 2011.*

[49] Saha S. K., Fiorini P., and Shah S. V., 2006. “Landing Mechanisms for Hopping Robots: Considerations and Prospects”. *In Proceedings of the 9th ESA Workshop on Advanced Space Technologies for Robotics and Automation ‘ASTRA 2006’ ESTEC, Noordwijk, The Netherlands, November 28-30, 2006.*

[50] Kim S., Spenko M., Trujillo S., Heyneman B., Mattoli V., and Cutkosky M. R., 2007. “Whole Body Adhesion: Hierarchical, Directional and Distributed Control of Adhesive Forces for a Climbing Robot”. *2007 IEEE International Conference on Robotics and Automation, Roma, Italy, 10-14 April 2007.*

[51] Park H. S., and Sitti M., 2009. “Complian Footpad Design Analysis for a Bio-inspired Quadruped Amphibious Robot”. *The 2009 IEEE/R&J International Conference on Intelligent Robots and Systems, October 11-15, 2009, St. Louis, USA.*

[52] Scarfogliero U., Stefanini C., and Dario P., 2009. “The Use of Compliant Joints and Elastic Energy Storage in Bio-inspired Legged Robots”. *Mechanism and Machine Theory*, 44, pp 580-590.

[53] Seipel J. E., Holmes P. J., and Full R. J., 2004. “Dynamics and Stability of Insect Locomotion: a Hexapedal Model for Horizontal Plane Motions”. *Biological Cybernetics*, 91, pp 76-90.

[54] Federle W., Riehle M., Curtis A. S.G., and Full R. J., 2002. “An Integrative Study of Insect Adhesion: Mechanics and Wet Adhesion of Pretarsal Pads in Ants”. *Integrative & Comparative Biology*, 42, pp 1100-1106.

[55] Claudio Quaglia, Elisa Buselli, Robert J Webser III, Pietro Valdastri, Arianna Menciassi, and Paolo Dario, 2009. “An Endoscopic Capsule Robot: A Meso-scale Engineering Case Study”. *Journal of Micromechanics and Microengineering*, 19, September, pp. 1-11.

[56] Zhenlong Wang, Guanrong Hang, Jian Li, and Yangwei Wang, 2008. “A Micro-robot Fish with Embedded SMA Wire Actuated Flexible Biomimetic Fin”. *Sensors and Actuators A: Physical*, 144, February, pp. 354-360.

[57] Jonathan E. Clark, and Mark R. Cutkosky, 2006. “The Effect of Leg Specialization in a Biomimetic Hexapedal Running Robot”. *Journal of Dynamic Systems, Measurement, and Control*, 128, March, pp. 26-35.

[58] Me+ARL, *Journal of Integrated Ferroelectrics*

[59] M.J. Sinclair, 2002. "A high force low area MEMS thermal actuator," *Thermal and Thermomechanical Phenomena in Electronic Systems*, *Las Vegas, NV*, August

[60] C.H. Ko, J.J. Yang, and J.C. Chiou, 2002. "Efficient magnetic microactuator with an enclosed magnetic core,” *Journal of Microlithography, Microfabrication, and Microsystems*, Vol. 1, pp. 144-150

[61] E. Sarajlic, E. Berenschot, N. Tas, H. Fujita, G. Krijnen, and M. Elwenspoek, 2006. “Fabrication and characterization of an electrostatic contraction beams micromotor,” *19th IEEE International Conference on Micro Electro Mechanical Systems (MEMS), Istanbul, Turkey*, pp. 814-817, January

[62] S. K. Dey, K. D. Budd, and D. A. Payne, 1988, “Thin-Film Ferroelectrics of PZT by Sol-Gel Processing”. *IEEE Transactions on Ultrasonics, Ferroelectrics, and Frequency Control*, Vol. 35, No. 1, January, pp. 80-81

[63] Bharat Bhushan, Huiwen Liu, and Stephen M. Hsu, 2004. “Adhesion and Friction Studies of Silicon and Hydrophobic and Low Friction Films and Investigation of Scale Effects”. *Journal of Tribology,* 126, July, pp. 583-590

[64] Nikhil S Tambe, and Bharat Bhushan, 2004. “Scale Dependence of Micro/Nano-friction and Adhesion of MEMS/NEMS Materials, Coatings and Lubricants”. *Nanotechnology*, 15, October, pp. 1561-1570.

[65] Minoru Taya, Abdulhakim A. Almajid, Martin Dunn, and Hirofumi Takahashi, 2003, “Design of Bimorph Piezo-composite Actuators with Functionally Graded Microstructure*”. Sensors and Actuators A*, 107, June, pp. 248-260.

[66] Zheng Chen, Yantao Shen, Ning Xi, and Xiaobo Tan, 2006. “Integrated Sensing for Ionic Polymer-metal Composite Actuators Using PVDF Thin Films*”. Smart Materials and Structures*, 16, March, pp. S262-S271

[67] K. Yamanaka, A. Noguchi, T. Tsuji, T. Koike, and T. Goto, 1998. “Quantitative Material Characterization by Ultrasonic AFM”. *Surface and Interface Analysis*, 27, December, pp. 600-606

[68] Ricardo Garcı´a, and Alvaro San Paulo, 1999. “Attractive and Repulsive Tip-sample Interaction Regimes in Tapping-mode Atomic Force Microscopy”. *Physical Review B,* 7, August, pp. 4961-4967

[69] Jeong H. Ryou, and Kenn R. Oldham, 2010. “Simulation Study and Experimental Testing of Foot-Terrain Dynamics in Piezoeectric Micro-Robots”. *Dynamic Systems and Control Conference*, *Boston, MA*

[70] In book, D. J. Inman, 2001. Engineering Vibration, 2nd ed., Prentice Hall, USR, NJ 07458, Chap. 7, pp. 495–532.

[71] L. Sirghi, O. Kylia´n, D. Gilliland, G. Ceccone, and F. Rossi, 2006. “Cleaning and Hydrophilization of Atomic Force Microscopy Silicon Probes”. *Journal of Physical Chemistry. B,* 110, October, pp. 25975-25981

[72] E. Buks, and M. L. Roukes, 2001. “Stiction, Adhesion Energy, and The Casimir Effect in Micromechanical Systems”. *Physical Review B*, 63, January, pp. 033402-1-033402-4

[73] Mark Raibert, Kevin Blankespoor, Gabriel Nelson, and Rob Playter, 2008. “BigDog, the Rough-Terrain Quadruped Robot”. *The International Federation of Automatic Control,* 6-11, July, pp. 10822-10825

[74] Amir Shapiro, Elon Rimon, and Shraga Shoval, 2005. “A foothold Selection Algorithm for Spider Robot Locomotion in Planar Tunnel Environments”. *The international Journal of Robotics Research*, Vol.24, No. 10, October, pp. 823-844

[75] Ill-Woo Park, Jung-Yup Kim, Jungho Lee, and Jun-Ho Oh, 2005. “Mechanical Design of Humanoid Robot Platform KHR-3”. *International Conference on Humanoid Robots,* pp 321-326

[76] Fred Delcomyn, and Mark E. Nelson, 2000, “Architectures for a biomimetic hexapod robot”. *Robotics and Autonomous Systems*, 30, pp. 5-15

[77] S. Laksanacharoen, A. J. Pollack, G. M. Nelson, R. D. Quinn, and R. E. Ritzmann, 2000, “Biomechanics and Simulation of Cricket for Micro-robot Design”, *IEEE International Conference on Robotics & Automation, San Francisco, CA*, April, pp. 1088-1094